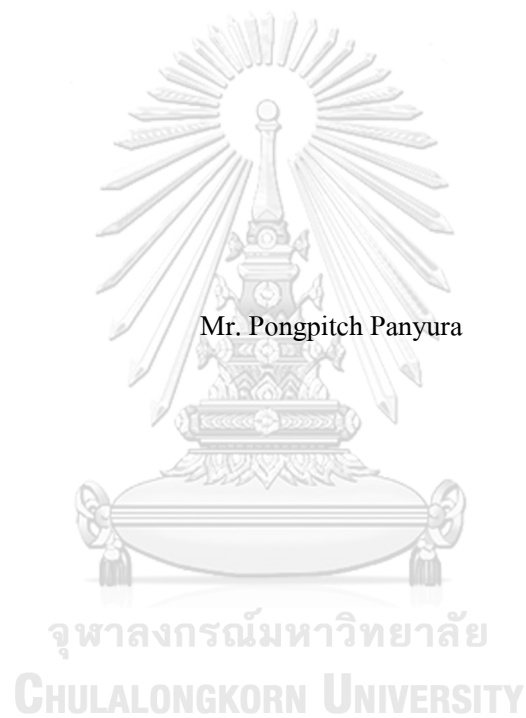


Effect of Inter-observer Delineation Variability on Radiomics Features in Nasopharyngeal Cancer



A Thesis Submitted in Partial Fulfillment of the Requirements  
for the Degree of Master of Science in Medical Physics

Department of Radiology

FACULTY OF MEDICINE

Chulalongkorn University

Academic Year 2022

Copyright of Chulalongkorn University

การศึกษาผลของความแปรปรวนในการวัดขอบเขตรอยโรคระหว่างผู้สังเกตที่ต่างกันต่อค่าพีเจอร์  
ของเรดิโอมิกส์ในโรคมะเร็งหลังโพรงจมูก



วิทยานิพนธ์นี้เป็นส่วนหนึ่งของการศึกษาตามหลักสูตรปริญญาวิทยาศาสตรมหาบัณฑิต  
สาขาวิชาฟิสิกส์การแพทย์ ภาควิชารังสีวิทยา  
คณะแพทยศาสตร์ จุฬาลงกรณ์มหาวิทยาลัย  
ปีการศึกษา 2565  
ลิขสิทธิ์ของจุฬาลงกรณ์มหาวิทยาลัย



พงษ์พิชญ์ พันธุ์ธูรา : การศึกษาผลของความแปรปรวนในการวาดขอบเขตรอยโรคระหว่างผู้สังเกต  
ที่ต่างกันต่อค่าพีเจอร์ของเรดิโอมิกส์ในโรคมะเร็งหลังโพรงจมูก. ( Effect of Inter-observer  
Delineation Variability on Radiomics Features in Nasopharyngeal Cancer) อ.ที่ปรึกษาหลัก : ผศ.  
ดร. โยธิน รักรวงษ์ไทย

โรคมะเร็งหลังโพรงจมูกเป็นหนึ่งในโรคมะเร็งศีรษะและลำคอที่พบได้บ่อยในประเทศไทยและเอเชียตะวันออกเฉียงใต้ โดยมีการรักษามาตรฐานคือการฉายรังสี (Radiation Therapy หรือ RT) ซึ่งต้องอาศัยการกำหนดขอบเขตรอยโรค (Target Volume Delineation หรือ TVD) ที่แม่นยำเพื่อการฉายรังสีอย่างมีประสิทธิภาพ ในขณะที่เนื้อเยื่อโดยรอบได้รับความเสียหายน้อยที่สุด อย่างไรก็ตาม การกำหนดขอบเขตรอยโรคอยู่ภายใต้ผลของความแปรปรวนทั้งภายในผู้สังเกตคนเดียว (intra-observer variability) และระหว่างผู้สังเกตหลายคน (inter-observer variability) ซึ่งส่งผลกระทบต่อความแม่นยำของการฉายรังสีและนำไปสู่ความไม่เสถียรของผลลัพธ์ของการวิเคราะห์ด้วยเรดิโอมิกส์ (Radiomics) โดยเรดิโอมิกส์คือวิธีการนำข้อมูลภาพมาวิเคราะห์เชิงปริมาณจากภาพทางการแพทย์ ซึ่งในขณะนี้ยังจำกัดด้วยการวาดขอบเขตรอยโรคโดยการใช้คนวาด ในงานวิจัยนี้มีวัตถุประสงค์เพื่อศึกษาผลของความแปรปรวนระหว่างผู้สังเกตในการวาดขอบเขตรอยโรคในเนื้องอกโดยการใช้คนวาดต่อความเสถียรของคุณลักษณะเรดิโอมิกส์ หรือเรดิโอมิกส์พีเจอร์ (Radiomic features) ในโรคมะเร็งหลังโพรงจมูก ในงานวิจัยนี้ใช้ภาพซีทีที่ได้จากผู้ป่วยที่ได้รับการวินิจฉัยว่าเป็นโรคมะเร็งหลังโพรงจมูก โดยรังสีแพทย์จะเป็นผู้วาดกำหนดขอบเขตของบริเวณรอยโรค (GTV) ของก้อนมะเร็งปฐมภูมิในภาพซีที เพื่อนำมาคำนวณเรดิโอมิกส์พีเจอร์โดยใช้โปรแกรมไพเรดิโอมิกส์ (Pyradiomics) ซึ่งพีเจอร์เหล่านี้จะถูกแบ่งแยกออกเป็น 4 กลุ่มและใช้ความกว้างของบิน (binwidth) จำนวน 3 ค่าในการคำนวณพีเจอร์ ในการวัดค่าความแปรปรวนระหว่างผู้สังเกตจะวัดโดยใช้ค่าสัมประสิทธิ์ความคล้ายของไดซ์ (Dice similarity coefficient), สัมประสิทธิ์สหสัมพันธ์ภายในชั้น (Intraclass Correlation Coefficient หรือ ICC) และค่าสัมประสิทธิ์ของความแปรปรวน (Coefficient of Variation หรือ CV) โดยเกณฑ์ในการเลือกพีเจอร์ที่เสถียรจะกำหนดที่ค่า ICC มากกว่า 0.8 และค่า CV น้อยกว่า 10 เปอร์เซ็นต์ ซึ่งเป็นค่าที่สามารถตัดสินได้ว่ามีความสามารถในการวัดซ้ำได้อย่างดีเยี่ยม ผลการศึกษาพบว่าพีเจอร์ในกลุ่มของ Shape และ First-order มีความเสถียรในทุกค่าความกว้างของบินที่ค่า ICC มากกว่า 0.8 แสดงถึงการวาดของแพทย์มีความใกล้เคียงกันเป็นอย่างดี ในขณะที่พีเจอร์ในกลุ่มของ Wavelet มีความเสถียรมากที่สุดซึ่งสามารถนำไปใช้ในการสร้างแบบจำลองเพื่อใช้ในการทำนายในอนาคต

สาขาวิชา      ฟิสิกส์การแพทย์  
ปีการศึกษา      2565

ลายมือชื่อนิติ .....  
ลายมือชื่อ อ.ที่ปรึกษาหลัก .....

## 6370029630 : MAJOR MEDICAL PHYSICS

KEYWORD: Nasopharyngeal cancer, Radiomics, Inter-observer variability, Dice coefficient

Pongpitch Panyura : Effect of Inter-observer Delineation Variability on Radiomics Features in Nasopharyngeal Cancer. Advisor: Asst. Prof. YOTHIN RAKVONGTHAI, Ph.D.

Nasopharyngeal cancer (NPC) is a type of head and neck cancer that is prevalent in China and Southeast Asia. The standard treatment for NPC is radiation therapy (RT), which requires accurate target volume delineation (TVD) to ensure an effective radiation dose while minimizing damage to surrounding healthy tissues. However, TVD is subject to intra- and inter-observer variability, which can affect the accuracy of RT and lead to unstable results in radiomics analysis. Radiomics is a technique that extracts quantitative data from medical images, but it is currently limited by the manual process of tumor delineation. This study aims to investigate the impact of inter-observer variability in manual tumor delineation on the stability of radiomic features in NPC. CT images were collected from patients who were diagnosed with Nasopharyngeal carcinoma (NPC) and were manually contoured by radiation oncologists to determine gross tumor volume (GTV) of the primary tumor. CT images were then analyzed to extract radiomic features using Pyradiomics. The extracted features were classified into four feature classes, and the binwidth parameter was varied into three values. To measure inter-observer variability, Dice similarity coefficient, intraclass correlation coefficient (ICC), and coefficient of variation (CV) were used. The ICC threshold of 0.8 was selected to determine stable features, and the CV threshold of 10% was selected for excellent reproducibility. The results showed that the shape and first-order classes were stable in all binwidths with an ICC value greater than 0.8, indicating good performance in tumor delineation. Additionally, the wavelet class had the most robust feature with respect to ICC and %CV, which can be used for prediction models in the future.

CHULALONGKORN UNIVERSITY

Field of Study: Medical Physics

Student's Signature .....

Academic Year: 2022

Advisor's Signature .....

## ACKNOWLEDGEMENTS

I would like to acknowledge the contributions and support of numerous individuals and institutions throughout this study. Firstly, we express our heartfelt gratitude to Assistant Professor Yothin Rakvongthai, Ph.D., from the Division of Nuclear Medicine, Department of Radiology, Faculty of Medicine, Chulalongkorn University. His patient guidance, supervision, and motivation have been invaluable in the completion of this master's degree study and research.

Furthermore, I extend our deep appreciation to Sararas Khongwirotphan, Ph.D., and Napat Ritlumlert from Chulalongkorn University Biomedical Imaging Group (CUBIG), Department of Radiology, Faculty of Medicine, Chulalongkorn University, Bangkok. Their generous assistance in data analysis and valuable suggestions for the clinical research aspect are greatly appreciated.

My profound thanks go to our thesis committee members: Assistant Professor Taweap Sanghangthum, Ph.D., from the Division of Radiotherapy, Department of Radiology, Faculty of Medicine, Chulalongkorn university, who served as the Chairman of the thesis committee, and Professor Kosuke Matsubara, Ph.D., from Kanazawa University, Japan, who acted as the external examiner during the thesis defense. I appreciate their encouragement and insightful comments, which have broadened the perspectives of our research.

Additionally, I would like to express our gratitude to all the lecturers, staff, and fellow colleagues in the Master of Science program in Medical Physics, Department of Radiology, Faculty of Medicine, Chulalongkorn University. Their suggestions, kind support, and teaching have been instrumental throughout the entire study.

Finally, we would like to acknowledge and thank our family for their unwavering support and encouragement during the compilation of this dissertation. Their contributions have kept us motivated, and this work would not have been possible without their involvement.

Pongpitch Panyura

## TABLE OF CONTENTS

|  | <b>Page</b> |
|--|-------------|
| .....  | iii         |
| ABSTRACT (THAI) .....                            | iii         |
| .....  | iv          |
| ABSTRACT (ENGLISH).....                          | iv          |
| ACKNOWLEDGEMENTS.....                            | v           |
| TABLE OF CONTENTS.....                           | vi          |
| LIST OF TABLES.....                              | x           |
| LIST OF FIGURES .....                            | xi          |
| CHAPTER I INTRODUCTION.....                      | 1           |
| 1.1 Background and rationale.....                | 1           |
| 1.2 Research question.....                       | 2           |
| 1.3 Research objectives .....                    | 2           |
| 1.3.1 Primary objective .....                    | 2           |
| 1.3.2 Secondary objective .....                  | 2           |
| 1.4 Significant and impact of the work .....     | 3           |
| 1.5 Definition .....                             | 3           |
| CHAPTER II THEORY AND RELATED LITERATURE .....   | 4           |
| 2.1 Theory .....                                 | 4           |
| 2.1.1 Nasopharyngeal carcinoma.....              | 4           |
| 2.1.1.1 Causes of nasopharyngeal carcinoma ..... | 4           |
| 2.1.1.2 Sign and symptoms.....                   | 4           |

|   |    |
|---|----|
| 2.1.1.3 Staging .....   | 5  |
| 2.1.1.4 Radiographic features .....                               | 5  |
| 2.1.1.5 Treatment .....   | 6  |
| 2.1.2 Radiomics.....  | 7  |
| 2.1.2.1 Fundamental of Radiomics .....                            | 7  |
| 2.1.2.2 Types of Radiomics Features.....                          | 8  |
| 2.1.2.2.1 Shape features.....                                     | 8  |
| 2.1.2.2.2 First-order features .....                              | 14 |
| 2.1.2.2.3 Texture features.....                                   | 19 |
| 2.1.2.2.4 Wavelet features .....                                  | 26 |
| 2.1.3 Inter-observer variability.....                             | 26 |
| 2.1.3.1 Dice coefficient.....                                     | 26 |
| 2.1.3.2 Intraclass correlation coefficient (ICC) .....            | 26 |
| 2.1.3.3 Coefficient of variation (CV).....                        | 27 |
| 2.2 Review of related literatures .....                           | 27 |
| Chang ATY, Tan LT, Duke S, Ng WT. (2017) <sup>(15)</sup> .....    | 27 |
| Pavic M, Bogowicz M, Würms X, et al. (2018) <sup>(18)</sup> ..... | 28 |
| CHAPTER III RESEARCH METHODOLOGY .....                            | 29 |
| 3.1 Research designs .....  | 29 |
| 3.2 Research design model.....                                    | 29 |
| 3.3 Conceptual framework .....                                    | 29 |
| 3.4 Key Word .....  | 30 |
| 3.5 The sample .....  | 30 |
| 3.5.1 Target population .....                                     | 30 |



|   |    |
|---|----|
| 3.5.2 Sample population.....                          | 30 |
| 3.5.3 Eligible criteria.....                          | 30 |
| 3.5.3.1 The inclusion criteria .....                  | 30 |
| 3.5.3.2 The exclusion criteria.....                   | 30 |
| 3.5.4 Sample size determination .....                 | 31 |
| 3.6 Materials.....                                    | 31 |
| 3.6.1 Computed tomography simulator.....              | 31 |
| 3.6.2 Pyradiomics software 3.0.1.....                 | 32 |
| 3.6.3 3D Slicer software.....                         | 32 |
| 3.6.4 MATLAB software.....                            | 33 |
| 3.6.5 Python .....                                    | 33 |
| 3.7 Methods.....                                      | 33 |
| 3.7.1 Patient data collection .....                   | 33 |
| 3.7.2 Tumor delineation.....                          | 34 |
| 3.7.3 Radiomics features extraction.....              | 34 |
| 3.7.4 Inter-observer variability analysis.....        | 34 |
| 3.7.4.1 Dice coefficient .....                        | 34 |
| 3.7.4.2 Intraclass correlation coefficient (ICC)..... | 34 |
| 3.7.4.3 Coefficient of variation (CV).....            | 35 |
| 3.8 Statistical analysis .....                        | 35 |
| 3.9 Ethical consideration.....                        | 35 |
| CHAPTER IV RESULTS.....                               | 36 |
| 4.1 The variation of tumor delineation.....           | 36 |
| 4.1.1 Dice coefficient.....                           | 36 |

|  |    |
|--|----|
| 4.1.2 Determination of stable radiomics features .....     | 36 |
| CHAPTER V DISCUSSION AND CONCLUSIONS .....                 | 42 |
| 5.1 Discussion .....                                       | 42 |
| 5.2 Conclusions .....                                      | 44 |
| APPENDIX A THE APPROVAL OF INSTITUTIONAL REVIEW BOARD..... | 45 |
| APPENDIX B RESULTS OF STABLE RADIOMICS FEATURES.....       | 47 |
| REFERENCES .....   | 95 |
| VITA .....   | 98 |



## LIST OF TABLES

|  | <b>Page</b> |
|--|-------------|
| Table 1 TNM staging of NPC according to AJCC 8 <sup>th</sup> edition <sup>(10, 11)</sup> ..... | 6           |
| Table 2 Dice coefficient of five radiation oncologists from the data sets of 30 patients.....  | 37          |
| Table 3 The most stable features with the highest ICC and lowest %CV in each class .....       | 41          |
| Table 4 The stable features in shape class in terms of ICC .....                               | 47          |
| Table 5 The stable features in first-order class in terms of ICC .....                         | 48          |
| Table 6 The stable features in texture class in terms of ICC .....                             | 49          |
| Table 7 The stable features in wavelet class in terms of ICC .....                             | 51          |
| Table 8 The stable features in shape class in terms of %CV .....                               | 80          |
| Table 9 The stable features in first-order class in terms of %CV .....                         | 81          |
| Table 10 The stable features in texture class in terms of %CV .....                            | 81          |
| Table 11 The stable features in wavelet class in terms of %CV.....                             | 82          |

## LIST OF FIGURES

|   | <b>Page</b> |
|---|-------------|
| Figure 1 Age-standardized (World) incidence rates of nasopharyngeal carcinoma in 2020.....                    | 5           |
| Figure 2 The process of radiomics <sup>(8)</sup> .....  | 8           |
| Figure 3 Research design.....   | 29          |
| Figure 4 Conceptual framework .....   | 29          |
| Figure 5 CT simulator, Somatom Definition AS, Siemens Medical Solutions, Erlangen, Germany.....               | 31          |
| Figure 6 Pyradiomics software .....   | 32          |
| Figure 7 3D Slicer software version 5.0.3 .....   | 32          |
| Figure 8 MATLAB software version R2022b.....  | 33          |
| Figure 9 The percentage of stable features in each class varying three binwidths. ....                        | 38          |
| Figure 10 The percentage of stable features compared to the results of Pavic M, et al. in HNSCC. ....         | 39          |
| Figure 11 The percentage of stable features in each class at %CV < 10,20,30 .....                             | 39          |
| Figure 12 The histogram of stable features in the shape class in range of %CV between 0 and 30 .....          | 40          |
| Figure 13 The percentage of stable radiomics features among three binwidth compared between ICC and %CV ..... | 40          |

# CHAPTER I

## INTRODUCTION

### 1.1 Background and rationale

Nasopharyngeal cancer (NPC) is a type of head and neck cancer that occurs in the nasopharynx, the upper part of the throat behind the nose and near the base of the skull, and is endemic in China and Southeast Asia where the prevalence rate is 15-50 cases per 100,000 people<sup>(1,2)</sup>. According to the International Agency for Research on Cancer, there have been approximately 130,000 new cases of NPC in 2020<sup>(3)</sup>.

The standard treatment for NPC is radiation therapy (RT) that delivers a lethal dose of radiation to cancer cells, while minimizing dose to surrounding healthy structures. The mainstay RT is photon-based radiotherapy that has evolved gradually over the past few decades, first from 2D to 3D conformal radiotherapy, and then to advanced radiotherapy techniques such as intensity-modulated radiation therapy (IMRT) that enables better target coverage with conformity of dose distribution achieved by sculpting the high-dose zone for complete coverage of tumor targets while sparing the critical normal structures<sup>(4,5)</sup>. Due to the high-dose zone of IMRT, we need to improve the precision of every step of treatment planning and delivery. The most crucial step is the accurate localization and delineation of the target volume. Target volume delineation (TVD) is the process of distinguishing tumor boundaries from surrounding structures<sup>(6)</sup>. TVD remains constant during the course of radiation therapy and therefore, has a large impact on the dose to the tumor. Major sources of TVD variation are visibility of the target, including its extensions (impact of imaging protocol), disagreement on the target extension, and interpretation or lack of delineation protocols. The magnitude of the contouring problem is usually seen in the studies of intra- and inter-observer variability. The variation had the potential to affect the dose-volume histograms of critical structures and the probabilities of normal tissue complication. The apparent causes of intra- and inter-observer variability can be attributed to many factors, including the impact of imaging (imaging modality and technique) and influence of the observer (speciality, training, and personal bias)<sup>(7)</sup>.

In NPC imaging such as computed tomography (CT) and magnetic resonance imaging (MRI), there are many ways to analyze the tumor appearance in radiographic images. However, these images contain information about disease-specific processes that are imperceptible to the human eye and therefore are not accessible by traditional visual inspection of the generated images. Recently, there is an appropriate technique for tumor characterization in terms of quantitative value which is called radiomics. Radiomics extracts quantitative data of medical image, so-called radiomic features, to mathematical data that reduce intra- and inter-observer variability<sup>(8, 9)</sup>. Moreover, the variation of medical images can be in terms of Dice coefficient, which is a statistical tool that measures the similarity between two images.

In conclusion, tumor delineation is an important step in radiomics and is currently still a manual process. Due to inter-observer variability in the delineation process being a well-known uncertainty in radiation oncology, differences of tumor delineation could potentially lead to unstable results in the radiomics analysis. Consequently, this study aimed to determine the impact of inter-observer variability in manual tumor delineation on the stability of radiomic features in nasopharyngeal cancer.

## **1.2 Research question**

What is the impact of tumor delineation variability due to different radiation oncologists on extracted radiomic features in CT images of nasopharyngeal cancer patients?

## **1.3 Research objectives**

### **1.3.1 Primary objective**

To determine the variation of radiomic features due to multiple tumor delineation and determine stable radiomic features.

### **1.3.2 Secondary objective**

To determine the variation in tumor delineation by radiation oncologists in nasopharyngeal cancer using the Dice coefficient.

#### 1.4 Significant and impact of the work

Tumor delineation is an important process in radiation treatment planning. However, there are many factors affecting the quality of the contouring, such as intra- and inter-observer variability. One of the appropriate methods to determine the quantity of variability is radiomics that extract information from medical images in terms of radiomic features for tumor prognosis and prediction of treatment response.

The objective of this study is to determine the impact of inter-observer variability in manual tumor delineation on radiomic feature extraction in nasopharyngeal cancer.

#### 1.5 Definition

|                   |  |
|-------------------|--|
| Tumor delineation | The process of separating tumor boundaries from surrounding normal tissues.            |
| Radiomics         | A quantitative approach of mathematical algorithms that extracted from medical images. |
| Dice coefficient  | A spatial overlap index that is used to gauge the similarity of two regions.           |

## CHAPTER II

### THEORY AND RELATED LITERATURE

#### 2.1 Theory

##### 2.1.1 Nasopharyngeal carcinoma

Nasopharyngeal carcinoma (NPC) is one of the most common head and neck cancers worldwide, about 86,500 cases of nasopharynx cancer and 50,000 deaths are reported annually, especially in China and Southeast Asia, where the prevalence rate is 15-50 cases per 100,000 people <sup>(2)</sup>.

##### 2.1.1.1 Causes of nasopharyngeal carcinoma

The exact causes of NPC are not fully understood, there are multiple risk factors that have been suggested as potentially contributing to its development. These potential risk factors are Epstein-Barr virus (EBV) infection, genetic predisposition, environmental exposure, ethnicity, dietary factors, smoking, and alcohol consumption.

##### 2.1.1.2 Sign and symptoms

Diagnosis of nasopharyngeal carcinoma (NPC) in its early stages can be challenging due to the location of the tumor. In many cases, NPC may grow significantly before patients become aware of it and spread to other organ structures. Common signs and symptoms of NPC patients include swollen lymph nodes in the neck, nasal blockage, hearing loss, bleeding, blurred vision, headaches, difficulty speaking or swallowing, and facial pain.



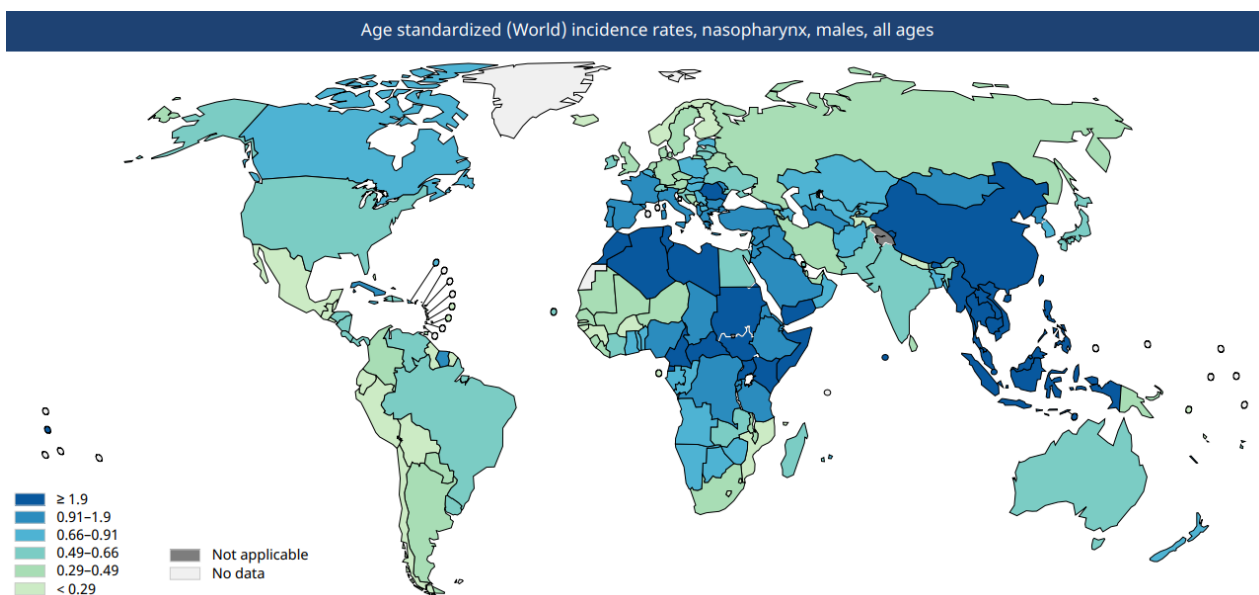


**Figure 1** Age-standardized (World) incidence rates of nasopharyngeal carcinoma in 2020

#### 2.1.1.3 Staging

The TNM staging system for malignant tumors of the nasopharynx is used to determine the stage of NPC according to the 8th edition of the America Joint Committee on Cancer (AJCC) which is shown in Table 1. This system classifies into 3 parts including tumor (T) refers to tumor size and tumor extension, node (N) means involvement of nearby lymph nodes and metastasis (M) indicates the presence of distant metastasis. The cancer stage is the combination of T, N, and M.

#### 2.1.1.4 Radiographic features

Medical imaging is an important tool for tumor characterization. In NPC, magnetic resonance imaging (MRI) is generally considered the preferred imaging modality due to high soft tissue contrast. However, CT scans may also be used as an adjunct to MRI in the evaluation of NPC, especially to evaluate bone involvement and detect distant metastasis. Most NPC cases consist of bony structure, CT can provide detailed information for radiotherapeutic treatment planning that is greater than MRI.

**Table 1** TNM staging of NPC according to AJCC 8<sup>th</sup> edition<sup>(10, 11)</sup>

| AJCC stage | Stage grouping       | Stage description  |
|------------|----------------------|--|
| 0          | Tis*, N0, M0         | The tumor is only inside nasopharynx with no spread to lymph nodes and no distant metastasis   |
| I          | T1, N0, M0           | Tumor confined to the nasopharynx or oropharynx with no spread to lymph nodes and no distant metastasis  |
| II         | [T0, T1], N1, M0     | Tumor confined to the nasopharynx or oropharynx with involvement of unilateral or bilateral lymph nodes and no distant metastasis  |
|            | or                   |  |
|            | T2, [N0, N1], M0     | Tumor involving the nasopharynx or oropharynx with local invasion of adjacent structures with involvement of unilateral or bilateral lymph nodes and   |
| III        | [T0, T1, T2], N2, M0 | Tumor involving the nasopharynx or oropharynx with local invasion of adjacent structures with involvement of bilateral or contralateral lymph nodes  |
|            | or                   |  |
|            | T3, [N0, N1, N2], M0 | Tumor involving the bony structures of the skull base, paranasal sinuses, or infratemporal fossa with involvement of bilateral or contralateral lymph nodes  |
| IVA        | T4, [N0, N1, N2], M0 | Tumor with intracranial extension or involvement of cranial nerves, or with extensive invasion of adjacent structures with involvement of bilateral or contralateral lymph nodes and no distant metastasis |
|            | or                   |  |
|            | [Any T], N3, M0      | The tumor might or might not have grown into structures outside the nasopharynx with involvement of lymph nodes or extension to supraclavicular fossa no distant metastasis                                |
| IVB        | [Any T], [Any N], M1 | The tumor might or might not have grown into structures outside the nasopharynx with spread or no spread to nearby lymph nodes with Distant  |
|            | Recurrent            | The tumor appear again after treatment   |

### 2.1.1.5 Treatment

There are several types of treatment for NPC patients including radiation therapy, chemotherapy, surgery, and immunotherapy. However, radiation therapy has the most important role in treatment due to the high dose to tumor and precise target localization. But the uncertainty in segmentation causes inconsistency in treatment planning. Therefore, an accurate contouring process is required in treatment planning. With a precise tool to improve the performance in segmentation, radiomics is one of the interesting approaches in this process.

## 2.1.2 Radiomics

### 2.1.2.1 Fundamental of Radiomics

Radiomics is a quantitative approach to medical imaging based on the assumption that medical images contain information related to disease-specific mechanisms that cannot be detected through the human eye. The approach of radiomics is an advanced image processing technique that extracts and analyzes quantitative features from medical images.

In the mathematical extraction of each image pixel, the image information transforms into numerical data, enabling an integrated cross-modality approach that takes advantage of the potential additional value of the extracted image information. These extracted features, the so-called radiomic features, describe the various characteristics of the images in each pixel and are used to derive meaningful information for clinical decision-making.

The main process of radiomics can be divided into four steps, including image acquisition followed by segmented of ROIs, such as tumor. After that, feature extraction was performed to extract the quantitative information of the images and used to analyze in the statistical analysis process to selected features to build a model for predicted outcome. All radiomic processes were illustrated in Figure 2<sup>(8)</sup>.

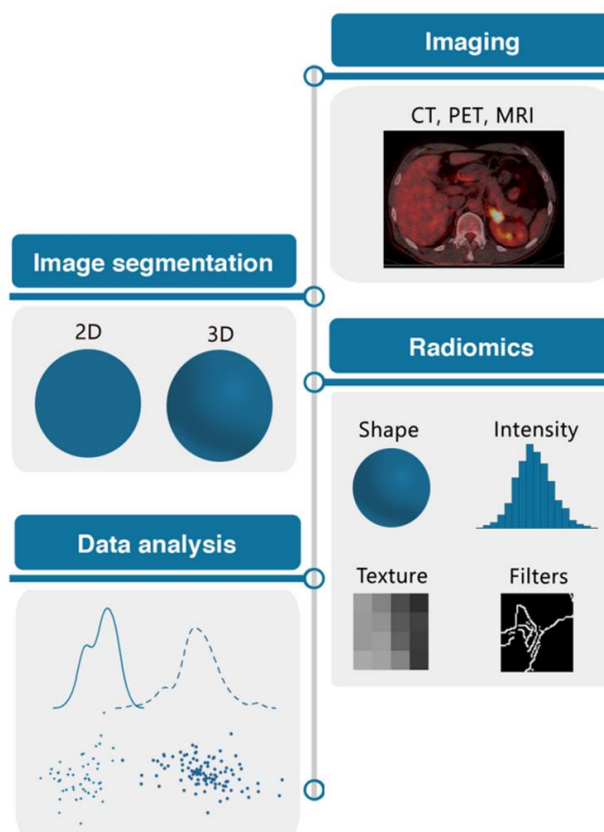


**Figure 2** The process of radiomics <sup>(8)</sup>

#### 2.1.2.2 Types of Radiomics Features

This study used a Python-based software tool called "PyRadiomics" to quantitatively analyze phenotypic characteristics in medical imaging. By applying this tool to tumor volumes, a total of 1288 features were extracted. These features can be classified into four classes, including shape, intensity, texture, and wavelet classes in medical imaging <sup>(12, 13)</sup>.

##### 2.1.2.2.1 Shape features

Shape features are a set of quantitative measurements that characterize the size, geometry, and spatial structure of regions of interest (ROI) within medical images. These features provide insight into the spatial arrangement, compactness, irregularity, and symmetry of the structures within the image. The radiomic features in this group are shown as follows.

- Mesh Surface

$$A_i = \frac{1}{2} Oa_i \times Ob_i \quad (1)$$

$$A = \sum_{i=1}^{N_f} A_i \quad (2)$$

Where  $O_i a_i$  and  $O_i b_i$  are edges of the  $i^{\text{th}}$  triangle in the mesh, formed by vertices  $a_i$ ,  $b_i$  of the perimeter and the origin  $O$ .

To determine the surface area, the initial step involves the calculation of the signed surface area  $A_i$  for each triangle present in the mesh (1). By summing up all the computed sub-areas, the total surface area can be obtained (2).

- Mesh Volume

$$V_i = \frac{Oa_i \cdot (Ob_i \times Oc_i)}{6} \quad (1)$$

$$V = \sum_{i=1}^{N_f} V_i \quad (2)$$

To calculate the volume of ROI, the triangle mesh of the ROI is utilized. For each face  $i$  in the mesh, defined by points  $a_i$ ,  $b_i$ , and  $c_i$ , contributes to the computation of the volume  $V_i$  of the tetrahedron formed by that face and the origin of the image  $O$  (1). The orientation of the normal vector determines the sign of the volume, and it should be consistently defined as either facing outward or inward of the ROI. By summing up all the individual volumes  $V_i$ , the total volume of the ROI can be determined (2).

- Pixel Surface

$$A_{\text{pixel}} = \sum_{k=1}^{N_v} A_k$$

The surface area of the ROI can be estimated by multiplying the pixel count within the ROI by the surface area of an individual pixel. However, this method provides a less accurate approximation

of the actual surface area. It does not rely on the mesh and is not utilized in calculating other 2D shape features.

- Voxel Volume

$$V_{\text{voxel}} = \sum_{k=1}^{N_v} V_k$$

The volume of the ROI can be estimated by multiplying the voxel count within the ROI by the volume of an individual voxel. However, this approximation provides a less accurate estimation of the actual volume and is not utilized in subsequent features. This method does not rely on the mesh and is not used in calculating other shape features.

- Perimeter

$$P_i = \sqrt{(a_i - b_i)^2} \quad (1)$$

$$P = \sum_{i=1}^{N_f} P_i \quad (2)$$

Where  $a_i$  and  $b_i$  are vertices of the  $i^{\text{th}}$  line in the perimeter mesh.

To determine the perimeter, the initial step involves calculating the perimeter  $P_i$  of each line in the circumference of the mesh (1). The total perimeter can then be obtained by adding up all the calculated sub-areas (2).

- Perimeter to Surface ratio

$$\text{perimeter to surface ratio} = \frac{P}{A}$$

Perimeter to Surface ratio is a metric that reflects the compactness of a shape, where a lower value indicates a more circular-like shape. This feature is partly influenced by the surface area of the ROI.

- Surface Area to Volume ratio

$$\text{surface to volume ratio} = \frac{A}{V}$$

Surface Area to Volume ratio is a metric that reflects the compactness of a shape, where a lower value indicates a more sphere-like shape. This feature is partly influenced by the volume of the ROI.

- Sphericity

$$\text{sphericity} = \frac{\sqrt[3]{36\pi V^2}}{A}$$

Sphericity is a quantitative measure that assesses the degree of roundness of the tumor region compared to a sphere. It is a dimensionless metric that remains unaffected by the scale and orientation of the shape. The range of possible values for sphericity is between 0 and 1, where a value of 1 indicates a perfect sphere (a perfect sphere possesses the smallest possible surface area for a given volume compared to other geometric solids).

- Spherical Disproportion

$$\text{spherical disproportion} = \frac{A}{4\pi R^2} = \frac{A}{\sqrt[3]{36\pi V^2}}$$

where R is the radius of a sphere with the same volume as the tumor, and equal to  $\sqrt[3]{\frac{3V}{4\pi}}$ .

Spherical disproportion is defined as the relationship between the surface area of the tumor region and the surface area of a sphere with the same volume as the tumor region. Since a perfect sphere has a value of 1, the value range is spherical disproportion  $\geq 1$ .

- Maximum 2D diameter (Slice)

Maximum 2D diameter (Slice) is the largest pairwise Euclidean distance between tumor surface mesh vertices in the row-column (the axial) plane.

- Maximum 2D diameter (Column)

Maximum 2D diameter (Column) is the largest pairwise Euclidean distance between tumor surface mesh vertices in the row-slice (the coronal) plane.

- Maximum 2D diameter (Row)

Maximum 2D diameter (Row) is the largest pairwise Euclidean distance between tumor surface mesh vertices in the column-slice (the sagittal) plane.

- Maximum 3D diameter

Maximum 3D diameter is the largest pairwise Euclidean distance between tumor surface mesh vertices.

- Major Axis Length

$$major\ axis = 4\sqrt{\lambda_{major}}$$

Major Axis Length is the largest axis length of the ROI-enclosing ellipsoid and can be calculated by using largest principal component  $\lambda_{major}$ .

- Minor Axis Length

$$minor\ axis = 4\sqrt{\lambda_{minor}}$$

Minor Axis Length is the second-largest axis length of the ROI-enclosing ellipsoid and can be calculated by using largest principal component  $\lambda_{minor}$ .



- Least Axis Length

$$\textit{least axis} = 4\sqrt{\lambda_{\textit{least}}}$$

Least Axis Length is the smallest axis length of the ROI-enclosing ellipsoid and can be calculated by using largest principal component  $\lambda_{\textit{least}}$ .

- Elongation

$$\textit{elongation} = \sqrt{\frac{\lambda_{\textit{minor}}}{\lambda_{\textit{major}}}}$$

where  $\lambda_{\textit{major}}$  and  $\lambda_{\textit{minor}}$  represent the lengths of the largest and second-largest principal component axes represent the basis for measuring elongation. The values of elongation range between 1, indicating a circular cross-section formed by the first and second largest principal moments (indicating a non-elongated shape), and 0, indicating maximum elongation where the object is reduced to a one-dimensional line.

Elongation characterizes the correlation between the two largest principal components within the shape of the ROI. Due to computational considerations, this feature is defined as the reciprocal of true elongation.

- Flatness

$$\textit{flatness} = \sqrt{\frac{\lambda_{\textit{least}}}{\lambda_{\textit{major}}}}$$

where  $\lambda_{\textit{major}}$  and  $\lambda_{\textit{least}}$  represent the lengths of the largest and smallest principal component axes, respectively. The values can vary between 1, indicating a non-flat, sphere-like shape, and 0, which represents a flat object or a single-slice segmentation.

The flatness of the ROI shape reveals the connection between the largest and smallest major components. This

characteristic is described as the inverse of the real flatness for computational purposes.

- Compactness 1

$$\text{compactness 1} = \frac{V}{\sqrt{\pi A^3}}$$

Compactness 1 measures how compact the tumor's form is in relation to a sphere (most compact), just like sphericity does. As a result, it is redundant and connected to sphericity. It is offered here to be comprehensive. The range of values is 0 to  $\frac{1}{6\pi}$  with a value of  $\frac{1}{6\pi}$  denoting a perfect sphere.

$$\text{Compactness 1} = \frac{1}{6\pi} \sqrt{\text{Compactness 2}} = \frac{1}{6\pi} \sqrt{\text{Sphericity}^3}$$

- Compactness 2

$$\text{compactness 2} = 36\pi \frac{V^2}{A^3}$$

Compactness 2 is a measurement of how compact the tumor's form is in relation to a sphere (most compact), much like Sphericity and Compactness 1. It is an arbitrary measurement that is not affected by scale or direction. The range of values is 0 to 1 with 1 denoting a perfect sphere.  $\text{Compactness 2} = (\text{Sphericity})^3$

#### 2.1.2.2.2 First-order features

First-order features described the statistical properties of voxel intensities within ROIs that capture information directly from the intensity histogram of the image without considering spatial relationships or texture patterns. The radiomic features in this group are shown as follows.

- Energy

$$energy = \sum_{i=1}^{N_p} (\mathbf{X}(i) + c)^2$$

where  $\mathbf{X}$  represents a set of  $N_p$  voxels contained within the ROI.  $\mathbf{P}(i)$  is the first-order histogram with  $N_g$  discrete intensity levels.  $N_g$  denotes the number of non-zero bins, which are evenly distributed from 0 with a specific width determined by the binWidth parameter. Furthermore,  $p(i)$  represents the normalized first-order histogram and is calculated as the ratio of  $\mathbf{P}(i)$  to  $N_p$ . The optional value  $c$  which is determined by the voxelArrayShift and is used to offset the intensities in  $\mathbf{X}$  to avoid negative values. This adjustment ensures that voxels with the lowest gray values have a minimal impact on the Energy calculation, rather than voxels with intensities closest to 0.

Energy represents a metric that quantifies the overall magnitude of the voxel values within an image. A higher Energy value indicates a larger sum of the squared voxel values.

- Total Energy

$$total\ energy = V_{voxel} \sum_{i=1}^{N_p} (\mathbf{X}(i) + c)^2$$

Total Energy is the value of the Energy feature multiplied by the cubic millimeters of the voxel's volume.

- Entropy

$$entropy = - \sum_{i=1}^{N_g} p(i) \log_2 (p(i) + \epsilon)$$

where  $\epsilon$  represents a very small positive number ( $2.2 \times 10^{-16}$ ).

- Minimum

$$\mathit{minimum} = \min(\mathbf{X})$$

Minimum is the minimum value of all gray level intensity within the ROI.

- 10th percentile

10th percentile is the 10th percentile of  $\mathbf{X}$ .

- 90th percentile

90th percentile is the 90th percentile of  $\mathbf{X}$ .

- Maximum

$$\mathit{maximum} = \max(\mathbf{X})$$

Maximum is the maximum value of all gray level intensity within the ROI.

- Mean

$$\mathit{mean} = \frac{1}{N_p} \sum_{i=1}^{N_p} \mathbf{X}(i)$$

Mean is the average gray level value within the ROI.

- Median

Median is the median gray level value within the ROI.

- Interquartile Range

$$\mathit{interquartile\ range} = P_{75} - P_{25}$$

where  $P_{25}$  and  $P_{75}$  are the 25<sup>th</sup> and 75<sup>th</sup> percentile of the image array, respectively.

- Range

$$\mathit{range} = \max(\mathbf{X}) - \min(\mathbf{X})$$

Range is the range of gray values in the ROI.

- Mean Absolute Deviation (MAD)

$$MAD = \frac{1}{N_p} \sum_{i=1}^{N_p} |\mathbf{X}(i) - \bar{X}|$$

Mean Absolute Deviation is the average distance between each intensity value and the average value of the image array.

- Robust Mean Absolute Deviation (rMAD)

$$rMAD = \frac{1}{N_{10-90}} \sum_{i=1}^{N_{10-90}} |\mathbf{X}_{10-90}(i) - \bar{X}_{10-90}|$$

Robust Mean Absolute Deviation, determined on the subset of the image array with gray levels in between, or equal to the 10th and 90th percentile, is the mean deviation of all intensity values from the mean value.

- Root Mean Squared (RMS)

$$RMS = \sqrt{\frac{1}{N_p} \sum_{i=1}^{N_p} (\mathbf{X}(i) + c)^2}$$

Root Mean Squared represents the average of all squared intensity levels. It is a different way to express how large the image values are. A higher value of  $c$  magnifies the influence of volume-confounding on this characteristic, which is volume-confounded.

- Standard Deviation

$$standard\ deviation = \sqrt{\frac{1}{N_p} \sum_{i=1}^{N_p} (\mathbf{X}(i) - \bar{X})^2}$$

Standard Deviation measures the degree of variance or dispersion from the mean value.

- Skewness

$$skewness = \frac{\mu_3}{\sigma^3} = \frac{\frac{1}{N_p} \sum_{i=1}^{N_p} (\mathbf{X}(i) - \bar{X})^3}{\left(\sqrt{\frac{1}{N_p} \sum_{i=1}^{N_p} (\mathbf{X}(i) - \bar{X})^2}\right)^3}$$

where  $\mu_3$  is the 3<sup>rd</sup> central moment.

Skewness measures the asymmetry of the distribution of values around the mean value. This number may be positive or negative depending on where the tail is extended and where the distribution's bulk is concentrated.

- Kurtosis

$$kurtosis = \frac{\mu_4}{\sigma^4} = \frac{\frac{1}{N_p} \sum_{i=1}^{N_p} (\mathbf{X}(i) - \bar{X})^4}{\left(\frac{1}{N_p} \sum_{i=1}^{N_p} (\mathbf{X}(i) - \bar{X})^2\right)^2}$$

where  $\mu_4$  is the 4<sup>th</sup> central moment.

Kurtosis is a metric for 'peakedness' in the value distribution inside the ROI of an image. A greater kurtosis indicates that the distribution's bulk is centered around the distribution's tails rather than its mean. A smaller kurtosis suggests the opposite, that the majority of the distribution is focused on a peak close to the mean value.

- Variance

$$variance = \frac{1}{N_p} \sum_{i=1}^{N_p} (\mathbf{X}(i) - \bar{X})^2$$

The mean of the squared deviations of each intensity value from the mean value is known as the variance. This is a measurement of the distribution's spread around the mean.

- Uniformity

$$uniformity = \sum_{i=1}^{N_g} p(i)^2$$

Uniformity is a measurement of the squares of all the intensity values. This is an indicator of how homogeneous the image array is, with higher uniformity denoting more homogeneity or a narrower range of discrete intensity values.

2.1.2.2.3 Texture features

Texture features represent spatial arrangement and patterns of voxels in the ROIs and can be derived from the matrix that represents the relationships between neighboring pixels or voxels such as the gray-level co-occurrence matrix (GLCM), gray-level run length matrix (GLRLM), gray-level size zone matrix (GLSZM), neighboring gray tone difference matrix (NGTDM), and gray level dependence matrix (GLDM). The information of texture features was about the texture, heterogeneity, and structural characteristics of the underlying tissue or lesion. There are so many features in this class, so we only show the example features in the GLCM group.

Gray Level Co-occurrence Matrix (GLCM) Features

The second-order joint probability function of an image region limited by the mask is described by a Gray Level Co-occurrence Matrix (GLCM) of size  $N_g \times N_g$ , which is defined as  $\mathbf{P}(i, j | \delta, \theta)$ . The  $(i, j)^{th}$  element of this matrix represents the frequency with which two pixels in the picture, separated by a distance of  $\delta$  pixels along angle  $\theta$ , have the combination of levels  $i$  and  $j$ . The distance  $\delta$  according to the infinity norm is what is meant when referring to the distance from the center voxel. This produces two neighbors for each of the 13 3D angles for  $\delta=1$  (26-connectivity) and 98-connectivity for  $\delta=2$  (49 unique angles). These are the notation for the GLCM features equation.

- $\epsilon$  represents an arbitrarily small positive number ( $2.2 \times 10^{-16}$ ).
- $\mathbf{P}(i, j)$  is the co-occurrence matrix for variables  $\delta$  and  $\theta$ .
- $p(i, j)$  is the matrix of normalized co-occurrence.
- $N_g$  is the number of discrete intensity levels in the image.
- $p_x(i)$  are the rows with marginal probabilities.
- $p_y(j)$  are the column with marginal probabilities.
- $\mu_x$  is the average intensity of the  $p_x$  gray level.
- $\mu_y$  is the average intensity of the  $p_y$  gray level.
- $\sigma_x$  is the standard deviation of  $p_x$ .
- $\sigma_y$  is the standard deviation of  $p_y$ .
- $H_X$  is the entropy of  $p_x$ .
- $H_Y$  is the entropy of  $p_y$ .
- $H_{XY}$  is the entropy of  $p(i, j)$ .

Radiomic features in the GLCM group were shown as follows.

- Autocorrelation

$$autocorrelation = \sum_{i=1}^{N_g} \sum_{j=1}^{N_g} p(i, j)ij$$

The degree of texture fineness and coarseness is measured by Autocorrelation.

- Joint Average

$$joint\ average = \mu_x = \sum_{i=1}^{N_g} \sum_{j=1}^{N_g} p(i, j)i$$

Joint Average is the mean gray level intensity of the  $i$  distribution.



- Cluster Prominence

$$cluster\ prominence = \sum_{i=1}^{N_g} \sum_{j=1}^{N_g} (i + j - \mu_x - \mu_y)^4 p(i, j)$$

A measure of the skewness and asymmetry of the GLCM is cluster prominence. While a lower number denotes a peak close to the mean and less fluctuation around the mean, a larger value denotes more asymmetry around the mean.

- Cluster Shade

$$cluster\ shade = \sum_{i=1}^{N_g} \sum_{j=1}^{N_g} (i + j - \mu_x - \mu_y)^3 p(i, j)$$

The skewness and homogeneity of the GLCM are assessed using Cluster Shade. Greater asymmetry regarding the mean is implied by a higher cluster shade.

- Cluster Tendency

$$cluster\ tendency = \sum_{i=1}^{N_g} \sum_{j=1}^{N_g} (i + j - \mu_x - \mu_y)^2 p(i, j)$$

A measure of clusters of voxels with comparable gray-level values is called cluster tendency.

- Contrast

$$contrast = \sum_{i=1}^{N_g} \sum_{j=1}^{N_g} (i - j)^2 p(i, j)$$

The local intensity variation is measured via contrast, which favors values other than the diagonal (i, j). A larger value is correlated with a wider range of intensity levels between adjacent voxels.

- Correlation

$$\text{correlation} = \frac{\sum_{i=1}^{N_g} \sum_{j=1}^{N_g} p(i, j) ij - \mu_x \mu_y}{\sigma_x(i) \sigma_y(j)}$$

The correlation value, which ranges from 0 (completely uncorrelated) to 1, depicts the linear relationship between the gray level values and the corresponding voxels in the GLCM.

- Difference Average

$$\text{difference average} = \sum_{k=0}^{N_g-1} k p_{x-y}(k)$$

Difference Average examines how frequently pairs with similar intensity values occur compared to pairs with different intensity values.

- Difference Entropy

$$\text{difference entropy} = \sum_{k=0}^{N_g-1} p_{x-y}(k) \log_2 (p_{x-y}(k) + \epsilon)$$

Difference Entropy quantifies the level of randomness or variability in the differences between neighboring intensity values.

- Difference Variance

$$\text{difference variance} = \sum_{k=0}^{N_g-1} (k - DA)^2 p_{x-y}(k)$$

Difference Variance is a metric for assessing the heterogeneity within a set of intensity level pairs, assigning greater significance to pairs that exhibit larger deviations from the average.

- Joint Energy

$$\text{joint energy} = \sum_{i=1}^{N_g} \sum_{j=1}^{N_g} (p(i, j))^2$$

Energy is a metric that evaluates the presence of uniform patterns in an image. A higher Energy indicates a greater abundance

of intensity value pairs that are adjacent to each other with increased frequency.

- Joint Entropy

$$\text{joint entropy} = - \sum_{i=1}^{N_g} \sum_{j=1}^{N_g} p(i, j) \log_2 (p(i, j) + \epsilon)$$

Joint entropy is a metric that quantifies the level of randomness or variability in the intensity values of neighboring pixels.

- Informational Measure of Correlation (IMC) 1

$$\text{IMC 1} = \frac{HXY - HXY1}{\max\{HX, HY\}}$$

IMC1 evaluates the correlation between the probability distributions of variables  $i$  and  $j$ . When  $HXY - HXY1$  is divided by the greater of the two marginal entropies,  $\text{IMC1} = -1$  is obtained, with  $HX = HY = I(i, j)$  in the situation of total dependency (not necessarily uniform; low complexity).

- Informational Measure of Correlation (IMC) 2

$$\text{IMC 2} = \sqrt{1 - e^{-2(HXY2 - HXY)}}$$

IMC2 evaluates the relationship between the probability distributions of  $i$  and  $j$  as well (quantifying the texture's complexity).

It's interesting to observe that the two distributions' mutual information is represented by  $HXY2 - HXY \geq 0$  and that  $HXY1 = HXY2$ . IMC2 thus has a range of  $[0, 1]$ , where 0 represents the situation of two independent distributions (no mutual information) and 1 represents the case of two fully dependent and uniform distributions (maximum mutual information, equal to  $\log_2(N_g)$ ). In the latter scenario, the highest value then approaches 1 and is equivalent to  $\sqrt{1 - e^{-2 \log_2(N_g)}}$ .

- Inverse Difference Moment (IDM)

$$IDM = \sum_{k=0}^{N_g-1} \frac{p_{x-y}(k)}{1+k^2}$$

IDM, which assesses the local homogeneity of an image, utilizes weights that are inversely related to the Contrast weights. These weights decrease exponentially as the distance from the diagonal ( $i = j$ ) in the GLCM increases.

- Maximal Correlation Coefficient (MCC)

$$MCC = \sqrt{\text{second largest eigenvalue of } Q}$$

$$Q(i, j) = \sum_{k=0}^{N_g} \frac{p(i, k)p(j, k)}{p_x(i)p_y(k)}$$

The Maximal Correlation Coefficient is utilized as a metric to quantify the complexity of the texture, with values ranging from 0 to 1. Each GLCM matrix has shape  $(N_g, N_g)$  in the case of a flat region, yielding a single eigenvalue. In this instance, a random value of 1 is returned.

- Inverse Difference Moment Normalized (IDMN)

$$IDMN = \sum_{k=0}^{N_g-1} \frac{p_{x-y}(k)}{1 + \left(\frac{k^2}{N_g^2}\right)}$$

IDMN is a metric for an image's local homogeneity. IDMN weights (which decrease exponentially from the diagonal  $i = j$  in the GLCM) are the opposite of Contrast weights. In contrast to Homogeneity<sup>2</sup>, IDMN divides the square of the total number of discrete intensity values to normalize the square of the difference between adjacent intensity values.

- Inverse Difference (ID)

$$ID = \sum_{k=0}^{N_g-1} \frac{p_{x-y}(k)}{1+k}$$

The local homogeneity of an image can also be measured by ID. The denominator will remain small when the gray levels are more consistent, leading to a greater average value.

- Inverse Difference Normalized (IDN)

$$IDN = \sum_{k=0}^{N_g-1} \frac{p_{x-y}(k)}{1 + \left(\frac{k}{N_g}\right)}$$

IDN is a different metric for gauging an image's regional homogeneity. IDN, as contrast to Homogeneity1, divides the total number of discrete intensity values to normalize the difference between the neighboring intensity values.

- Inverse Variance

$$inverse\ variance = \sum_{k=1}^{N_g-1} \frac{p_{x-y}(k)}{k^2}$$

If the value of k is 0, then the result is undefined.

- Maximum Probability

$$maximum\ probability = \max(p(i, j))$$

Maximum Probability is the most frequent occurrence of a pair of adjacent intensity values.

- Sum Average

$$sum\ average = \sum_{k=2}^{2N_g} p_{x+y}(k)k$$

Sum Average examines the correlation between the occurrences of pairs with lower and higher intensity levels.

- Sum Entropy

$$sum\ entropy = \sum_{k=2}^{2N_g} p_{x+y}(k) \log_2 (p_{x+y}(k) + \epsilon)$$

Sum Entropy is the total of local intensity value variations.

- Sum of Squares

$$sum\ squares = \sum_{i=1}^{N_g} \sum_{j=1}^{N_g} (i - \mu_x)^2 p(i, j)$$

Sum of Squares is a measurement of the distribution of adjacent intensity level pairs around the GLCM's mean intensity level.

#### 2.1.2.2.4 Wavelet features

Wavelet features are the features that using wavelet transforms to decompose the image into sub bands, representing different frequency components. The resulting wavelet coefficients capture details at different scales and orientations, enabling the extraction of texture and structural information from the image.

### 2.1.3 Inter-observer variability

#### 2.1.3.1 Dice coefficient

Dice coefficient is a method that measures the spatial overlap between two segmentations, A and B target regions, and is defined as

$$Dice(A, B) = \frac{2 (|A \cap B|)}{|A| + |B|}$$

where  $|A|$  and  $|B|$  is the area of A and B, while  $|A \cap B|$  is the area of the intersection between the target regions A and B<sup>(14)</sup>.

#### 2.1.3.2 Intraclass correlation coefficient (ICC)

Intraclass correlation coefficient is used to measure the reliability of ratings in studies where there are two or more raters. This research uses the two-

way mixed single measures intraclass correlation coefficient to analyze radiomics features which is given by

$$ICC(3, k) = \frac{MS_R - MS_E}{MS_R}$$

where  $MS_R$  is the mean square for rows of data,  $MS_E$  is the mean square for error of data, and  $k$  is the number of raters or measurements which is five in this research.

### 2.1.3.3 Coefficient of variation (CV)

The coefficient of variation is a useful measure for evaluating the relative variability of data sets, calculated as the ratio of the standard deviation to the mean, and provides insight into the level of variability in relation to the mean of the data population.

## 2.2 Review of related literatures

**Chang ATY, Tan LT, Duke S, Ng WT. (2017)**<sup>(15)</sup> reviewed the literature on target volume delineation (TVD) variability and its impact on dosimetry. The reviewer found that there were very few in various publications that investigated the causes of the variability. The outstanding paper that evaluated dosimetric impact of TVD variability in target and OAR contouring on dosimetry is Vinod et al.<sup>(16)</sup> They identified 25 studies, of which 8 studies found a significant impact on OAR dose-volume histograms (DVH) and 8 studies found statistically significant differences in OAR doses. Moreover, Vinod classified the analysis of the dosimetric impact of TVD variability into three broad methods. But the relevant method for our study was the method of Van de Steen et al.<sup>(17)</sup> They generated plans that are optimized to a particular delineated volume and then applied to all other volumes to assess dosimetry in lung cancer with 5 clinicians on the planning CT scans of 8 patients. The study reported an inter-observer variation in the dimensions of the primary tumor of up to 4.2 cm (transverse), 7.9 cm (cranio-caudal), and 5.4 cm (antero-posterior), and there is only 63% of tumor regions were delineated by the clinicians. Therefore, we can conclude that TVD variability is a significant problem in radiotherapy in clinical trials.

**Pavic M, Bogowicz M, Würms X, et al. (2018)**<sup>(18)</sup> studied 3 tumor types including Head and neck squamous cell carcinoma (HNSCC), Non-small cell lung cancers (NSCLC) and Malignant pleural mesothelioma (MPM) with 11 tumors for each type in diagnostic PET/CT images to investigate the impact of inter-observer variability (IOV) in tumor delineation on the reliability of radiomic features. They studied the delineation variability by using the median Dice coefficient. After that they extracted radiomics features into 4 subgroups including to determine stability rate. Then they applied 2 methods (merging and averaging matrices) for texture features in GLCM and GLRLM to investigate whether one of them is characterized by a superior inter-observer stability. From the results, the stability rate of radiomic features was correlated with the median Dice coefficient, and a similar correlation was observed for each feature subgroup. Furthermore, the method of averaging texture features in the end resulted in a slightly higher percentage of stable features. Finally, this study showed differences in tumor delineation influences results of radiomics analysis and for a tumor site with large inter-observer delineation differences can still find some stable features lead to reducing number of features for radiomic analysis in the future.



## CHAPTER III

### RESEARCH METHODOLOGY

#### 3.1 Research designs

The type of research in this proposal is a retrospective descriptive study in a patient with nasopharyngeal carcinoma.

#### 3.2 Research design model

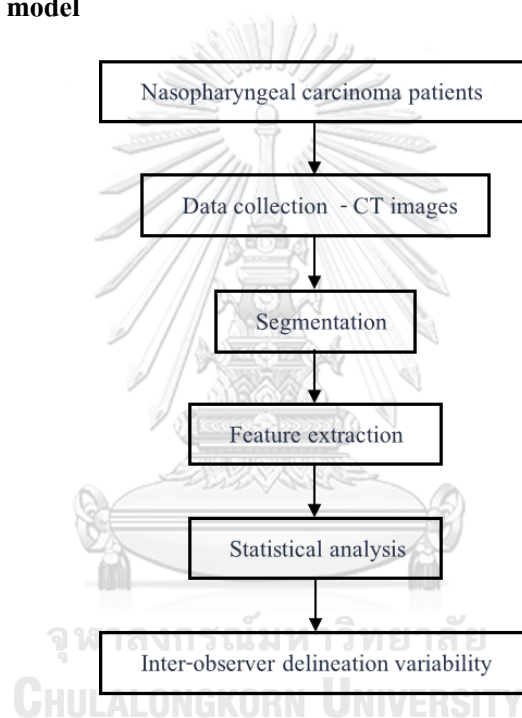


**Figure 3** Research design

#### 3.3 Conceptual framework

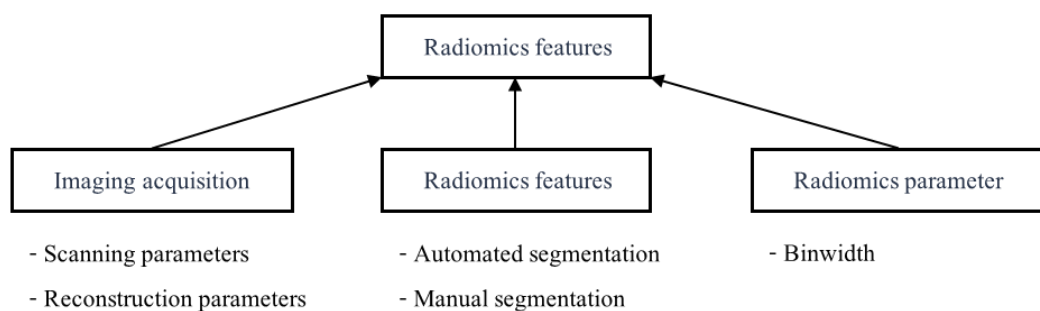


**Figure 4** Conceptual framework

### 3.4 Key Word

Nasopharyngeal cancer, Radiomics, Inter-observer variability, Dice coefficient, ICC, CV

### 3.5 The sample

#### 3.5.1 Target population

Data sets of all CT images of patients newly diagnosed with Nasopharyngeal carcinoma at King Chulalongkorn Memorial Hospital (KCMH).

#### 3.5.2 Sample population

The CT images data set of patients who are newly diagnosed with Nasopharyngeal carcinoma at KCMH who met the eligible criteria.

#### 3.5.3 Eligible criteria

##### 3.5.3.1 The inclusion criteria

- a) They were recently diagnosed with Nasopharyngeal carcinoma at KCMH between July 2010 and July 2021.
- b) They have no evidence of distant metastases.
- c) They have at least 3 years of follow-up time.
- d) They undergo CT and MRI-simulation.
- e) They received IMRT or VMAT with chemotherapy.
- f) They have the pretreatment plasma Epstein-Barr virus (EBV) level.

In this study, clinical data of sex, age, tumor staging will be used. Staging classification is performed according to the 8th edition of the American Joint Committee on Cancer (AJCC)<sup>(19)</sup>.

##### 3.5.3.2 The exclusion criteria

- a) Streak artifact from dental amalgam or other metallic foreign bodies in the vicinity of region of interest on CT images

- b) Other artifacts on the CT or MRI images that may interfere with intensity analysis.

Due to the data collected in this research based on Intarak et al. <sup>(9)</sup> that have inclusion and exclusion criteria as mentioned above, therefore we will use the same criteria as them.

#### 3.5.4 Sample size determination

This study used all data sets of patients newly diagnosed with Nasopharyngeal carcinoma at KCMH. However, there is no appropriate formula for our data, so we will use a number of data comparable to the reference research <sup>(18)</sup>.

### 3.6 Materials

#### 3.6.1 Computed tomography simulator

CT images were collected with CT simulator at division of radiation oncology, King Chulalongkorn Memorial Hospital (Somatom Definition AS, Siemens Medical Solutions, Erlangen, Germany).



**Figure 5** CT simulator, Somatom Definition AS, Siemens Medical Solutions, Erlangen, Germany

### 3.6.2 Pyradiomics software 3.0.1

Pyradiomics is an open-source Python package for the extraction of radiomics data from medical images such as CT images. SimpleITK is utilized for the tasks of loading and preprocessing images, then transformed into numpy arrays, which are employed in various calculations involving multiple feature classes. This study used Pyradiomics software version 3.0.1 to extract radiomics features from CT images.



**Figure 6** Pyradiomics software

### 3.6.3 3D Slicer software

The 3D Slicer software is an open-source software for image visualization, image processing, image segmentation, and analysis of medical images by contributions from an international community of scientists worldwide. This study used the 3D Slicer software version 5.0.3 to convert CT images to other formats; i.e.. nrrd.

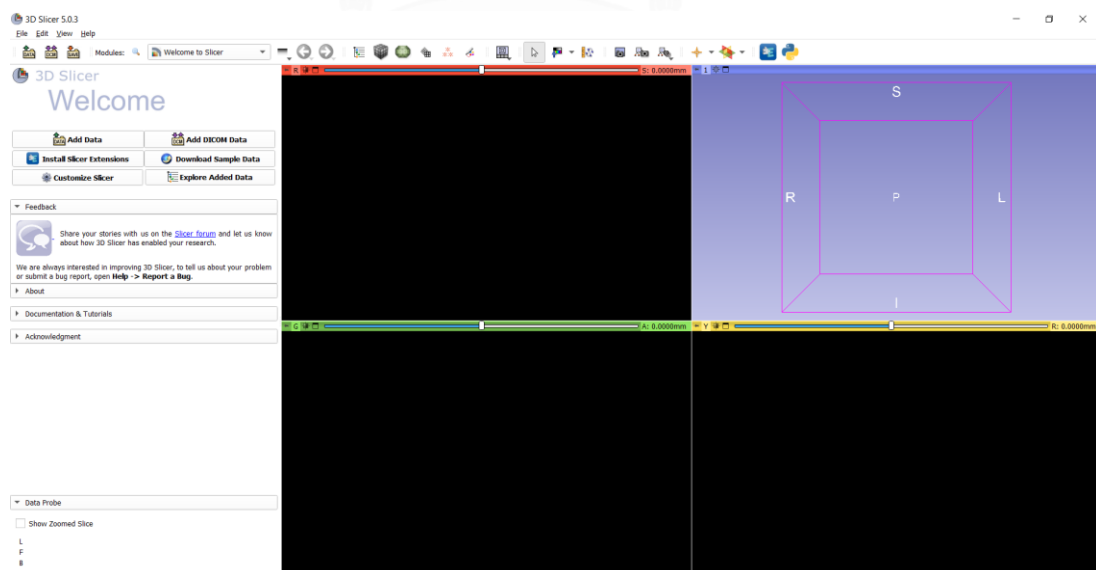


**Figure 7** 3D Slicer software version 5.0.3

### 3.6.4 MATLAB software

MATLAB (MATrix LABORatory) is a high-performance software designed specifically for engineers and scientists to analyze technical computing systems using the matrix-based language developed by MathWorks. This study used the MATLAB software version R2022b to calculate the Dice coefficient.

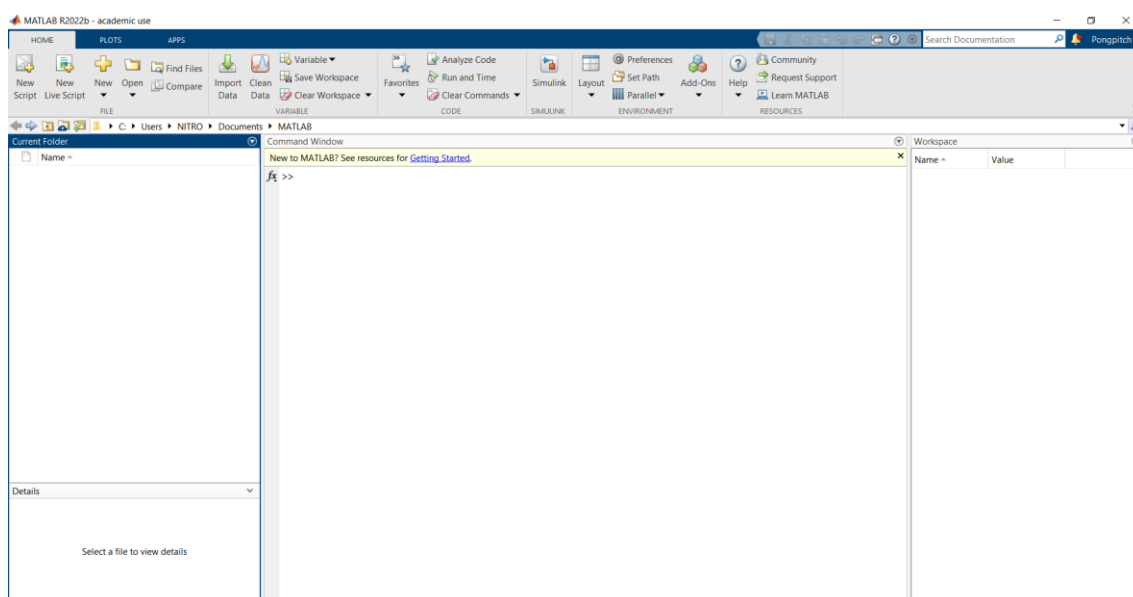


**Figure 8** MATLAB software version R2022b

### 3.6.5 Python

Python is a free high-level programming language. It is a general-purpose programming program and supports multiple paradigms. Since being easy to learn and friendly for beginners, Python has become one of the most popular programming languages in the world for many tasks. One common task is data analysis.

## 3.7 Methods

### 3.7.1 Patient data collection

This study was a retrospective study. Therefore, we collected data from patients who were newly diagnosed with Nasopharyngeal carcinoma (NPC) at King Chulalongkorn Memorial Hospital between July 2010 and July 2021. All CT images were acquired by using CT simulator at division of radiation oncology. The scanning parameters were as follows: 120 kVp, 325 mAs, FOV 600x600 mm, 2- and 3-mm slice thickness. Image

acquisition was performed after fifty-nine seconds after 75 ml Omnipaque 300, contrast media, were injected.

### 3.7.2 Tumor delineation

Thirty patients who undergo inclusion criteria will be randomly selected. For each patient, the gross tumor volume (GTV) of the primary tumor in the nasopharynx was manually contoured on CT images by five different experienced radiation oncologists. The experience depends on the duration after receiving the Diploma from Thai Board of Radiation Oncology.

### 3.7.3 Radiomics features extraction

CT images were analyzed into 1288 radiomic features per GTV by using Pyradiomics version 3.0.1. The extracted features will be classified into four feature classes: Shape-based class (14), First-order intensity class (18), Texture-based class (73), and Wavelet-based class (1183).

Moreover, the binwidth parameter during the extraction process was the parameter that influences the features, and it was varied into three values: 0.05, 0.1 and 0.2<sup>(20)</sup>.

### 3.7.4 Inter-observer variability analysis

To measure inter-observer variability, the analysis was divided into three parts including Dice coefficient that represents the difference between two targets, Intraclass correlation coefficient (ICC) and coefficient of variation (CV) that show the consistency of features measurements.

#### 3.7.4.1 Dice coefficient

To determine the similarity between two segmented images, the Dice coefficient was used to measure the spatial overlap of ROIs of CT images.

#### 3.7.4.2 Intraclass correlation coefficient (ICC)

The robust radiomics features should be consistent between observers. Therefore, the ICC was used to assess the correlation of radiomic features from

multiple ROIs. This study selected the ICC threshold at 0.8 to determine the stable feature<sup>(18)</sup>.

#### 3.7.4.3 Coefficient of variation (CV)

The other method to evaluate the relative variability of the features is CV. The threshold was selected at 10%, giving excellent reproducibility<sup>(21)</sup>.

### 3.8 Statistical analysis

The variation in tumor delineation in each patient was determined by the Dice coefficient. Moreover, the variation of radiomics features was analyzed using the two-way mixed single measures intraclass correlation coefficient (ICC(3,1))<sup>(22)</sup> and coefficient of variation.

### 3.9 Ethical consideration

This study requires patient data; therefore, the research study was approved by Institutional Review Board (IRB) of the Faculty of Medicine, Chulalongkorn University, Bangkok, Thailand (IRB No. 0419/65). The certificate is shown in APPENDIX A.

## CHAPTER IV

### RESULTS

#### 4.1 The variation of tumor delineation

##### 4.1.1 Dice coefficient

The GTV of the primary tumor from 30 patients was drawn manually by five radiation oncologists. The similarity of each GTV was determined by the Dice coefficient. The mean Dice coefficient is  $0.72 \pm 0.15$  and the median Dice coefficient is 0.77. Each Dice coefficient from five radiation oncologists was shown in Table 2. The results showed that doctor 1 who has the most experience was drawn differently from other doctors.

##### 4.1.2 Determination of stable radiomics features

In this study, the stable features were classified into two aspects, that is, ICC and %CV. This study uses the threshold to determine stable features in terms of ICC is greater than 0.8<sup>(18)</sup> and in terms of %CV is less than 10<sup>(20)</sup>. Moreover, the binwidth parameter was applied to the results of the stable features.

In the inter-observer stability test, the percentage of stable features in each class is shown in Figure 9. The overall stable features percentages are 70.73, 70.26 and 67.78 at binwidth equal to 0.05, 0.1 and 0.2 respectively. In the shape and first-order classes, the percentage of stable features is 92.86% and 77.78% for all binwidths. The percentage of stable features in texture class is 78.08%, 73.97% and 69.86% and the percentage of stable features in wavelet class is 69.91%, 69.65% and 67.20% at binwidth equal to 0.05, 0.1 and 0.2 respectively. Figure 10 shows the percentage of stable features in each class compared to the results of Pavic M et al. in HNSCC<sup>(18)</sup> while varying the binwidths. The average percentage of stable features was 92.86%, 77.78%, 73.97%, and 68.92% in the shape, first-order, texture, and wavelet classes, respectively.



**Table 2** Dice coefficient of five radiation oncologists from the data sets of 30 patients

| Pt.ID/Dr. | 1x2  | 1x3  | 1x4  | 1x5  | 2x3  | 2x4  | 2x5  | 3x4  | 3x5  | 4x5  |
|-----------|------|------|------|------|------|------|------|------|------|------|
| 1         | 0.01 | 0.01 | 0.01 | 0.01 | 0.85 | 0.84 | 0.85 | 0.81 | 0.99 | 0.81 |
| 2         | 0.34 | 0.32 | 0.32 | 0.31 | 0.83 | 0.79 | 0.84 | 0.83 | 0.97 | 0.84 |
| 3         | 0.65 | 0.48 | 0.66 | 0.66 | 0.72 | 0.81 | 0.81 | 0.72 | 0.72 | 0.99 |
| 4         | 0.32 | 0.35 | 0.34 | 0.32 | 0.76 | 0.81 | 0.99 | 0.88 | 0.76 | 0.81 |
| 5         | 0.59 | 0.37 | 0.38 | 0.59 | 0.67 | 0.70 | 0.99 | 0.91 | 0.67 | 0.70 |
| 6         | 0.29 | 0.27 | 0.30 | 0.31 | 0.86 | 0.89 | 0.77 | 0.87 | 0.75 | 0.79 |
| 7         | 0.71 | 0.63 | 0.68 | 0.71 | 0.84 | 0.89 | 0.99 | 0.87 | 0.84 | 0.89 |
| 8         | 0.60 | 0.62 | 0.57 | 0.62 | 0.88 | 0.85 | 0.88 | 0.86 | 0.99 | 0.86 |
| 9         | 0.54 | 0.49 | 0.44 | 0.41 | 0.83 | 0.75 | 0.77 | 0.79 | 0.77 | 0.67 |
| 10        | 0.54 | 0.58 | 0.59 | 0.56 | 0.85 | 0.83 | 0.95 | 0.85 | 0.86 | 0.86 |
| 11        | 0.63 | 0.74 | 0.73 | 0.74 | 0.79 | 0.74 | 0.78 | 0.91 | 0.99 | 0.92 |
| 12        | 0.70 | 0.55 | 0.52 | 0.53 | 0.78 | 0.75 | 0.76 | 0.84 | 0.84 | 0.95 |
| 13        | 0.70 | 0.56 | 0.58 | 0.56 | 0.79 | 0.83 | 0.79 | 0.86 | 0.99 | 0.86 |
| 14        | 0.80 | 0.69 | 0.83 | 0.80 | 0.74 | 0.85 | 0.99 | 0.75 | 0.74 | 0.85 |
| 15        | 0.74 | 0.73 | 0.73 | 0.70 | 0.85 | 0.86 | 0.83 | 0.85 | 0.82 | 0.92 |
| 16        | 0.86 | 0.85 | 0.86 | 0.85 | 0.84 | 0.82 | 0.84 | 0.88 | 0.99 | 0.88 |
| 17        | 0.88 | 0.86 | 0.70 | 0.70 | 0.92 | 0.70 | 0.71 | 0.70 | 0.70 | 0.89 |
| 18        | 0.05 | 0.06 | 0.07 | 0.07 | 0.60 | 0.76 | 0.76 | 0.73 | 0.73 | 0.99 |
| 19        | 0.52 | 0.44 | 0.43 | 0.44 | 0.86 | 0.84 | 0.86 | 0.86 | 0.99 | 0.86 |
| 20        | 0.70 | 0.69 | 0.67 | 0.63 | 0.75 | 0.71 | 0.77 | 0.81 | 0.70 | 0.68 |
| 21        | 0.44 | 0.44 | 0.45 | 0.45 | 0.75 | 0.72 | 0.72 | 0.74 | 0.74 | 1.00 |
| 22        | 0.80 | 0.68 | 0.71 | 0.80 | 0.79 | 0.80 | 0.99 | 0.81 | 0.79 | 0.80 |
| 23        | 0.54 | 0.49 | 0.50 | 0.50 | 0.79 | 0.73 | 0.73 | 0.73 | 0.73 | 0.99 |
| 24        | 0.56 | 0.45 | 0.49 | 0.45 | 0.75 | 0.78 | 0.75 | 0.90 | 0.99 | 0.90 |
| 25        | 0.71 | 0.64 | 0.64 | 0.51 | 0.78 | 0.76 | 0.62 | 0.70 | 0.62 | 0.54 |
| 26        | 0.80 | 0.83 | 0.83 | 0.81 | 0.85 | 0.86 | 0.84 | 0.88 | 0.95 | 0.87 |
| 27        | 0.78 | 0.84 | 0.84 | 0.77 | 0.76 | 0.78 | 0.73 | 0.82 | 0.80 | 0.76 |
| 28        | 0.84 | 0.86 | 0.89 | 0.72 | 0.86 | 0.82 | 0.75 | 0.86 | 0.71 | 0.74 |
| 29        | 0.68 | 0.67 | 0.66 | 0.66 | 0.75 | 0.72 | 0.72 | 0.83 | 0.83 | 0.99 |
| 30        | 0.77 | 0.74 | 0.75 | 0.75 | 0.86 | 0.88 | 0.90 | 0.86 | 0.85 | 0.85 |

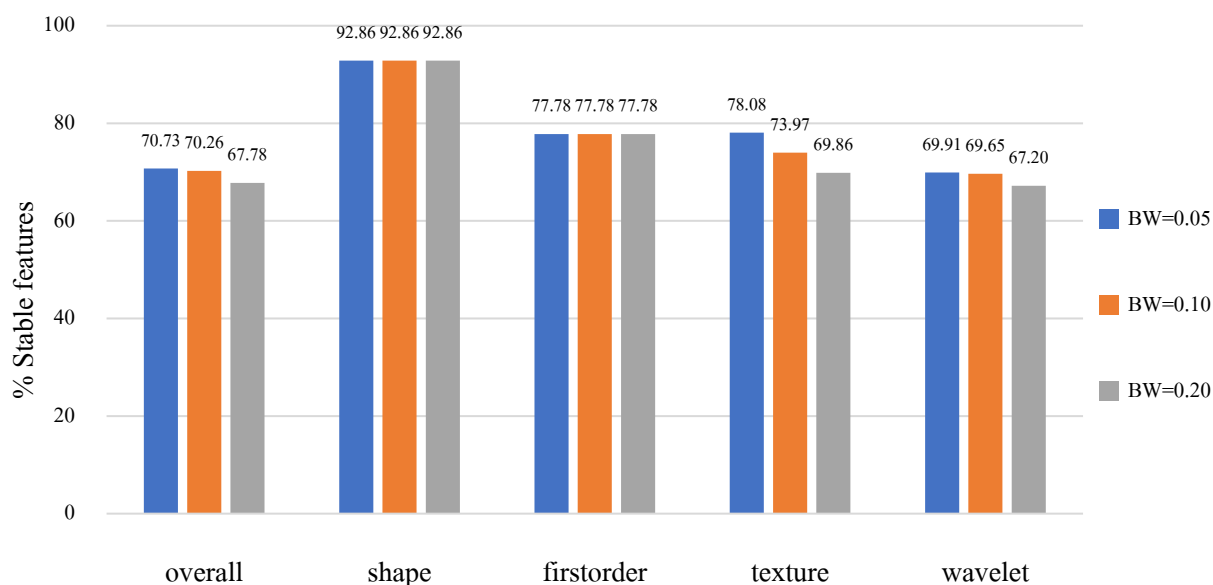


**Figure 9** The percentage of stable features in each class varying three binwidths.

Furthermore, we vary the %CV threshold to observe the relation between binwidths and the %CV threshold, as shown in Figure 11. It was found that the percentage was independent of the binwidth in the shape and first-order classes. The most stable class was the shape class at 85.71% of all %CV. From Figures 9 and 11, we can conclude that the binwidth of 0.05 yielded the highest percentage of stable features. As can be seen in Figure 12, the distribution of feature in shape class showed that the variation of stable feature in terms of %CV was found to be between 20 and 30. Figure 13 shows the proportion of stable radiomics features that were stable across all binwidths when comparing ICC and %CV. The shape class had the highest ICC at 92.86%, while the most stable feature was wavelet-LLH\_glszm\_ZoneEntropy in the wavelet class. Conversely, the most robust class in terms of %CV was the first-order class at 27.78%, and the most stable feature was wavelet-LLH\_firstorder\_RootMeanSquared in the wavelet class. Moreover, only 10.33% of the features were marked as stable in terms of ICC and %CV on average, with the most robust class being the first-order class at 16.67% and the most robust feature being wavelet-LLH\_glszm\_ZoneEntropy in the wavelet class. The lists of these stable features are shown in APPENDIX B. An example of the most stable features in each class that intersect with the highest ICC and the lowest %CV is shown in Table 3.

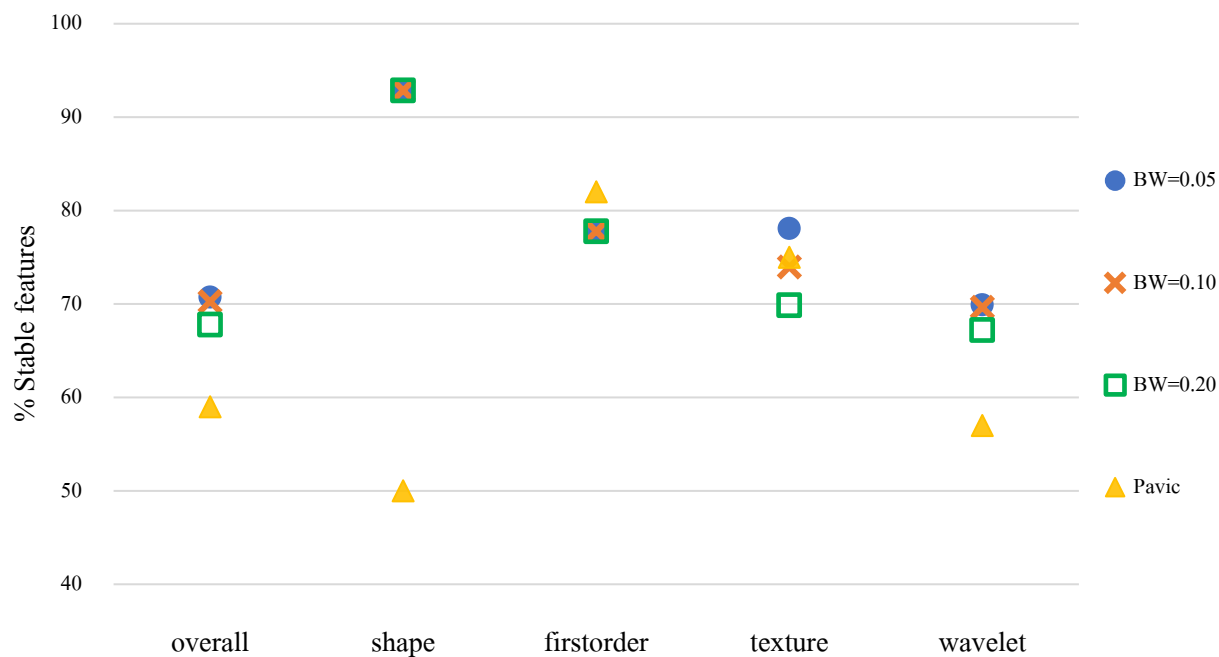


**Figure 10** The percentage of stable features compared to the results of Pavic M, et al. in HNSCC.

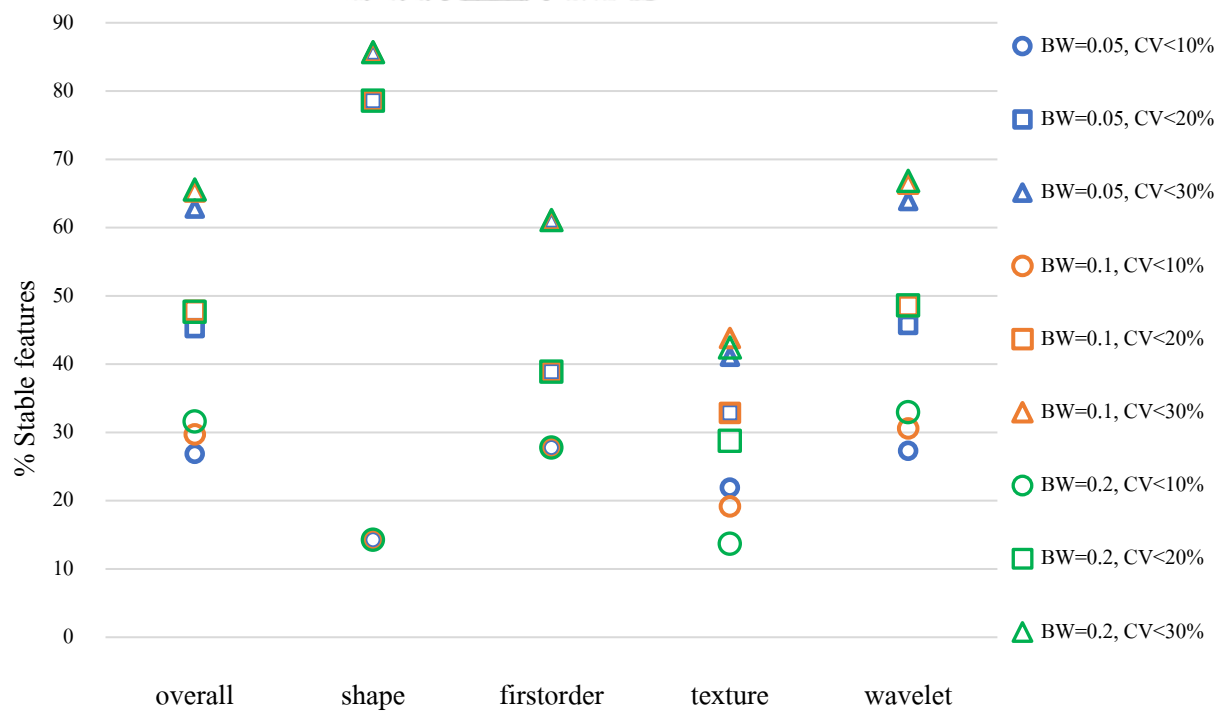


**Figure 11** The percentage of stable features in each class at %CV < 10,20,30

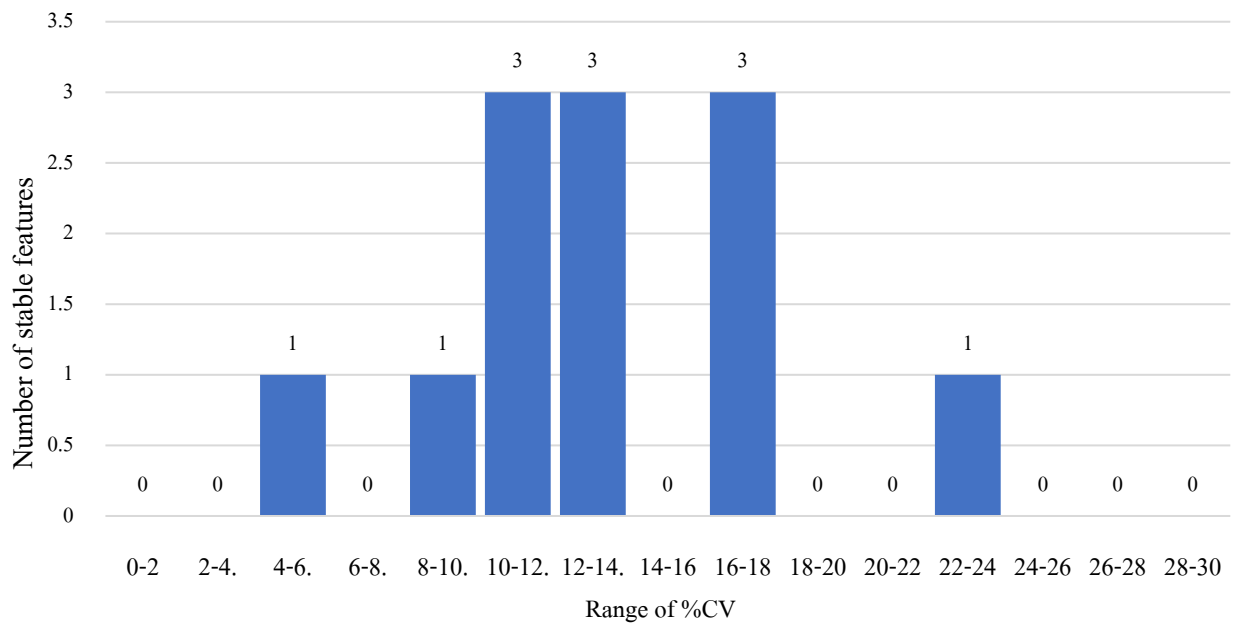


**Figure 12** The histogram of stable features in the shape class in range of %CV between 0 and 30

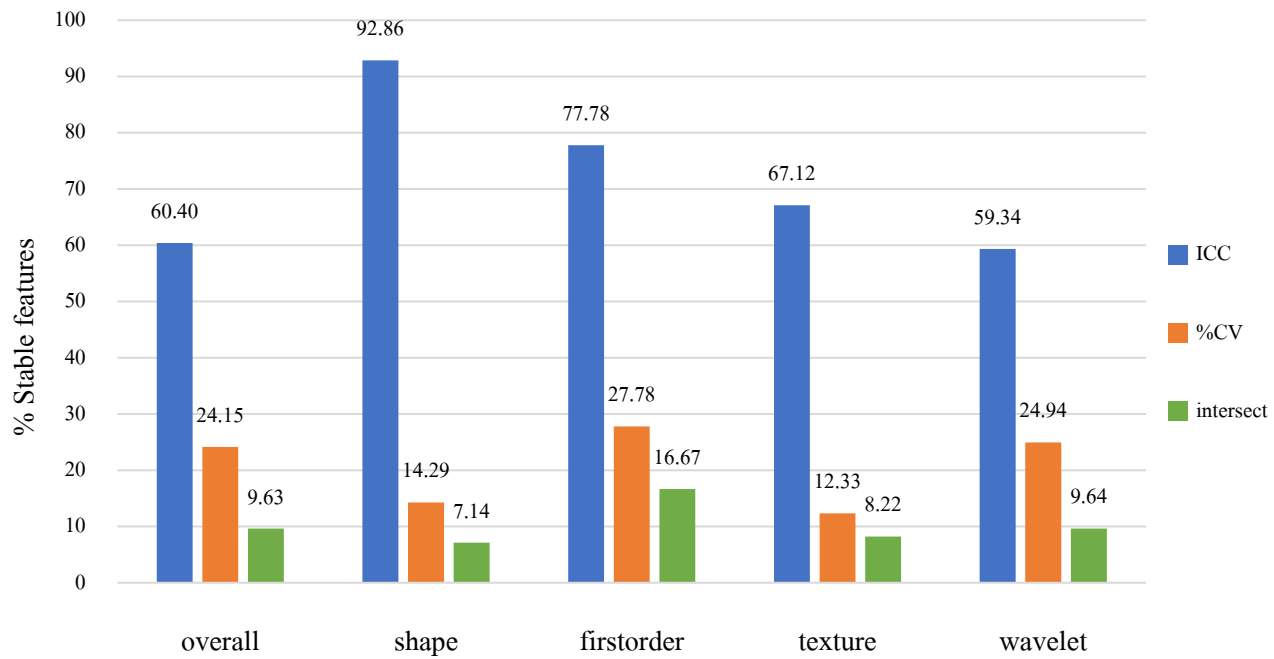


**Figure 13** The percentage of stable radiomics features among three binwidth compared between ICC and %CV

**Table 3** The most stable features with the highest ICC and lowest %CV in each class

| <b>Class</b>       | <b>ICC</b>                       | <b>%CV</b>                             |
|--------------------|----------------------------------|--|
| <b>Shape</b>       | original_shape_Elongation        | original_shape_Elongation              |
| <b>First-order</b> | original_firstorder_90Percentile | original_firstorder_RootMeanSquared    |
| <b>Texture</b>     | original_glszm_ZoneEntropy       | original_glcm_Id                       |
| <b>Wavelet</b>     | wavelet-LLH_glszm_ZoneEntropy    | wavelet-LLH_firstorder_RootMeanSquared |



## CHAPTER V

### DISCUSSION AND CONCLUSIONS

#### 5.1 Discussion

Radiomics is an effective tool in medical imaging that analyzes quantitative features from medical images to gain insights into disease characterization, treatment response prediction, and prognosis assessment. NPC is a complex disease with multifactorial etiology, histopathological heterogeneity, varied treatment approaches, geographic variation, and long-term management challenges. For this reason, the complexity of NPC makes it difficult to predict tumor prognostic from radiomics analysis that has feature selection is one of the most important steps. Feature selection involves the process of identifying and choosing the most relevant and informative features. There are several methods for feature selection that may vary depending on the dataset and analysis goals. Therefore, this research presents a method to determine the robust features that make it easier to select features in the future.

The discussion of the study can focus on the findings and implications of the Dice coefficient analysis and the determination of stable radiomics features. For Dice coefficient analysis, the study evaluated the similarity of manually drawn GTVs by five radiation oncologists using the Dice coefficient. The mean Dice coefficient was  $0.72 \pm 0.15$ , indicating a moderate level of agreement between oncologists. The median Dice coefficient was 0.77, suggesting that there was relatively good consensus in most cases. Moreover, the result was comparable to Pavic M, et al. with a median Dice coefficient in HNSCC of 0.72<sup>(18)</sup>. However, it was notable that doctor 1, who had the most experience, showed significant differences in their GTV delineation compared to other doctors. This finding raises the importance of consistent interpretation and delineation guidelines among physicians to ensure accurate and reliable results.

In determining the stable radiomics features, this study classified the stable features based on two aspects that are ICC and %CV. Stable features were defined using specific thresholds: ICC > 0.8 and %CV < 10. By applying these criteria, the study identified stable features across different classes, namely shape, first-order, texture, and wavelet. The inter-observer stability test showed that this study analyzed the percentage of stable features within each class, considering different binwidth values. The overall percentage of stable features ranged from 67.78% to 70.73% across different binwidths. Shape and first-order classes consistently showed the highest percentages of stable features, indicating their robustness. The texture and wavelet classes exhibited slightly lower percentages, suggesting a higher degree of variability within those feature classes. In the impact of %CV threshold and binwidth, the study investigated the relationship between %CV threshold and binwidth. The analysis revealed that the percentage of stable features was independent of the binwidth in the shape and first-order classes. The shape class exhibited the highest stability, with 85.71% of all %CV falling within the stable range. Furthermore, a binwidth of 0.05 yielded the highest percentage of stable features, indicating its suitability for analysis. Moreover, we examined the distribution of features within the shape class and identified a variation range of 20 to 30 in terms of %CV. However, this study determined the most stable features within each class based on the intersection of the highest ICC and the lowest %CV with the criteria of ICC value greater than 0.8 and %CV less than 10. Therefore, there were only a few features that met the criteria and can be used for the prediction model in the future. One of the limitations of this research was that the data collection was done in a single center with a small sample size.

Finally, this study's findings highlight the importance of standardized guidelines and consensus among radiation oncologists for consistent GTV delineation. The moderate agreement observed among oncologists underscores the need for ongoing training and quality assurance measures. Furthermore, the identification of stable radiomics features provides valuable insights for feature selection and reproducibility in future studies. The study's results contribute to the

growing body of knowledge in the field of radiomics and can guide researchers and clinicians in utilizing stable features for clinical decision-making and treatment planning.

## 5.2 Conclusions

This study mainly showed the performance and importance of radiomics in estimating the variability of tumor delineation in NPC patients. Moreover, the stable features of this study could be particularly useful as a tool for variation study in the future. This could help the radiation oncologist evaluate the performance of tumor delineation in the future.





## APPENDIX A

### THE APPROVAL OF INSTITUTIONAL REVIEW BOARD

Certificate of research approval from Institutional Review Board (IRB) of faculty of Medicine, Chulalongkorn University, Bangkok, Thailand. IRB no. 0419/65



COA No. 1039/2022

IRB No. 0419/65

#### INSTITUTIONAL REVIEW BOARD

Faculty of Medicine, Chulalongkorn University

1873 Rama 4 Road, Pathumwan, Bangkok 10330, Thailand, Tel 662-256-4493

#### Certificate of Expedited Review Approval

(COA No. 1039/2022)

The Institutional Review Board of the Faculty of Medicine, Chulalongkorn University, Bangkok, Thailand, has approved the following study which is to be carried out in compliance with the International guidelines for human research protection as Declaration of Helsinki, The Belmont Report, CIOMS Guideline and International Conference on Harmonization in Good Clinical Practice (ICH-GCP)

**Study Title** : Effect of Inter-observer Delineation Variability on Radiomics Features in Nasopharyngeal Cancer

**Study Code** : -

**Principal Investigator** : Mr. Pongpitch Panyura

**Affiliation of PI** : Department of Radiology,  
Faculty of Medicine, Chulalongkorn University.

**Review Method** : Expedited

**Continuing Report** : At least once annually or submit the final report if finished.

**Document Reviewed** :

1. Research Proposal Version 2.0 Date 20 July 2022
2. Protocol Synopsis Version 2.0 Date 20 July 2022
3. Case record form Version 1.0 Date 2 June 2022
4. Curriculum Vitae and GCP Training
  - Mr. Pongpitch Panyura

Approval granted is subject to the following conditions: (see back of this Certificate)



- Assist.Prof. Yothin Rakvongthai, Ph.D.

Signature Tada Sueblinwong  
(Emeritus Professor Tada Sueblinwong MD)  
Chairperson  
The Institutional Review Board

Signature Thananya Thongtan  
(Assistant Professor Thananya Thongtan, PhD)  
Member and Secretary  
The Institutional Review Board

Date of Approval : August 2, 2022  
Approval Expire Date : August 1, 2023

Approval granted is subject to the following conditions: (see back of this Certificate)

## APPENDIX B

### RESULTS OF STABLE RADIOMICS FEATURES

**Table 4** The stable features in shape class in terms of ICC

| Feature name                              | Binwidth |       |       |         |
|---|----------|-------|-------|---------|
|   | 0.05     | 0.10  | 0.20  | Average |
| CT_original_shape_Elongation              | 0.832    | 0.832 | 0.832 | 0.832   |
| CT_original_shape_Flatness                | 0.831    | 0.831 | 0.831 | 0.831   |
| CT_original_shape_LeastAxisLength         | 0.960    | 0.960 | 0.960 | 0.960   |
| CT_original_shape_MajorAxisLength         | 0.924    | 0.924 | 0.924 | 0.924   |
| CT_original_shape_Maximum2DDiameterColumn | 0.925    | 0.925 | 0.925 | 0.925   |
| CT_original_shape_Maximum2DDiameterRow    | 0.947    | 0.947 | 0.947 | 0.947   |
| CT_original_shape_Maximum2DDiameterSlice  | 0.901    | 0.901 | 0.901 | 0.901   |
| CT_original_shape_Maximum3DDiameter       | 0.925    | 0.925 | 0.925 | 0.925   |
| CT_original_shape_MeshVolume              | 0.942    | 0.942 | 0.942 | 0.942   |
| CT_original_shape_MinorAxisLength         | 0.954    | 0.954 | 0.954 | 0.954   |
| CT_original_shape_SurfaceArea             | 0.954    | 0.954 | 0.954 | 0.954   |
| CT_original_shape_SurfaceVolumeRatio      | 0.949    | 0.949 | 0.949 | 0.949   |
| CT_original_shape_VoxelVolume             | 0.942    | 0.942 | 0.942 | 0.942   |

**Table 5** The stable features in first-order class in terms of ICC

| Feature name                                       | Binwidth |       |       |         |
|--|----------|-------|-------|---------|
|  | 0.05     | 0.10  | 0.20  | Average |
| CT_original_firstorder_90Percentile                | 0.877    | 0.877 | 0.877 | 0.877   |
| CT_original_firstorder_Energy                      | 0.942    | 0.942 | 0.942 | 0.942   |
| CT_original_firstorder_Entropy                     | 0.952    | 0.948 | 0.944 | 0.948   |
| CT_original_firstorder_Kurtosis                    | 0.833    | 0.833 | 0.833 | 0.833   |
| CT_original_firstorder_Maximum                     | 0.958    | 0.958 | 0.958 | 0.958   |
| CT_original_firstorder_MeanAbsoluteDeviation       | 0.869    | 0.869 | 0.869 | 0.869   |
| CT_original_firstorder_Mean                        | 0.856    | 0.856 | 0.856 | 0.856   |
| CT_original_firstorder_Minimum                     | 0.927    | 0.927 | 0.927 | 0.927   |
| CT_original_firstorder_Range                       | 0.965    | 0.965 | 0.965 | 0.965   |
| CT_original_firstorder_RobustMeanAbsoluteDeviation | 0.812    | 0.812 | 0.812 | 0.812   |
| CT_original_firstorder_RootMeanSquared             | 0.856    | 0.856 | 0.856 | 0.856   |
| CT_original_firstorder_Skewness                    | 0.889    | 0.889 | 0.889 | 0.889   |
| CT_original_firstorder_TotalEnergy                 | 0.943    | 0.943 | 0.943 | 0.943   |
| CT_original_firstorder_Uniformity                  | 0.963    | 0.955 | 0.947 | 0.955   |

**Table 6** The stable features in texture class in terms of ICC

| Feature name  | Binwidth |       |       |         |
|---|----------|-------|-------|---------|
|   | 0.05     | 0.10  | 0.20  | Average |
| CT_original_glcm_Autocorrelation                    | 0.931    | 0.930 | 0.933 | 0.931   |
| CT_original_glcm_JointAverage                       | 0.935    | 0.935 | 0.937 | 0.936   |
| CT_original_glcm_Correlation                        | 0.885    | 0.893 | 0.902 | 0.893   |
| CT_original_glcm_DifferenceAverage                  | 0.868    | 0.869 | 0.875 | 0.871   |
| CT_original_glcm_DifferenceEntropy                  | 0.936    | 0.934 | 0.934 | 0.935   |
| CT_original_glcm_DifferenceVariance                 | 0.802    | 0.803 | 0.807 | 0.804   |
| CT_original_glcm_JointEnergy                        | 0.957    | 0.948 | 0.941 | 0.948   |
| CT_original_glcm_JointEntropy                       | 0.945    | 0.938 | 0.933 | 0.939   |
| CT_original_glcm_Imc2                               | 0.914    | 0.927 | 0.930 | 0.924   |
| CT_original_glcm_Idm                                | 0.935    | 0.924 | 0.919 | 0.926   |
| CT_original_glcm_Id                                 | 0.934    | 0.925 | 0.921 | 0.926   |
| CT_original_glcm_MaximumProbability                 | 0.952    | 0.934 | 0.935 | 0.940   |
| CT_original_glcm_SumEntropy                         | 0.948    | 0.943 | 0.938 | 0.943   |
| CT_original_glrmlm_GrayLevelNonUniformity           | 0.928    | 0.951 | 0.943 | 0.940   |
| CT_original_glrmlm_GrayLevelNonUniformityNormalized | 0.964    | 0.962 | 0.961 | 0.962   |
| CT_original_glrmlm_GrayLevelVariance                | 0.838    | 0.858 | 0.871 | 0.856   |
| CT_original_glrmlm_HighGrayLevelRunEmphasis         | 0.936    | 0.939 | 0.943 | 0.939   |
| CT_original_glrmlm_LongRunEmphasis                  | 0.922    | 0.899 | 0.837 | 0.886   |
| CT_original_glrmlm_LowGrayLevelRunEmphasis          | 0.908    | 0.909 | 0.906 | 0.908   |
| CT_original_glrmlm_RunEntropy                       | 0.958    | 0.960 | 0.961 | 0.960   |
| CT_original_glrmlm_RunLengthNonUniformity           | 0.930    | 0.921 | 0.914 | 0.922   |
| CT_original_glrmlm_RunLengthNonUniformityNormalized | 0.939    | 0.940 | 0.934 | 0.938   |
| CT_original_glrmlm_ShortRunEmphasis                 | 0.949    | 0.951 | 0.948 | 0.950   |

| Feature name  | Binwidth |       |       |         |
|---|----------|-------|-------|---------|
|   | 0.05     | 0.10  | 0.20  | Average |
| CT_original_glrml_ShortRunHighGrayLevelEmphasis       | 0.939    | 0.941 | 0.945 | 0.942   |
| CT_original_glrml_ShortRunLowGrayLevelEmphasis        | 0.906    | 0.912 | 0.910 | 0.909   |
| CT_original_glszm_GrayLevelNonUniformity              | 0.923    | 0.912 | 0.904 | 0.913   |
| CT_original_glszm_GrayLevelNonUniformityNormalized    | 0.946    | 0.945 | 0.950 | 0.947   |
| CT_original_glszm_GrayLevelVariance                   | 0.929    | 0.947 | 0.957 | 0.944   |
| CT_original_glszm_HighGrayLevelZoneEmphasis           | 0.954    | 0.956 | 0.958 | 0.956   |
| CT_original_glszm_LowGrayLevelZoneEmphasis            | 0.950    | 0.942 | 0.944 | 0.945   |
| CT_original_glszm_SizeZoneNonUniformity               | 0.900    | 0.881 | 0.858 | 0.879   |
| CT_original_glszm_SmallAreaEmphasis                   | 0.943    | 0.896 | 0.849 | 0.896   |
| CT_original_glszm_SmallAreaHighGrayLevelEmphasis      | 0.954    | 0.953 | 0.952 | 0.953   |
| CT_original_glszm_SmallAreaLowGrayLevelEmphasis       | 0.946    | 0.932 | 0.907 | 0.928   |
| CT_original_glszm_ZoneEntropy                         | 0.968    | 0.969 | 0.971 | 0.969   |
| CT_original_glszm_ZonePercentage                      | 0.913    | 0.880 | 0.838 | 0.877   |
| CT_original_gldm_DependenceEntropy                    | 0.961    | 0.954 | 0.943 | 0.952   |
| CT_original_gldm_DependenceNonUniformity              | 0.921    | 0.805 | 0.813 | 0.846   |
| CT_original_gldm_DependenceVariance                   | 0.942    | 0.958 | 0.953 | 0.951   |
| CT_original_gldm_GrayLevelNonUniformity               | 0.881    | 0.881 | 0.912 | 0.891   |
| CT_original_gldm_HighGrayLevelEmphasis                | 0.932    | 0.932 | 0.935 | 0.933   |
| CT_original_gldm_LargeDependenceHighGrayLevelEmphasis | 0.878    | 0.904 | 0.912 | 0.898   |
| CT_original_gldm_LargeDependenceLowGrayLevelEmphasis  | 0.859    | 0.861 | 0.832 | 0.851   |
| CT_original_gldm_LowGrayLevelEmphasis                 | 0.896    | 0.896 | 0.896 | 0.896   |
| CT_original_gldm_SmallDependenceEmphasis              | 0.916    | 0.889 | 0.874 | 0.893   |
| CT_original_gldm_SmallDependenceHighGrayLevelEmphasis | 0.896    | 0.884 | 0.884 | 0.888   |
| CT_original_gldm_SmallDependenceLowGrayLevelEmphasis  | 0.889    | 0.893 | 0.864 | 0.882   |

| Feature name                 | Binwidth |       |       |         |
|------------------------------|----------|-------|-------|---------|
|                              | 0.05     | 0.10  | 0.20  | Average |
| CT_original_ngtdm_Coarseness | 0.909    | 0.928 | 0.922 | 0.920   |
| CT_original_ngtdm_Complexity | 0.857    | 0.867 | 0.875 | 0.866   |

**Table 7** The stable features in wavelet class in terms of ICC

| Feature name  | Binwidth |       |       |         |
|---|----------|-------|-------|---------|
|   | 0.05     | 0.10  | 0.20  | Average |
| CT_log-sigma-1-0-mm-3D_firstorder_10Percentile                | 0.876    | 0.876 | 0.876 | 0.876   |
| CT_log-sigma-1-0-mm-3D_firstorder_90Percentile                | 0.918    | 0.918 | 0.918 | 0.918   |
| CT_log-sigma-1-0-mm-3D_firstorder_Energy                      | 0.943    | 0.943 | 0.943 | 0.943   |
| CT_log-sigma-1-0-mm-3D_firstorder_Entropy                     | 0.955    | 0.952 | 0.937 | 0.948   |
| CT_log-sigma-1-0-mm-3D_firstorder_Kurtosis                    | 0.902    | 0.902 | 0.902 | 0.902   |
| CT_log-sigma-1-0-mm-3D_firstorder_Maximum                     | 0.941    | 0.941 | 0.941 | 0.941   |
| CT_log-sigma-1-0-mm-3D_firstorder_MeanAbsoluteDeviation       | 0.916    | 0.916 | 0.916 | 0.916   |
| CT_log-sigma-1-0-mm-3D_firstorder_Minimum                     | 0.929    | 0.929 | 0.929 | 0.929   |
| CT_log-sigma-1-0-mm-3D_firstorder_Range                       | 0.947    | 0.947 | 0.947 | 0.947   |
| CT_log-sigma-1-0-mm-3D_firstorder_RobustMeanAbsoluteDeviation | 0.826    | 0.826 | 0.826 | 0.826   |
| CT_log-sigma-1-0-mm-3D_firstorder_Skewness                    | 0.816    | 0.816 | 0.816 | 0.816   |
| CT_log-sigma-1-0-mm-3D_firstorder_TotalEnergy                 | 0.942    | 0.942 | 0.942 | 0.942   |
| CT_log-sigma-1-0-mm-3D_firstorder_Uniformity                  | 0.955    | 0.954 | 0.935 | 0.948   |
| CT_log-sigma-1-0-mm-3D_firstorder_Variance                    | 0.876    | 0.876 | 0.876 | 0.876   |
| CT_log-sigma-1-0-mm-3D_glcmm_Autocorrelation                  | 0.894    | 0.898 | 0.911 | 0.901   |
| CT_log-sigma-1-0-mm-3D_glcmm_JointAverage                     | 0.927    | 0.928 | 0.932 | 0.929   |
| CT_log-sigma-1-0-mm-3D_glcmm_ClusterShade                     | 0.808    | 0.805 | 0.821 | 0.811   |

| Feature name  | Binwidth |       |       |         |
|---|----------|-------|-------|---------|
|   | 0.05     | 0.10  | 0.20  | Average |
| CT_log-sigma-1-0-mm-3D_glcm_ClusterTendency                   | 0.867    | 0.865 | 0.860 | 0.864   |
| CT_log-sigma-1-0-mm-3D_glcm_DifferenceEntropy                 | 0.940    | 0.927 | 0.892 | 0.920   |
| CT_log-sigma-1-0-mm-3D_glcm_DifferenceVariance                | 0.843    | 0.836 | 0.812 | 0.831   |
| CT_log-sigma-1-0-mm-3D_glcm_JointEnergy                       | 0.951    | 0.951 | 0.926 | 0.943   |
| CT_log-sigma-1-0-mm-3D_glcm_JointEntropy                      | 0.948    | 0.942 | 0.921 | 0.937   |
| CT_log-sigma-1-0-mm-3D_glcm_Imc2                              | 0.900    | 0.926 | 0.933 | 0.920   |
| CT_log-sigma-1-0-mm-3D_glcm_MaximumProbability                | 0.925    | 0.918 | 0.846 | 0.896   |
| CT_log-sigma-1-0-mm-3D_glcm_SumEntropy                        | 0.955    | 0.952 | 0.937 | 0.948   |
| CT_log-sigma-1-0-mm-3D_glcm_SumSquares                        | 0.855    | 0.853 | 0.844 | 0.850   |
| CT_log-sigma-1-0-mm-3D_glrlm_GrayLevelNonUniformity           | 0.933    | 0.941 | 0.945 | 0.940   |
| CT_log-sigma-1-0-mm-3D_glrlm_GrayLevelNonUniformityNormalized | 0.959    | 0.962 | 0.952 | 0.958   |
| CT_log-sigma-1-0-mm-3D_glrlm_GrayLevelVariance                | 0.908    | 0.910 | 0.903 | 0.907   |
| CT_log-sigma-1-0-mm-3D_glrlm_HighGrayLevelRunEmphasis         | 0.894    | 0.897 | 0.910 | 0.900   |
| CT_log-sigma-1-0-mm-3D_glrlm_LongRunHighGrayLevelEmphasis     | 0.876    | 0.894 | 0.929 | 0.900   |
| CT_log-sigma-1-0-mm-3D_glrlm_LongRunLowGrayLevelEmphasis      | 0.907    | 0.925 | 0.918 | 0.917   |
| CT_log-sigma-1-0-mm-3D_glrlm_LowGrayLevelRunEmphasis          | 0.933    | 0.934 | 0.925 | 0.931   |
| CT_log-sigma-1-0-mm-3D_glrlm_RunEntropy                       | 0.967    | 0.970 | 0.968 | 0.968   |
| CT_log-sigma-1-0-mm-3D_glrlm_RunLengthNonUniformity           | 0.930    | 0.925 | 0.922 | 0.926   |
| CT_log-sigma-1-0-mm-3D_glrlm_ShortRunHighGrayLevelEmphasis    | 0.885    | 0.883 | 0.888 | 0.885   |
| CT_log-sigma-1-0-mm-3D_glrlm_ShortRunLowGrayLevelEmphasis     | 0.919    | 0.923 | 0.925 | 0.922   |
| CT_log-sigma-1-0-mm-3D_glszm_GrayLevelNonUniformity           | 0.912    | 0.897 | 0.919 | 0.910   |
| CT_log-sigma-1-0-mm-3D_glszm_GrayLevelNonUniformityNormalized | 0.953    | 0.952 | 0.958 | 0.954   |
| CT_log-sigma-1-0-mm-3D_glszm_GrayLevelVariance                | 0.941    | 0.946 | 0.949 | 0.945   |
| CT_log-sigma-1-0-mm-3D_glszm_HighGrayLevelZoneEmphasis        | 0.896    | 0.901 | 0.913 | 0.903   |



| Feature name   | Binwidth |       |       |         |
|--|----------|-------|-------|---------|
|  | 0.05     | 0.10  | 0.20  | Average |
| CT_log-sigma-1-0-mm-3D_glszm_LowGrayLevelZoneEmphasis            | 0.956    | 0.944 | 0.905 | 0.935   |
| CT_log-sigma-1-0-mm-3D_glszm_SizeZoneNonUniformity               | 0.869    | 0.848 | 0.856 | 0.858   |
| CT_log-sigma-1-0-mm-3D_glszm_SmallAreaHighGrayLevelEmphasis      | 0.892    | 0.899 | 0.884 | 0.892   |
| CT_log-sigma-1-0-mm-3D_glszm_SmallAreaLowGrayLevelEmphasis       | 0.954    | 0.912 | 0.813 | 0.893   |
| CT_log-sigma-1-0-mm-3D_glszm_ZoneEntropy                         | 0.965    | 0.968 | 0.969 | 0.968   |
| CT_log-sigma-1-0-mm-3D_glszm_ZonePercentage                      | 0.875    | 0.849 | 0.811 | 0.845   |
| CT_log-sigma-1-0-mm-3D_gldm_DependenceEntropy                    | 0.966    | 0.963 | 0.948 | 0.959   |
| CT_log-sigma-1-0-mm-3D_gldm_DependenceNonUniformity              | 0.924    | 0.938 | 0.943 | 0.935   |
| CT_log-sigma-1-0-mm-3D_gldm_DependenceVariance                   | 0.945    | 0.955 | 0.944 | 0.948   |
| CT_log-sigma-1-0-mm-3D_gldm_GrayLevelNonUniformity               | 0.913    | 0.932 | 0.940 | 0.928   |
| CT_log-sigma-1-0-mm-3D_gldm_GrayLevelVariance                    | 0.875    | 0.874 | 0.866 | 0.872   |
| CT_log-sigma-1-0-mm-3D_gldm_HighGrayLevelEmphasis                | 0.894    | 0.898 | 0.910 | 0.901   |
| CT_log-sigma-1-0-mm-3D_gldm_LargeDependenceHighGrayLevelEmphasis | 0.914    | 0.921 | 0.933 | 0.922   |
| CT_log-sigma-1-0-mm-3D_gldm_LargeDependenceLowGrayLevelEmphasis  | 0.909    | 0.914 | 0.903 | 0.909   |
| CT_log-sigma-1-0-mm-3D_gldm_LowGrayLevelEmphasis                 | 0.931    | 0.937 | 0.930 | 0.933   |
| CT_log-sigma-1-0-mm-3D_gldm_SmallDependenceLowGrayLevelEmphasis  | 0.828    | 0.845 | 0.905 | 0.859   |
| CT_log-sigma-1-0-mm-3D_ngtdm_Coarseness                          | 0.883    | 0.885 | 0.888 | 0.885   |
| CT_log-sigma-1-0-mm-3D_ngtdm_Complexity                          | 0.823    | 0.839 | 0.874 | 0.845   |
| CT_log-sigma-2-0-mm-3D_firstorder_10Percentile                   | 0.804    | 0.804 | 0.804 | 0.804   |
| CT_log-sigma-2-0-mm-3D_firstorder_90Percentile                   | 0.933    | 0.933 | 0.933 | 0.933   |
| CT_log-sigma-2-0-mm-3D_firstorder_Energy                         | 0.943    | 0.943 | 0.943 | 0.943   |
| CT_log-sigma-2-0-mm-3D_firstorder_Entropy                        | 0.954    | 0.950 | 0.942 | 0.949   |
| CT_log-sigma-2-0-mm-3D_firstorder_InterquartileRange             | 0.821    | 0.821 | 0.821 | 0.821   |
| CT_log-sigma-2-0-mm-3D_firstorder_Maximum                        | 0.926    | 0.926 | 0.926 | 0.926   |

| Feature name  | Binwidth |       |       |         |
|---|----------|-------|-------|---------|
|   | 0.05     | 0.10  | 0.20  | Average |
| CT_log-sigma-2-0-mm-3D_firstorder_MeanAbsoluteDeviation       | 0.912    | 0.912 | 0.912 | 0.912   |
| CT_log-sigma-2-0-mm-3D_firstorder_Minimum                     | 0.929    | 0.929 | 0.929 | 0.929   |
| CT_log-sigma-2-0-mm-3D_firstorder_Range                       | 0.942    | 0.942 | 0.942 | 0.942   |
| CT_log-sigma-2-0-mm-3D_firstorder_RobustMeanAbsoluteDeviation | 0.879    | 0.879 | 0.879 | 0.879   |
| CT_log-sigma-2-0-mm-3D_firstorder_TotalEnergy                 | 0.942    | 0.942 | 0.942 | 0.942   |
| CT_log-sigma-2-0-mm-3D_firstorder_Uniformity                  | 0.947    | 0.951 | 0.947 | 0.948   |
| CT_log-sigma-2-0-mm-3D_firstorder_Variance                    | 0.861    | 0.861 | 0.861 | 0.861   |
| CT_log-sigma-2-0-mm-3D_glcmm_Autocorrelation                  | 0.918    | 0.917 | 0.922 | 0.919   |
| CT_log-sigma-2-0-mm-3D_glcmm_JointAverage                     | 0.935    | 0.933 | 0.934 | 0.934   |
| CT_log-sigma-2-0-mm-3D_glcmm_ClusterTendency                  | 0.838    | 0.839 | 0.836 | 0.838   |
| CT_log-sigma-2-0-mm-3D_glcmm_DifferenceAverage                | 0.861    | 0.854 | 0.835 | 0.850   |
| CT_log-sigma-2-0-mm-3D_glcmm_DifferenceEntropy                | 0.940    | 0.935 | 0.921 | 0.932   |
| CT_log-sigma-2-0-mm-3D_glcmm_DifferenceVariance               | 0.818    | 0.817 | 0.808 | 0.814   |
| CT_log-sigma-2-0-mm-3D_glcmm_JointEnergy                      | 0.936    | 0.947 | 0.943 | 0.942   |
| CT_log-sigma-2-0-mm-3D_glcmm_JointEntropy                     | 0.952    | 0.946 | 0.934 | 0.944   |
| CT_log-sigma-2-0-mm-3D_glcmm_Idm                              | 0.888    | 0.870 | 0.840 | 0.866   |
| CT_log-sigma-2-0-mm-3D_glcmm_Id                               | 0.891    | 0.876 | 0.845 | 0.871   |
| CT_log-sigma-2-0-mm-3D_glcmm_MaximumProbability               | 0.935    | 0.938 | 0.911 | 0.928   |
| CT_log-sigma-2-0-mm-3D_glcmm_SumEntropy                       | 0.953    | 0.950 | 0.941 | 0.948   |
| CT_log-sigma-2-0-mm-3D_glcmm_SumSquares                       | 0.833    | 0.834 | 0.831 | 0.833   |
| CT_log-sigma-2-0-mm-3D_glrmm_GrayLevelNonUniformity           | 0.943    | 0.946 | 0.948 | 0.946   |
| CT_log-sigma-2-0-mm-3D_glrmm_GrayLevelNonUniformityNormalized | 0.951    | 0.956 | 0.956 | 0.954   |
| CT_log-sigma-2-0-mm-3D_glrmm_GrayLevelVariance                | 0.884    | 0.888 | 0.891 | 0.888   |
| CT_log-sigma-2-0-mm-3D_glrmm_HighGrayLevelRunEmphasis         | 0.917    | 0.915 | 0.919 | 0.917   |

| Feature name   | Binwidth |       |       |         |
|--|----------|-------|-------|---------|
|  | 0.05     | 0.10  | 0.20  | Average |
| CT_log-sigma-2-0-mm-3D_glrmlm_LongRunHighGrayLevelEmphasis       | 0.878    | 0.878 | 0.923 | 0.893   |
| CT_log-sigma-2-0-mm-3D_glrmlm_LongRunLowGrayLevelEmphasis        | 0.870    | 0.856 | 0.849 | 0.858   |
| CT_log-sigma-2-0-mm-3D_glrmlm_LowGrayLevelRunEmphasis            | 0.909    | 0.918 | 0.904 | 0.910   |
| CT_log-sigma-2-0-mm-3D_glrmlm_RunEntropy                         | 0.961    | 0.961 | 0.963 | 0.962   |
| CT_log-sigma-2-0-mm-3D_glrmlm_RunLengthNonUniformity             | 0.938    | 0.933 | 0.923 | 0.931   |
| CT_log-sigma-2-0-mm-3D_glrmlm_ShortRunHighGrayLevelEmphasis      | 0.914    | 0.907 | 0.903 | 0.908   |
| CT_log-sigma-2-0-mm-3D_glrmlm_ShortRunLowGrayLevelEmphasis       | 0.894    | 0.901 | 0.891 | 0.895   |
| CT_log-sigma-2-0-mm-3D_glszm_GrayLevelNonUniformity              | 0.924    | 0.906 | 0.927 | 0.919   |
| CT_log-sigma-2-0-mm-3D_glszm_GrayLevelNonUniformityNormalized    | 0.941    | 0.954 | 0.961 | 0.952   |
| CT_log-sigma-2-0-mm-3D_glszm_GrayLevelVariance                   | 0.891    | 0.922 | 0.930 | 0.914   |
| CT_log-sigma-2-0-mm-3D_glszm_HighGrayLevelZoneEmphasis           | 0.911    | 0.913 | 0.921 | 0.915   |
| CT_log-sigma-2-0-mm-3D_glszm_LowGrayLevelZoneEmphasis            | 0.942    | 0.916 | 0.914 | 0.924   |
| CT_log-sigma-2-0-mm-3D_glszm_SizeZoneNonUniformity               | 0.877    | 0.842 | 0.903 | 0.874   |
| CT_log-sigma-2-0-mm-3D_glszm_SmallAreaHighGrayLevelEmphasis      | 0.912    | 0.923 | 0.908 | 0.914   |
| CT_log-sigma-2-0-mm-3D_glszm_ZoneEntropy                         | 0.959    | 0.968 | 0.969 | 0.965   |
| CT_log-sigma-2-0-mm-3D_gldm_DependenceEntropy                    | 0.969    | 0.965 | 0.951 | 0.961   |
| CT_log-sigma-2-0-mm-3D_gldm_DependenceNonUniformity              | 0.932    | 0.937 | 0.933 | 0.934   |
| CT_log-sigma-2-0-mm-3D_gldm_DependenceNonUniformityNormalized    | 0.803    | 0.932 | 0.922 | 0.886   |
| CT_log-sigma-2-0-mm-3D_gldm_DependenceVariance                   | 0.897    | 0.939 | 0.942 | 0.926   |
| CT_log-sigma-2-0-mm-3D_gldm_GrayLevelNonUniformity               | 0.899    | 0.923 | 0.933 | 0.918   |
| CT_log-sigma-2-0-mm-3D_gldm_GrayLevelVariance                    | 0.861    | 0.861 | 0.858 | 0.860   |
| CT_log-sigma-2-0-mm-3D_gldm_HighGrayLevelEmphasis                | 0.917    | 0.916 | 0.921 | 0.918   |
| CT_log-sigma-2-0-mm-3D_gldm_LargeDependenceHighGrayLevelEmphasis | 0.928    | 0.932 | 0.938 | 0.932   |
| CT_log-sigma-2-0-mm-3D_gldm_LargeDependenceLowGrayLevelEmphasis  | 0.879    | 0.886 | 0.877 | 0.881   |

| Feature name   | Binwidth |       |       |         |
|--|----------|-------|-------|---------|
|  | 0.05     | 0.10  | 0.20  | Average |
| CT_log-sigma-2-0-mm-3D_gldm_LowGrayLevelEmphasis                 | 0.898    | 0.913 | 0.906 | 0.906   |
| CT_log-sigma-2-0-mm-3D_gldm_SmallDependenceHighGrayLevelEmphasis | 0.841    | 0.830 | 0.847 | 0.839   |
| CT_log-sigma-2-0-mm-3D_ngtdm_Coarseness                          | 0.907    | 0.910 | 0.909 | 0.908   |
| CT_log-sigma-2-0-mm-3D_ngtdm_Complexity                          | 0.844    | 0.849 | 0.865 | 0.853   |
| CT_log-sigma-3-0-mm-3D_firstorder_10Percentile                   | 0.806    | 0.806 | 0.806 | 0.806   |
| CT_log-sigma-3-0-mm-3D_firstorder_90Percentile                   | 0.900    | 0.900 | 0.900 | 0.900   |
| CT_log-sigma-3-0-mm-3D_firstorder_Energy                         | 0.943    | 0.943 | 0.943 | 0.943   |
| CT_log-sigma-3-0-mm-3D_firstorder_Entropy                        | 0.950    | 0.947 | 0.938 | 0.945   |
| CT_log-sigma-3-0-mm-3D_firstorder_InterquartileRange             | 0.909    | 0.909 | 0.909 | 0.909   |
| CT_log-sigma-3-0-mm-3D_firstorder_Maximum                        | 0.913    | 0.913 | 0.913 | 0.913   |
| CT_log-sigma-3-0-mm-3D_firstorder_MeanAbsoluteDeviation          | 0.915    | 0.915 | 0.915 | 0.915   |
| CT_log-sigma-3-0-mm-3D_firstorder_Minimum                        | 0.941    | 0.941 | 0.941 | 0.941   |
| CT_log-sigma-3-0-mm-3D_firstorder_Range                          | 0.947    | 0.947 | 0.947 | 0.947   |
| CT_log-sigma-3-0-mm-3D_firstorder_RobustMeanAbsoluteDeviation    | 0.913    | 0.913 | 0.913 | 0.913   |
| CT_log-sigma-3-0-mm-3D_firstorder_TotalEnergy                    | 0.942    | 0.942 | 0.942 | 0.942   |
| CT_log-sigma-3-0-mm-3D_firstorder_Uniformity                     | 0.944    | 0.952 | 0.947 | 0.947   |
| CT_log-sigma-3-0-mm-3D_firstorder_Variance                       | 0.864    | 0.864 | 0.864 | 0.864   |
| CT_log-sigma-3-0-mm-3D_gldm_Autocorrelation                      | 0.930    | 0.927 | 0.927 | 0.928   |
| CT_log-sigma-3-0-mm-3D_gldm_JointAverage                         | 0.946    | 0.942 | 0.940 | 0.943   |
| CT_log-sigma-3-0-mm-3D_gldm_ClusterTendency                      | 0.819    | 0.819 | 0.817 | 0.818   |
| CT_log-sigma-3-0-mm-3D_gldm_Contrast                             | 0.842    | 0.842 | 0.843 | 0.842   |
| CT_log-sigma-3-0-mm-3D_gldm_DifferenceAverage                    | 0.889    | 0.887 | 0.879 | 0.885   |
| CT_log-sigma-3-0-mm-3D_gldm_DifferenceEntropy                    | 0.942    | 0.940 | 0.934 | 0.939   |
| CT_log-sigma-3-0-mm-3D_gldm_DifferenceVariance                   | 0.866    | 0.867 | 0.871 | 0.868   |

| Feature name  | Binwidth |       |       |         |
|---|----------|-------|-------|---------|
|   | 0.05     | 0.10  | 0.20  | Average |
| CT_log-sigma-3-0-mm-3D_glcm_JointEnergy                       | 0.923    | 0.939 | 0.940 | 0.934   |
| CT_log-sigma-3-0-mm-3D_glcm_JointEntropy                      | 0.952    | 0.946 | 0.934 | 0.944   |
| CT_log-sigma-3-0-mm-3D_glcm_Idm                               | 0.838    | 0.851 | 0.868 | 0.853   |
| CT_log-sigma-3-0-mm-3D_glcm_Idmn                              | 0.866    | 0.869 | 0.903 | 0.879   |
| CT_log-sigma-3-0-mm-3D_glcm_Id                                | 0.859    | 0.854 | 0.852 | 0.855   |
| CT_log-sigma-3-0-mm-3D_glcm_Idn                               | 0.893    | 0.881 | 0.879 | 0.884   |
| CT_log-sigma-3-0-mm-3D_glcm_MaximumProbability                | 0.923    | 0.919 | 0.919 | 0.920   |
| CT_log-sigma-3-0-mm-3D_glcm_SumEntropy                        | 0.944    | 0.941 | 0.930 | 0.939   |
| CT_log-sigma-3-0-mm-3D_glcm_SumSquares                        | 0.827    | 0.827 | 0.825 | 0.826   |
| CT_log-sigma-3-0-mm-3D_glrlm_GrayLevelNonUniformity           | 0.947    | 0.949 | 0.950 | 0.949   |
| CT_log-sigma-3-0-mm-3D_glrlm_GrayLevelNonUniformityNormalized | 0.953    | 0.958 | 0.957 | 0.956   |
| CT_log-sigma-3-0-mm-3D_glrlm_GrayLevelVariance                | 0.875    | 0.882 | 0.890 | 0.882   |
| CT_log-sigma-3-0-mm-3D_glrlm_HighGrayLevelRunEmphasis         | 0.928    | 0.924 | 0.923 | 0.925   |
| CT_log-sigma-3-0-mm-3D_glrlm_LongRunHighGrayLevelEmphasis     | 0.897    | 0.883 | 0.890 | 0.890   |
| CT_log-sigma-3-0-mm-3D_glrlm_LongRunLowGrayLevelEmphasis      | 0.942    | 0.932 | 0.922 | 0.932   |
| CT_log-sigma-3-0-mm-3D_glrlm_LowGrayLevelRunEmphasis          | 0.945    | 0.931 | 0.932 | 0.936   |
| CT_log-sigma-3-0-mm-3D_glrlm_RunEntropy                       | 0.945    | 0.947 | 0.954 | 0.949   |
| CT_log-sigma-3-0-mm-3D_glrlm_RunLengthNonUniformity           | 0.943    | 0.938 | 0.927 | 0.936   |
| CT_log-sigma-3-0-mm-3D_glrlm_ShortRunHighGrayLevelEmphasis    | 0.927    | 0.921 | 0.915 | 0.921   |
| CT_log-sigma-3-0-mm-3D_glrlm_ShortRunLowGrayLevelEmphasis     | 0.940    | 0.918 | 0.912 | 0.923   |
| CT_log-sigma-3-0-mm-3D_glszm_GrayLevelNonUniformity           | 0.933    | 0.904 | 0.950 | 0.929   |
| CT_log-sigma-3-0-mm-3D_glszm_GrayLevelNonUniformityNormalized | 0.949    | 0.955 | 0.943 | 0.949   |
| CT_log-sigma-3-0-mm-3D_glszm_GrayLevelVariance                | 0.916    | 0.931 | 0.935 | 0.927   |
| CT_log-sigma-3-0-mm-3D_glszm_HighGrayLevelZoneEmphasis        | 0.920    | 0.926 | 0.931 | 0.926   |

| Feature name   | Binwidth |       |       |         |
|--|----------|-------|-------|---------|
|  | 0.05     | 0.10  | 0.20  | Average |
| CT_log-sigma-3-0-mm-3D_glszm_LowGrayLevelZoneEmphasis            | 0.960    | 0.935 | 0.918 | 0.938   |
| CT_log-sigma-3-0-mm-3D_glszm_SizeZoneNonUniformity               | 0.877    | 0.861 | 0.942 | 0.893   |
| CT_log-sigma-3-0-mm-3D_glszm_SmallAreaHighGrayLevelEmphasis      | 0.924    | 0.933 | 0.925 | 0.928   |
| CT_log-sigma-3-0-mm-3D_glszm_ZoneEntropy                         | 0.958    | 0.957 | 0.960 | 0.958   |
| CT_log-sigma-3-0-mm-3D_gldm_DependenceEntropy                    | 0.964    | 0.961 | 0.944 | 0.956   |
| CT_log-sigma-3-0-mm-3D_gldm_DependenceNonUniformity              | 0.940    | 0.934 | 0.920 | 0.931   |
| CT_log-sigma-3-0-mm-3D_gldm_DependenceNonUniformityNormalized    | 0.851    | 0.900 | 0.878 | 0.876   |
| CT_log-sigma-3-0-mm-3D_gldm_DependenceVariance                   | 0.815    | 0.925 | 0.946 | 0.895   |
| CT_log-sigma-3-0-mm-3D_gldm_GrayLevelNonUniformity               | 0.918    | 0.928 | 0.932 | 0.926   |
| CT_log-sigma-3-0-mm-3D_gldm_GrayLevelVariance                    | 0.864    | 0.864 | 0.861 | 0.863   |
| CT_log-sigma-3-0-mm-3D_gldm_HighGrayLevelEmphasis                | 0.928    | 0.925 | 0.925 | 0.926   |
| CT_log-sigma-3-0-mm-3D_gldm_LargeDependenceHighGrayLevelEmphasis | 0.916    | 0.923 | 0.929 | 0.922   |
| CT_log-sigma-3-0-mm-3D_gldm_LargeDependenceLowGrayLevelEmphasis  | 0.935    | 0.934 | 0.931 | 0.933   |
| CT_log-sigma-3-0-mm-3D_gldm_LowGrayLevelEmphasis                 | 0.939    | 0.923 | 0.934 | 0.932   |
| CT_log-sigma-3-0-mm-3D_gldm_SmallDependenceHighGrayLevelEmphasis | 0.882    | 0.878 | 0.891 | 0.884   |
| CT_log-sigma-3-0-mm-3D_gldm_SmallDependenceLowGrayLevelEmphasis  | 0.887    | 0.864 | 0.880 | 0.877   |
| CT_log-sigma-3-0-mm-3D_ngtdm_Coarseness                          | 0.940    | 0.935 | 0.931 | 0.935   |
| CT_log-sigma-3-0-mm-3D_ngtdm_Complexity                          | 0.864    | 0.874 | 0.882 | 0.873   |
| CT_log-sigma-4-0-mm-3D_firstorder_10Percentile                   | 0.842    | 0.842 | 0.842 | 0.842   |
| CT_log-sigma-4-0-mm-3D_firstorder_90Percentile                   | 0.819    | 0.819 | 0.819 | 0.819   |
| CT_log-sigma-4-0-mm-3D_firstorder_Energy                         | 0.943    | 0.943 | 0.943 | 0.943   |
| CT_log-sigma-4-0-mm-3D_firstorder_Entropy                        | 0.944    | 0.942 | 0.937 | 0.941   |
| CT_log-sigma-4-0-mm-3D_firstorder_InterquartileRange             | 0.900    | 0.900 | 0.900 | 0.900   |
| CT_log-sigma-4-0-mm-3D_firstorder_Kurtosis                       | 0.890    | 0.890 | 0.890 | 0.890   |

| Feature name  | Binwidth |       |       |         |
|---|----------|-------|-------|---------|
|   | 0.05     | 0.10  | 0.20  | Average |
| CT_log-sigma-4-0-mm-3D_firstorder_Maximum                     | 0.899    | 0.899 | 0.899 | 0.899   |
| CT_log-sigma-4-0-mm-3D_firstorder_MeanAbsoluteDeviation       | 0.917    | 0.917 | 0.917 | 0.917   |
| CT_log-sigma-4-0-mm-3D_firstorder_Minimum                     | 0.957    | 0.957 | 0.957 | 0.957   |
| CT_log-sigma-4-0-mm-3D_firstorder_Range                       | 0.956    | 0.956 | 0.956 | 0.956   |
| CT_log-sigma-4-0-mm-3D_firstorder_RobustMeanAbsoluteDeviation | 0.904    | 0.904 | 0.904 | 0.904   |
| CT_log-sigma-4-0-mm-3D_firstorder_TotalEnergy                 | 0.942    | 0.942 | 0.942 | 0.942   |
| CT_log-sigma-4-0-mm-3D_firstorder_Uniformity                  | 0.935    | 0.941 | 0.934 | 0.937   |
| CT_log-sigma-4-0-mm-3D_firstorder_Variance                    | 0.877    | 0.877 | 0.877 | 0.877   |
| CT_log-sigma-4-0-mm-3D_glcml_Autocorrelation                  | 0.945    | 0.946 | 0.944 | 0.945   |
| CT_log-sigma-4-0-mm-3D_glcml_JointAverage                     | 0.960    | 0.961 | 0.958 | 0.960   |
| CT_log-sigma-4-0-mm-3D_glcml_ClusterTendency                  | 0.838    | 0.838 | 0.834 | 0.836   |
| CT_log-sigma-4-0-mm-3D_glcml_DifferenceEntropy                | 0.937    | 0.935 | 0.934 | 0.935   |
| CT_log-sigma-4-0-mm-3D_glcml_DifferenceVariance               | 0.873    | 0.874 | 0.883 | 0.876   |
| CT_log-sigma-4-0-mm-3D_glcml_JointEnergy                      | 0.895    | 0.928 | 0.926 | 0.916   |
| CT_log-sigma-4-0-mm-3D_glcml_JointEntropy                     | 0.943    | 0.939 | 0.930 | 0.937   |
| CT_log-sigma-4-0-mm-3D_glcml_Idmn                             | 0.906    | 0.914 | 0.922 | 0.914   |
| CT_log-sigma-4-0-mm-3D_glcml_Idn                              | 0.937    | 0.931 | 0.909 | 0.926   |
| CT_log-sigma-4-0-mm-3D_glcml_MaximumProbability               | 0.827    | 0.889 | 0.842 | 0.853   |
| CT_log-sigma-4-0-mm-3D_glcml_SumEntropy                       | 0.935    | 0.935 | 0.930 | 0.934   |
| CT_log-sigma-4-0-mm-3D_glcml_SumSquares                       | 0.841    | 0.842 | 0.838 | 0.840   |
| CT_log-sigma-4-0-mm-3D_glrml_GrayLevelNonUniformity           | 0.946    | 0.949 | 0.950 | 0.948   |
| CT_log-sigma-4-0-mm-3D_glrml_GrayLevelNonUniformityNormalized | 0.948    | 0.950 | 0.955 | 0.951   |
| CT_log-sigma-4-0-mm-3D_glrml_GrayLevelVariance                | 0.886    | 0.893 | 0.903 | 0.894   |
| CT_log-sigma-4-0-mm-3D_glrml_HighGrayLevelRunEmphasis         | 0.944    | 0.945 | 0.942 | 0.944   |

| Feature name   | Binwidth |       |       |         |
|--|----------|-------|-------|---------|
|  | 0.05     | 0.10  | 0.20  | Average |
| CT_log-sigma-4-0-mm-3D_glrmlm_LongRunHighGrayLevelEmphasis       | 0.932    | 0.933 | 0.928 | 0.931   |
| CT_log-sigma-4-0-mm-3D_glrmlm_LongRunLowGrayLevelEmphasis        | 0.898    | 0.900 | 0.942 | 0.913   |
| CT_log-sigma-4-0-mm-3D_glrmlm_LowGrayLevelRunEmphasis            | 0.954    | 0.956 | 0.963 | 0.957   |
| CT_log-sigma-4-0-mm-3D_glrmlm_RunEntropy                         | 0.951    | 0.952 | 0.959 | 0.954   |
| CT_log-sigma-4-0-mm-3D_glrmlm_RunLengthNonUniformity             | 0.945    | 0.942 | 0.933 | 0.940   |
| CT_log-sigma-4-0-mm-3D_glrmlm_ShortRunHighGrayLevelEmphasis      | 0.942    | 0.940 | 0.932 | 0.938   |
| CT_log-sigma-4-0-mm-3D_glrmlm_ShortRunLowGrayLevelEmphasis       | 0.962    | 0.963 | 0.957 | 0.960   |
| CT_log-sigma-4-0-mm-3D_glszm_GrayLevelNonUniformity              | 0.908    | 0.874 | 0.905 | 0.896   |
| CT_log-sigma-4-0-mm-3D_glszm_GrayLevelNonUniformityNormalized    | 0.964    | 0.956 | 0.945 | 0.955   |
| CT_log-sigma-4-0-mm-3D_glszm_GrayLevelVariance                   | 0.941    | 0.950 | 0.930 | 0.941   |
| CT_log-sigma-4-0-mm-3D_glszm_HighGrayLevelZoneEmphasis           | 0.945    | 0.952 | 0.950 | 0.949   |
| CT_log-sigma-4-0-mm-3D_glszm_LowGrayLevelZoneEmphasis            | 0.954    | 0.934 | 0.952 | 0.947   |
| CT_log-sigma-4-0-mm-3D_glszm_SizeZoneNonUniformity               | 0.833    | 0.872 | 0.887 | 0.864   |
| CT_log-sigma-4-0-mm-3D_glszm_SmallAreaHighGrayLevelEmphasis      | 0.944    | 0.957 | 0.903 | 0.934   |
| CT_log-sigma-4-0-mm-3D_glszm_ZoneEntropy                         | 0.960    | 0.956 | 0.959 | 0.958   |
| CT_log-sigma-4-0-mm-3D_gldm_DependenceEntropy                    | 0.959    | 0.953 | 0.941 | 0.951   |
| CT_log-sigma-4-0-mm-3D_gldm_DependenceNonUniformity              | 0.945    | 0.938 | 0.909 | 0.931   |
| CT_log-sigma-4-0-mm-3D_gldm_DependenceNonUniformityNormalized    | 0.886    | 0.908 | 0.886 | 0.893   |
| CT_log-sigma-4-0-mm-3D_gldm_DependenceVariance                   | 0.859    | 0.922 | 0.937 | 0.906   |
| CT_log-sigma-4-0-mm-3D_gldm_GrayLevelNonUniformity               | 0.931    | 0.931 | 0.932 | 0.931   |
| CT_log-sigma-4-0-mm-3D_gldm_GrayLevelVariance                    | 0.877    | 0.877 | 0.876 | 0.877   |
| CT_log-sigma-4-0-mm-3D_gldm_HighGrayLevelEmphasis                | 0.944    | 0.946 | 0.943 | 0.944   |
| CT_log-sigma-4-0-mm-3D_gldm_LargeDependenceHighGrayLevelEmphasis | 0.938    | 0.946 | 0.950 | 0.945   |
| CT_log-sigma-4-0-mm-3D_gldm_LargeDependenceLowGrayLevelEmphasis  | 0.857    | 0.873 | 0.938 | 0.889   |



| Feature name   | Binwidth |       |       |         |
|--|----------|-------|-------|---------|
|  | 0.05     | 0.10  | 0.20  | Average |
| CT_log-sigma-4-0-mm-3D_gldm_LowGrayLevelEmphasis                 | 0.946    | 0.948 | 0.963 | 0.952   |
| CT_log-sigma-4-0-mm-3D_gldm_SmallDependenceHighGrayLevelEmphasis | 0.894    | 0.907 | 0.905 | 0.902   |
| CT_log-sigma-4-0-mm-3D_gldm_SmallDependenceLowGrayLevelEmphasis  | 0.936    | 0.915 | 0.940 | 0.930   |
| CT_log-sigma-4-0-mm-3D_ngtdm_Coarseness                          | 0.933    | 0.929 | 0.928 | 0.930   |
| CT_log-sigma-4-0-mm-3D_ngtdm_Complexity                          | 0.885    | 0.897 | 0.901 | 0.894   |
| CT_log-sigma-4-0-mm-3D_ngtdm_Contrast                            | 0.847    | 0.853 | 0.816 | 0.839   |
| CT_log-sigma-5-0-mm-3D_firstorder_10Percentile                   | 0.874    | 0.874 | 0.874 | 0.874   |
| CT_log-sigma-5-0-mm-3D_firstorder_Energy                         | 0.943    | 0.943 | 0.943 | 0.943   |
| CT_log-sigma-5-0-mm-3D_firstorder_Entropy                        | 0.955    | 0.953 | 0.951 | 0.953   |
| CT_log-sigma-5-0-mm-3D_firstorder_InterquartileRange             | 0.902    | 0.902 | 0.902 | 0.902   |
| CT_log-sigma-5-0-mm-3D_firstorder_Maximum                        | 0.891    | 0.891 | 0.891 | 0.891   |
| CT_log-sigma-5-0-mm-3D_firstorder_MeanAbsoluteDeviation          | 0.931    | 0.931 | 0.931 | 0.931   |
| CT_log-sigma-5-0-mm-3D_firstorder_Minimum                        | 0.958    | 0.958 | 0.958 | 0.958   |
| CT_log-sigma-5-0-mm-3D_firstorder_Range                          | 0.958    | 0.958 | 0.958 | 0.958   |
| CT_log-sigma-5-0-mm-3D_firstorder_RobustMeanAbsoluteDeviation    | 0.910    | 0.910 | 0.910 | 0.910   |
| CT_log-sigma-5-0-mm-3D_firstorder_TotalEnergy                    | 0.942    | 0.942 | 0.942 | 0.942   |
| CT_log-sigma-5-0-mm-3D_firstorder_Uniformity                     | 0.944    | 0.943 | 0.944 | 0.944   |
| CT_log-sigma-5-0-mm-3D_firstorder_Variance                       | 0.891    | 0.891 | 0.891 | 0.891   |
| CT_log-sigma-5-0-mm-3D_gldm_Autocorrelation                      | 0.940    | 0.944 | 0.940 | 0.941   |
| CT_log-sigma-5-0-mm-3D_gldm_JointAverage                         | 0.959    | 0.961 | 0.954 | 0.958   |
| CT_log-sigma-5-0-mm-3D_gldm_ClusterTendency                      | 0.869    | 0.869 | 0.869 | 0.869   |
| CT_log-sigma-5-0-mm-3D_gldm_DifferenceEntropy                    | 0.905    | 0.892 | 0.871 | 0.889   |
| CT_log-sigma-5-0-mm-3D_gldm_JointEnergy                          | 0.920    | 0.921 | 0.924 | 0.922   |
| CT_log-sigma-5-0-mm-3D_gldm_JointEntropy                         | 0.949    | 0.944 | 0.940 | 0.944   |

| Feature name  | Binwidth |       |       |         |
|---|----------|-------|-------|---------|
|   | 0.05     | 0.10  | 0.20  | Average |
| CT_log-sigma-5-0-mm-3D_glcm_Idmn                              | 0.881    | 0.893 | 0.891 | 0.888   |
| CT_log-sigma-5-0-mm-3D_glcm_Idn                               | 0.925    | 0.921 | 0.874 | 0.907   |
| CT_log-sigma-5-0-mm-3D_glcm_MaximumProbability                | 0.896    | 0.887 | 0.889 | 0.891   |
| CT_log-sigma-5-0-mm-3D_glcm_SumEntropy                        | 0.952    | 0.952 | 0.947 | 0.950   |
| CT_log-sigma-5-0-mm-3D_glcm_SumSquares                        | 0.869    | 0.868 | 0.869 | 0.869   |
| CT_log-sigma-5-0-mm-3D_glrlm_GrayLevelNonUniformity           | 0.945    | 0.948 | 0.948 | 0.947   |
| CT_log-sigma-5-0-mm-3D_glrlm_GrayLevelNonUniformityNormalized | 0.953    | 0.955 | 0.958 | 0.955   |
| CT_log-sigma-5-0-mm-3D_glrlm_GrayLevelVariance                | 0.899    | 0.905 | 0.915 | 0.906   |
| CT_log-sigma-5-0-mm-3D_glrlm_HighGrayLevelRunEmphasis         | 0.940    | 0.943 | 0.939 | 0.941   |
| CT_log-sigma-5-0-mm-3D_glrlm_LongRunHighGrayLevelEmphasis     | 0.935    | 0.937 | 0.927 | 0.933   |
| CT_log-sigma-5-0-mm-3D_glrlm_LongRunLowGrayLevelEmphasis      | 0.883    | 0.917 | 0.886 | 0.895   |
| CT_log-sigma-5-0-mm-3D_glrlm_LowGrayLevelRunEmphasis          | 0.933    | 0.957 | 0.941 | 0.944   |
| CT_log-sigma-5-0-mm-3D_glrlm_RunEntropy                       | 0.965    | 0.966 | 0.968 | 0.966   |
| CT_log-sigma-5-0-mm-3D_glrlm_RunLengthNonUniformity           | 0.946    | 0.943 | 0.933 | 0.941   |
| CT_log-sigma-5-0-mm-3D_glrlm_ShortRunHighGrayLevelEmphasis    | 0.936    | 0.937 | 0.927 | 0.933   |
| CT_log-sigma-5-0-mm-3D_glrlm_ShortRunLowGrayLevelEmphasis     | 0.934    | 0.957 | 0.944 | 0.945   |
| CT_log-sigma-5-0-mm-3D_glszm_GrayLevelNonUniformity           | 0.867    | 0.886 | 0.872 | 0.875   |
| CT_log-sigma-5-0-mm-3D_glszm_GrayLevelNonUniformityNormalized | 0.966    | 0.957 | 0.939 | 0.954   |
| CT_log-sigma-5-0-mm-3D_glszm_GrayLevelVariance                | 0.947    | 0.945 | 0.935 | 0.942   |
| CT_log-sigma-5-0-mm-3D_glszm_HighGrayLevelZoneEmphasis        | 0.952    | 0.955 | 0.951 | 0.953   |
| CT_log-sigma-5-0-mm-3D_glszm_LargeAreaHighGrayLevelEmphasis   | 0.813    | 0.823 | 0.821 | 0.819   |
| CT_log-sigma-5-0-mm-3D_glszm_LowGrayLevelZoneEmphasis         | 0.942    | 0.933 | 0.897 | 0.924   |
| CT_log-sigma-5-0-mm-3D_glszm_SizeZoneNonUniformity            | 0.819    | 0.921 | 0.888 | 0.876   |
| CT_log-sigma-5-0-mm-3D_glszm_SmallAreaHighGrayLevelEmphasis   | 0.950    | 0.959 | 0.921 | 0.943   |

| Feature name   | Binwidth |       |       |         |
|--|----------|-------|-------|---------|
|  | 0.05     | 0.10  | 0.20  | Average |
| CT_log-sigma-5-0-mm-3D_glszm_ZoneEntropy                         | 0.964    | 0.957 | 0.954 | 0.959   |
| CT_log-sigma-5-0-mm-3D_glszm_ZoneVariance                        | 0.805    | 0.861 | 0.847 | 0.838   |
| CT_log-sigma-5-0-mm-3D_gldm_DependenceEntropy                    | 0.965    | 0.960 | 0.938 | 0.955   |
| CT_log-sigma-5-0-mm-3D_gldm_DependenceNonUniformity              | 0.947    | 0.941 | 0.919 | 0.935   |
| CT_log-sigma-5-0-mm-3D_gldm_DependenceVariance                   | 0.871    | 0.913 | 0.911 | 0.898   |
| CT_log-sigma-5-0-mm-3D_gldm_GrayLevelNonUniformity               | 0.936    | 0.936 | 0.935 | 0.936   |
| CT_log-sigma-5-0-mm-3D_gldm_GrayLevelVariance                    | 0.891    | 0.890 | 0.890 | 0.891   |
| CT_log-sigma-5-0-mm-3D_gldm_HighGrayLevelEmphasis                | 0.940    | 0.943 | 0.940 | 0.941   |
| CT_log-sigma-5-0-mm-3D_gldm_LargeDependenceHighGrayLevelEmphasis | 0.939    | 0.946 | 0.946 | 0.944   |
| CT_log-sigma-5-0-mm-3D_gldm_LargeDependenceLowGrayLevelEmphasis  | 0.876    | 0.917 | 0.908 | 0.900   |
| CT_log-sigma-5-0-mm-3D_gldm_LowGrayLevelEmphasis                 | 0.925    | 0.956 | 0.946 | 0.942   |
| CT_log-sigma-5-0-mm-3D_gldm_SmallDependenceHighGrayLevelEmphasis | 0.852    | 0.869 | 0.875 | 0.865   |
| CT_log-sigma-5-0-mm-3D_gldm_SmallDependenceLowGrayLevelEmphasis  | 0.947    | 0.955 | 0.944 | 0.949   |
| CT_log-sigma-5-0-mm-3D_ngtdm_Coarseness                          | 0.912    | 0.909 | 0.919 | 0.913   |
| CT_log-sigma-5-0-mm-3D_ngtdm_Complexity                          | 0.886    | 0.894 | 0.893 | 0.891   |
| CT_wavelet-LLH_firstorder_10Percentile                           | 0.911    | 0.911 | 0.911 | 0.911   |
| CT_wavelet-LLH_firstorder_Energy                                 | 0.943    | 0.943 | 0.943 | 0.943   |
| CT_wavelet-LLH_firstorder_Entropy                                | 0.949    | 0.949 | 0.947 | 0.948   |
| CT_wavelet-LLH_firstorder_Maximum                                | 0.902    | 0.902 | 0.902 | 0.902   |
| CT_wavelet-LLH_firstorder_MeanAbsoluteDeviation                  | 0.927    | 0.927 | 0.927 | 0.927   |
| CT_wavelet-LLH_firstorder_Mean                                   | 0.852    | 0.852 | 0.852 | 0.852   |
| CT_wavelet-LLH_firstorder_Minimum                                | 0.952    | 0.952 | 0.952 | 0.952   |
| CT_wavelet-LLH_firstorder_Range                                  | 0.963    | 0.963 | 0.963 | 0.963   |
| CT_wavelet-LLH_firstorder_RootMeanSquared                        | 0.852    | 0.852 | 0.852 | 0.852   |

| Feature name  | Binwidth |       |       |         |
|---|----------|-------|-------|---------|
|   | 0.05     | 0.10  | 0.20  | Average |
| CT_wavelet-LLH_firstorder_TotalEnergy                 | 0.942    | 0.942 | 0.942 | 0.942   |
| CT_wavelet-LLH_firstorder_Uniformity                  | 0.922    | 0.928 | 0.931 | 0.927   |
| CT_wavelet-LLH_firstorder_Variance                    | 0.910    | 0.910 | 0.910 | 0.910   |
| CT_wavelet-LLH_glcm_Autocorrelation                   | 0.939    | 0.940 | 0.942 | 0.940   |
| CT_wavelet-LLH_glcm_JointAverage                      | 0.952    | 0.953 | 0.954 | 0.953   |
| CT_wavelet-LLH_glcm_ClusterProminence                 | 0.849    | 0.849 | 0.849 | 0.849   |
| CT_wavelet-LLH_glcm_ClusterTendency                   | 0.912    | 0.912 | 0.911 | 0.912   |
| CT_wavelet-LLH_glcm_Contrast                          | 0.899    | 0.899 | 0.898 | 0.899   |
| CT_wavelet-LLH_glcm_DifferenceAverage                 | 0.926    | 0.925 | 0.921 | 0.924   |
| CT_wavelet-LLH_glcm_DifferenceEntropy                 | 0.950    | 0.952 | 0.953 | 0.952   |
| CT_wavelet-LLH_glcm_DifferenceVariance                | 0.904    | 0.904 | 0.903 | 0.903   |
| CT_wavelet-LLH_glcm_JointEnergy                       | 0.894    | 0.914 | 0.920 | 0.909   |
| CT_wavelet-LLH_glcm_JointEntropy                      | 0.952    | 0.950 | 0.947 | 0.950   |
| CT_wavelet-LLH_glcm_Idm                               | 0.892    | 0.898 | 0.900 | 0.897   |
| CT_wavelet-LLH_glcm_Id                                | 0.899    | 0.904 | 0.905 | 0.903   |
| CT_wavelet-LLH_glcm_InverseVariance                   | 0.887    | 0.885 | 0.876 | 0.883   |
| CT_wavelet-LLH_glcm_MaximumProbability                | 0.903    | 0.916 | 0.908 | 0.909   |
| CT_wavelet-LLH_glcm_SumEntropy                        | 0.947    | 0.948 | 0.949 | 0.948   |
| CT_wavelet-LLH_glcm_SumSquares                        | 0.911    | 0.911 | 0.911 | 0.911   |
| CT_wavelet-LLH_glrIm_GrayLevelNonUniformity           | 0.901    | 0.919 | 0.931 | 0.917   |
| CT_wavelet-LLH_glrIm_GrayLevelNonUniformityNormalized | 0.931    | 0.938 | 0.945 | 0.938   |
| CT_wavelet-LLH_glrIm_GrayLevelVariance                | 0.913    | 0.913 | 0.915 | 0.914   |
| CT_wavelet-LLH_glrIm_HighGrayLevelRunEmphasis         | 0.939    | 0.940 | 0.942 | 0.941   |
| CT_wavelet-LLH_glrIm_LongRunEmphasis                  | 0.844    | 0.872 | 0.868 | 0.861   |

| Feature name  | Binwidth |       |       |         |
|---|----------|-------|-------|---------|
|   | 0.05     | 0.10  | 0.20  | Average |
| CT_wavelet-LLH_grlm_LongRunHighGrayLevelEmphasis      | 0.923    | 0.919 | 0.929 | 0.924   |
| CT_wavelet-LLH_grlm_LongRunLowGrayLevelEmphasis       | 0.919    | 0.905 | 0.891 | 0.905   |
| CT_wavelet-LLH_grlm_LowGrayLevelRunEmphasis           | 0.938    | 0.931 | 0.920 | 0.930   |
| CT_wavelet-LLH_grlm_RunEntropy                        | 0.961    | 0.964 | 0.966 | 0.963   |
| CT_wavelet-LLH_grlm_RunLengthNonUniformity            | 0.941    | 0.939 | 0.939 | 0.940   |
| CT_wavelet-LLH_grlm_ShortRunEmphasis                  | 0.883    | 0.889 | 0.891 | 0.887   |
| CT_wavelet-LLH_grlm_ShortRunHighGrayLevelEmphasis     | 0.939    | 0.940 | 0.941 | 0.940   |
| CT_wavelet-LLH_grlm_ShortRunLowGrayLevelEmphasis      | 0.939    | 0.932 | 0.923 | 0.931   |
| CT_wavelet-LLH_glszm_GrayLevelNonUniformity           | 0.931    | 0.924 | 0.916 | 0.923   |
| CT_wavelet-LLH_glszm_GrayLevelNonUniformityNormalized | 0.961    | 0.958 | 0.961 | 0.960   |
| CT_wavelet-LLH_glszm_GrayLevelVariance                | 0.901    | 0.902 | 0.919 | 0.907   |
| CT_wavelet-LLH_glszm_HighGrayLevelZoneEmphasis        | 0.939    | 0.940 | 0.943 | 0.940   |
| CT_wavelet-LLH_glszm_LowGrayLevelZoneEmphasis         | 0.941    | 0.948 | 0.946 | 0.945   |
| CT_wavelet-LLH_glszm_SizeZoneNonUniformity            | 0.920    | 0.904 | 0.884 | 0.902   |
| CT_wavelet-LLH_glszm_SizeZoneNonUniformityNormalized  | 0.948    | 0.937 | 0.939 | 0.941   |
| CT_wavelet-LLH_glszm_SmallAreaEmphasis                | 0.952    | 0.943 | 0.948 | 0.948   |
| CT_wavelet-LLH_glszm_SmallAreaHighGrayLevelEmphasis   | 0.937    | 0.936 | 0.936 | 0.936   |
| CT_wavelet-LLH_glszm_SmallAreaLowGrayLevelEmphasis    | 0.931    | 0.941 | 0.913 | 0.928   |
| CT_wavelet-LLH_glszm_ZoneEntropy                      | 0.968    | 0.973 | 0.973 | 0.971   |
| CT_wavelet-LLH_glszm_ZonePercentage                   | 0.910    | 0.903 | 0.888 | 0.900   |
| CT_wavelet-LLH_gldm_DependenceEntropy                 | 0.966    | 0.964 | 0.960 | 0.963   |
| CT_wavelet-LLH_gldm_DependenceNonUniformity           | 0.921    | 0.929 | 0.939 | 0.929   |
| CT_wavelet-LLH_gldm_DependenceVariance                | 0.855    | 0.935 | 0.954 | 0.915   |
| CT_wavelet-LLH_gldm_GrayLevelNonUniformity            | 0.857    | 0.896 | 0.921 | 0.892   |

| Feature name   | Binwidth |       |       |         |
|--|----------|-------|-------|---------|
|  | 0.05     | 0.10  | 0.20  | Average |
| CT_wavelet-LLH_gldm_GrayLevelVariance                    | 0.910    | 0.910 | 0.910 | 0.910   |
| CT_wavelet-LLH_gldm_HighGrayLevelEmphasis                | 0.939    | 0.940 | 0.942 | 0.941   |
| CT_wavelet-LLH_gldm_LargeDependenceHighGrayLevelEmphasis | 0.921    | 0.931 | 0.942 | 0.931   |
| CT_wavelet-LLH_gldm_LargeDependenceLowGrayLevelEmphasis  | 0.886    | 0.884 | 0.885 | 0.885   |
| CT_wavelet-LLH_gldm_LowGrayLevelEmphasis                 | 0.935    | 0.925 | 0.914 | 0.925   |
| CT_wavelet-LLH_gldm_SmallDependenceEmphasis              | 0.917    | 0.904 | 0.892 | 0.904   |
| CT_wavelet-LLH_gldm_SmallDependenceHighGrayLevelEmphasis | 0.923    | 0.907 | 0.892 | 0.907   |
| CT_wavelet-LLH_gldm_SmallDependenceLowGrayLevelEmphasis  | 0.888    | 0.892 | 0.900 | 0.893   |
| CT_wavelet-LLH_ngtdm_Coarseness                          | 0.915    | 0.913 | 0.913 | 0.914   |
| CT_wavelet-LLH_ngtdm_Complexity                          | 0.891    | 0.887 | 0.884 | 0.887   |
| CT_wavelet-LHL_firstorder_90Percentile                   | 0.917    | 0.917 | 0.917 | 0.917   |
| CT_wavelet-LHL_firstorder_Energy                         | 0.943    | 0.943 | 0.943 | 0.943   |
| CT_wavelet-LHL_firstorder_Entropy                        | 0.934    | 0.908 | 0.873 | 0.905   |
| CT_wavelet-LHL_firstorder_InterquartileRange             | 0.831    | 0.831 | 0.831 | 0.831   |
| CT_wavelet-LHL_firstorder_Maximum                        | 0.935    | 0.935 | 0.935 | 0.935   |
| CT_wavelet-LHL_firstorder_MeanAbsoluteDeviation          | 0.908    | 0.908 | 0.908 | 0.908   |
| CT_wavelet-LHL_firstorder_Minimum                        | 0.906    | 0.906 | 0.906 | 0.906   |
| CT_wavelet-LHL_firstorder_Range                          | 0.935    | 0.935 | 0.935 | 0.935   |
| CT_wavelet-LHL_firstorder_RobustMeanAbsoluteDeviation    | 0.845    | 0.845 | 0.845 | 0.845   |
| CT_wavelet-LHL_firstorder_TotalEnergy                    | 0.942    | 0.942 | 0.942 | 0.942   |
| CT_wavelet-LHL_firstorder_Uniformity                     | 0.931    | 0.893 | 0.862 | 0.895   |
| CT_wavelet-LHL_firstorder_Variance                       | 0.873    | 0.873 | 0.873 | 0.873   |
| CT_wavelet-LHL_glcm_Autocorrelation                      | 0.865    | 0.867 | 0.847 | 0.860   |
| CT_wavelet-LHL_glcm_JointAverage                         | 0.915    | 0.912 | 0.883 | 0.903   |

| Feature name  | Binwidth |       |       |         |
|---|----------|-------|-------|---------|
|   | 0.05     | 0.10  | 0.20  | Average |
| CT_wavelet-LHL_glcm_ClusterTendency                   | 0.841    | 0.831 | 0.840 | 0.837   |
| CT_wavelet-LHL_glcm_Correlation                       | 0.922    | 0.915 | 0.916 | 0.918   |
| CT_wavelet-LHL_glcm_JointEntropy                      | 0.919    | 0.886 | 0.824 | 0.876   |
| CT_wavelet-LHL_glcm_Imc1                              | 0.916    | 0.913 | 0.920 | 0.916   |
| CT_wavelet-LHL_glcm_Imc2                              | 0.934    | 0.918 | 0.916 | 0.923   |
| CT_wavelet-LHL_glcm_Idmn                              | 0.895    | 0.882 | 0.921 | 0.900   |
| CT_wavelet-LHL_glcm_Idn                               | 0.918    | 0.933 | 0.934 | 0.928   |
| CT_wavelet-LHL_glcm_SumEntropy                        | 0.926    | 0.899 | 0.860 | 0.895   |
| CT_wavelet-LHL_grlm_GrayLevelNonUniformity            | 0.944    | 0.946 | 0.947 | 0.946   |
| CT_wavelet-LHL_grlm_GrayLevelNonUniformityNormalized  | 0.948    | 0.917 | 0.873 | 0.913   |
| CT_wavelet-LHL_grlm_GrayLevelVariance                 | 0.897    | 0.882 | 0.849 | 0.876   |
| CT_wavelet-LHL_grlm_HighGrayLevelRunEmphasis          | 0.865    | 0.867 | 0.845 | 0.859   |
| CT_wavelet-LHL_grlm_LongRunHighGrayLevelEmphasis      | 0.861    | 0.885 | 0.878 | 0.875   |
| CT_wavelet-LHL_grlm_LowGrayLevelRunEmphasis           | 0.850    | 0.816 | 0.849 | 0.838   |
| CT_wavelet-LHL_grlm_RunEntropy                        | 0.961    | 0.955 | 0.952 | 0.956   |
| CT_wavelet-LHL_grlm_RunLengthNonUniformity            | 0.933    | 0.941 | 0.947 | 0.940   |
| CT_wavelet-LHL_grlm_RunVariance                       | 0.816    | 0.963 | 0.965 | 0.914   |
| CT_wavelet-LHL_grlm_ShortRunHighGrayLevelEmphasis     | 0.856    | 0.852 | 0.818 | 0.842   |
| CT_wavelet-LHL_grlm_ShortRunLowGrayLevelEmphasis      | 0.870    | 0.839 | 0.875 | 0.861   |
| CT_wavelet-LHL_glszm_GrayLevelNonUniformity           | 0.937    | 0.927 | 0.890 | 0.918   |
| CT_wavelet-LHL_glszm_GrayLevelNonUniformityNormalized | 0.908    | 0.883 | 0.921 | 0.904   |
| CT_wavelet-LHL_glszm_GrayLevelVariance                | 0.928    | 0.932 | 0.940 | 0.934   |
| CT_wavelet-LHL_glszm_HighGrayLevelZoneEmphasis        | 0.865    | 0.863 | 0.833 | 0.854   |
| CT_wavelet-LHL_glszm_SizeZoneNonUniformity            | 0.888    | 0.892 | 0.890 | 0.890   |

| Feature name   | Binwidth |       |       |         |
|--|----------|-------|-------|---------|
|  | 0.05     | 0.10  | 0.20  | Average |
| CT_wavelet-LHL_glszm_SmallAreaHighGrayLevelEmphasis      | 0.848    | 0.841 | 0.819 | 0.836   |
| CT_wavelet-LHL_glszm_ZoneEntropy                         | 0.962    | 0.958 | 0.943 | 0.954   |
| CT_wavelet-LHL_gldm_DependenceEntropy                    | 0.945    | 0.919 | 0.873 | 0.912   |
| CT_wavelet-LHL_gldm_DependenceNonUniformity              | 0.939    | 0.938 | 0.938 | 0.938   |
| CT_wavelet-LHL_gldm_DependenceVariance                   | 0.954    | 0.921 | 0.837 | 0.904   |
| CT_wavelet-LHL_gldm_GrayLevelNonUniformity               | 0.940    | 0.943 | 0.943 | 0.942   |
| CT_wavelet-LHL_gldm_GrayLevelVariance                    | 0.868    | 0.856 | 0.833 | 0.852   |
| CT_wavelet-LHL_gldm_HighGrayLevelEmphasis                | 0.865    | 0.867 | 0.847 | 0.859   |
| CT_wavelet-LHL_gldm_LargeDependenceHighGrayLevelEmphasis | 0.870    | 0.883 | 0.874 | 0.876   |
| CT_wavelet-LHL_gldm_LowGrayLevelEmphasis                 | 0.847    | 0.815 | 0.851 | 0.838   |
| CT_wavelet-LHL_gldm_SmallDependenceLowGrayLevelEmphasis  | 0.863    | 0.881 | 0.882 | 0.875   |
| CT_wavelet-LHL_ngtdm_Coarseness                          | 0.892    | 0.898 | 0.901 | 0.897   |
| CT_wavelet-LHL_ngtdm_Complexity                          | 0.876    | 0.891 | 0.880 | 0.882   |
| CT_wavelet-LHH_firstorder_10Percentile                   | 0.888    | 0.888 | 0.888 | 0.888   |
| CT_wavelet-LHH_firstorder_90Percentile                   | 0.899    | 0.899 | 0.899 | 0.899   |
| CT_wavelet-LHH_firstorder_Energy                         | 0.943    | 0.943 | 0.943 | 0.943   |
| CT_wavelet-LHH_firstorder_Maximum                        | 0.901    | 0.901 | 0.901 | 0.901   |
| CT_wavelet-LHH_firstorder_MeanAbsoluteDeviation          | 0.905    | 0.905 | 0.905 | 0.905   |
| CT_wavelet-LHH_firstorder_Minimum                        | 0.930    | 0.930 | 0.930 | 0.930   |
| CT_wavelet-LHH_firstorder_Range                          | 0.926    | 0.926 | 0.926 | 0.926   |
| CT_wavelet-LHH_firstorder_RobustMeanAbsoluteDeviation    | 0.844    | 0.844 | 0.844 | 0.844   |
| CT_wavelet-LHH_firstorder_TotalEnergy                    | 0.942    | 0.942 | 0.942 | 0.942   |
| CT_wavelet-LHH_firstorder_Variance                       | 0.824    | 0.824 | 0.824 | 0.824   |
| CT_wavelet-LHH_glcm_Autocorrelation                      | 0.871    | 0.880 | 0.875 | 0.875   |



| Feature name  | Binwidth |       |       |         |
|---|----------|-------|-------|---------|
|   | 0.05     | 0.10  | 0.20  | Average |
| CT_wavelet-LHH_glcm_JointAverage                      | 0.926    | 0.926 | 0.884 | 0.912   |
| CT_wavelet-LHH_glcm_Imc1                              | 0.924    | 0.878 | 0.811 | 0.871   |
| CT_wavelet-LHH_glcm_Idmn                              | 0.915    | 0.932 | 0.892 | 0.913   |
| CT_wavelet-LHH_glcm_Idn                               | 0.929    | 0.941 | 0.901 | 0.924   |
| CT_wavelet-LHH_grlm_GrayLevelNonUniformity            | 0.942    | 0.944 | 0.944 | 0.943   |
| CT_wavelet-LHH_grlm_HighGrayLevelRunEmphasis          | 0.872    | 0.879 | 0.875 | 0.875   |
| CT_wavelet-LHH_grlm_LongRunHighGrayLevelEmphasis      | 0.925    | 0.924 | 0.907 | 0.918   |
| CT_wavelet-LHH_grlm_LowGrayLevelRunEmphasis           | 0.949    | 0.933 | 0.856 | 0.912   |
| CT_wavelet-LHH_grlm_RunEntropy                        | 0.960    | 0.948 | 0.949 | 0.952   |
| CT_wavelet-LHH_grlm_RunLengthNonUniformity            | 0.936    | 0.941 | 0.943 | 0.940   |
| CT_wavelet-LHH_grlm_RunVariance                       | 0.822    | 0.936 | 0.949 | 0.902   |
| CT_wavelet-LHH_grlm_ShortRunHighGrayLevelEmphasis     | 0.844    | 0.852 | 0.850 | 0.849   |
| CT_wavelet-LHH_grlm_ShortRunLowGrayLevelEmphasis      | 0.947    | 0.932 | 0.865 | 0.915   |
| CT_wavelet-LHH_glszm_GrayLevelNonUniformity           | 0.926    | 0.869 | 0.817 | 0.871   |
| CT_wavelet-LHH_glszm_GrayLevelNonUniformityNormalized | 0.902    | 0.947 | 0.895 | 0.915   |
| CT_wavelet-LHH_glszm_GrayLevelVariance                | 0.931    | 0.948 | 0.902 | 0.927   |
| CT_wavelet-LHH_glszm_HighGrayLevelZoneEmphasis        | 0.884    | 0.897 | 0.880 | 0.887   |
| CT_wavelet-LHH_glszm_LargeAreaHighGrayLevelEmphasis   | 0.902    | 0.908 | 0.848 | 0.886   |
| CT_wavelet-LHH_glszm_SizeZoneNonUniformity            | 0.820    | 0.839 | 0.868 | 0.842   |
| CT_wavelet-LHH_glszm_SmallAreaHighGrayLevelEmphasis   | 0.845    | 0.883 | 0.860 | 0.863   |
| CT_wavelet-LHH_glszm_ZoneEntropy                      | 0.968    | 0.962 | 0.895 | 0.942   |
| CT_wavelet-LHH_gldm_DependenceNonUniformity           | 0.937    | 0.935 | 0.935 | 0.935   |
| CT_wavelet-LHH_gldm_GrayLevelNonUniformity            | 0.939    | 0.942 | 0.942 | 0.941   |
| CT_wavelet-LHH_gldm_HighGrayLevelEmphasis             | 0.871    | 0.880 | 0.875 | 0.875   |

| Feature name   | Binwidth |       |       |         |
|--|----------|-------|-------|---------|
|  | 0.05     | 0.10  | 0.20  | Average |
| CT_wavelet-LHH_gldm_LargeDependenceHighGrayLevelEmphasis | 0.924    | 0.921 | 0.913 | 0.919   |
| CT_wavelet-LHH_gldm_LowGrayLevelEmphasis                 | 0.949    | 0.933 | 0.859 | 0.914   |
| CT_wavelet-LHH_gldm_SmallDependenceLowGrayLevelEmphasis  | 0.926    | 0.927 | 0.871 | 0.908   |
| CT_wavelet-LHH_ngtdm_Coarseness                          | 0.885    | 0.892 | 0.894 | 0.891   |
| CT_wavelet-LHH_ngtdm_Complexity                          | 0.806    | 0.843 | 0.863 | 0.837   |
| CT_wavelet-LHH_ngtdm_Contrast                            | 0.859    | 0.912 | 0.877 | 0.882   |
| CT_wavelet-HLL_firstorder_10Percentile                   | 0.909    | 0.909 | 0.909 | 0.909   |
| CT_wavelet-HLL_firstorder_90Percentile                   | 0.910    | 0.910 | 0.910 | 0.910   |
| CT_wavelet-HLL_firstorder_Energy                         | 0.943    | 0.943 | 0.943 | 0.943   |
| CT_wavelet-HLL_firstorder_Entropy                        | 0.950    | 0.935 | 0.891 | 0.925   |
| CT_wavelet-HLL_firstorder_InterquartileRange             | 0.874    | 0.874 | 0.874 | 0.874   |
| CT_wavelet-HLL_firstorder_Maximum                        | 0.938    | 0.938 | 0.938 | 0.938   |
| CT_wavelet-HLL_firstorder_MeanAbsoluteDeviation          | 0.934    | 0.934 | 0.934 | 0.934   |
| CT_wavelet-HLL_firstorder_Minimum                        | 0.938    | 0.938 | 0.938 | 0.938   |
| CT_wavelet-HLL_firstorder_Range                          | 0.947    | 0.947 | 0.947 | 0.947   |
| CT_wavelet-HLL_firstorder_RobustMeanAbsoluteDeviation    | 0.892    | 0.892 | 0.892 | 0.892   |
| CT_wavelet-HLL_firstorder_TotalEnergy                    | 0.942    | 0.942 | 0.942 | 0.942   |
| CT_wavelet-HLL_firstorder_Uniformity                     | 0.948    | 0.924 | 0.865 | 0.913   |
| CT_wavelet-HLL_firstorder_Variance                       | 0.878    | 0.878 | 0.878 | 0.878   |
| CT_wavelet-HLL_glcm_Autocorrelation                      | 0.890    | 0.893 | 0.888 | 0.890   |
| CT_wavelet-HLL_glcm_JointAverage                         | 0.938    | 0.934 | 0.915 | 0.929   |
| CT_wavelet-HLL_glcm_ClusterTendency                      | 0.857    | 0.845 | 0.825 | 0.842   |
| CT_wavelet-HLL_glcm_Correlation                          | 0.958    | 0.947 | 0.931 | 0.945   |
| CT_wavelet-HLL_glcm_JointEntropy                         | 0.942    | 0.924 | 0.860 | 0.909   |

| Feature name  | Binwidth |       |       |         |
|---|----------|-------|-------|---------|
|   | 0.05     | 0.10  | 0.20  | Average |
| CT_wavelet-HLL_glcm_Imc1                              | 0.945    | 0.943 | 0.932 | 0.940   |
| CT_wavelet-HLL_glcm_Imc2                              | 0.959    | 0.951 | 0.933 | 0.948   |
| CT_wavelet-HLL_glcm_Idm                               | 0.918    | 0.828 | 0.809 | 0.852   |
| CT_wavelet-HLL_glcm_Idmn                              | 0.876    | 0.882 | 0.932 | 0.896   |
| CT_wavelet-HLL_glcm_Id                                | 0.918    | 0.817 | 0.844 | 0.860   |
| CT_wavelet-HLL_glcm_Idn                               | 0.917    | 0.936 | 0.946 | 0.933   |
| CT_wavelet-HLL_glcm_SumEntropy                        | 0.948    | 0.934 | 0.893 | 0.925   |
| CT_wavelet-HLL_glrlm_GrayLevelNonUniformity           | 0.946    | 0.948 | 0.947 | 0.947   |
| CT_wavelet-HLL_glrlm_GrayLevelNonUniformityNormalized | 0.960    | 0.940 | 0.886 | 0.929   |
| CT_wavelet-HLL_glrlm_GrayLevelVariance                | 0.901    | 0.878 | 0.820 | 0.866   |
| CT_wavelet-HLL_glrlm_HighGrayLevelRunEmphasis         | 0.890    | 0.893 | 0.887 | 0.890   |
| CT_wavelet-HLL_glrlm_LongRunHighGrayLevelEmphasis     | 0.928    | 0.929 | 0.918 | 0.925   |
| CT_wavelet-HLL_glrlm_LongRunLowGrayLevelEmphasis      | 0.881    | 0.840 | 0.876 | 0.865   |
| CT_wavelet-HLL_glrlm_LowGrayLevelRunEmphasis          | 0.897    | 0.862 | 0.909 | 0.889   |
| CT_wavelet-HLL_glrlm_RunEntropy                       | 0.966    | 0.960 | 0.954 | 0.960   |
| CT_wavelet-HLL_glrlm_RunLengthNonUniformity           | 0.930    | 0.936 | 0.944 | 0.937   |
| CT_wavelet-HLL_glrlm_RunVariance                      | 0.815    | 0.968 | 0.970 | 0.918   |
| CT_wavelet-HLL_glrlm_ShortRunHighGrayLevelEmphasis    | 0.865    | 0.868 | 0.863 | 0.865   |
| CT_wavelet-HLL_glrlm_ShortRunLowGrayLevelEmphasis     | 0.896    | 0.860 | 0.914 | 0.890   |
| CT_wavelet-HLL_glszm_GrayLevelNonUniformity           | 0.934    | 0.924 | 0.883 | 0.914   |
| CT_wavelet-HLL_glszm_GrayLevelNonUniformityNormalized | 0.951    | 0.932 | 0.957 | 0.947   |
| CT_wavelet-HLL_glszm_GrayLevelVariance                | 0.931    | 0.937 | 0.945 | 0.938   |
| CT_wavelet-HLL_glszm_HighGrayLevelZoneEmphasis        | 0.892    | 0.902 | 0.899 | 0.898   |
| CT_wavelet-HLL_glszm_LargeAreaHighGrayLevelEmphasis   | 0.822    | 0.851 | 0.851 | 0.841   |

| Feature name   | Binwidth |       |       |         |
|--|----------|-------|-------|---------|
|  | 0.05     | 0.10  | 0.20  | Average |
| CT_wavelet-HLL_glszm_LowGrayLevelZoneEmphasis            | 0.904    | 0.913 | 0.844 | 0.887   |
| CT_wavelet-HLL_glszm_SizeZoneNonUniformity               | 0.851    | 0.859 | 0.900 | 0.870   |
| CT_wavelet-HLL_glszm_SmallAreaHighGrayLevelEmphasis      | 0.861    | 0.867 | 0.884 | 0.871   |
| CT_wavelet-HLL_glszm_ZoneEntropy                         | 0.969    | 0.961 | 0.935 | 0.955   |
| CT_wavelet-HLL_gldm_DependenceEntropy                    | 0.954    | 0.936 | 0.877 | 0.923   |
| CT_wavelet-HLL_gldm_DependenceNonUniformity              | 0.939    | 0.940 | 0.939 | 0.939   |
| CT_wavelet-HLL_gldm_DependenceVariance                   | 0.962    | 0.924 | 0.834 | 0.907   |
| CT_wavelet-HLL_gldm_GrayLevelNonUniformity               | 0.942    | 0.944 | 0.944 | 0.943   |
| CT_wavelet-HLL_gldm_GrayLevelVariance                    | 0.873    | 0.857 | 0.804 | 0.845   |
| CT_wavelet-HLL_gldm_HighGrayLevelEmphasis                | 0.890    | 0.893 | 0.888 | 0.890   |
| CT_wavelet-HLL_gldm_LargeDependenceHighGrayLevelEmphasis | 0.928    | 0.922 | 0.910 | 0.920   |
| CT_wavelet-HLL_gldm_LargeDependenceLowGrayLevelEmphasis  | 0.885    | 0.845 | 0.878 | 0.870   |
| CT_wavelet-HLL_gldm_LowGrayLevelEmphasis                 | 0.897    | 0.862 | 0.910 | 0.890   |
| CT_wavelet-HLL_gldm_SmallDependenceLowGrayLevelEmphasis  | 0.881    | 0.857 | 0.910 | 0.882   |
| CT_wavelet-HLL_ngtdm_Coarseness                          | 0.894    | 0.902 | 0.904 | 0.900   |
| CT_wavelet-HLL_ngtdm_Complexity                          | 0.838    | 0.887 | 0.900 | 0.875   |
| CT_wavelet-HLH_firstorder_10Percentile                   | 0.897    | 0.897 | 0.897 | 0.897   |
| CT_wavelet-HLH_firstorder_90Percentile                   | 0.911    | 0.911 | 0.911 | 0.911   |
| CT_wavelet-HLH_firstorder_Energy                         | 0.943    | 0.943 | 0.943 | 0.943   |
| CT_wavelet-HLH_firstorder_InterquartileRange             | 0.815    | 0.815 | 0.815 | 0.815   |
| CT_wavelet-HLH_firstorder_Maximum                        | 0.945    | 0.945 | 0.945 | 0.945   |
| CT_wavelet-HLH_firstorder_MeanAbsoluteDeviation          | 0.920    | 0.920 | 0.920 | 0.920   |
| CT_wavelet-HLH_firstorder_Minimum                        | 0.894    | 0.894 | 0.894 | 0.894   |
| CT_wavelet-HLH_firstorder_Range                          | 0.939    | 0.939 | 0.939 | 0.939   |

| Feature name  | Binwidth |       |       |         |
|---|----------|-------|-------|---------|
|   | 0.05     | 0.10  | 0.20  | Average |
| CT_wavelet-HLH_firstorder_RobustMeanAbsoluteDeviation | 0.863    | 0.863 | 0.863 | 0.863   |
| CT_wavelet-HLH_firstorder_Skewness                    | 0.893    | 0.893 | 0.893 | 0.893   |
| CT_wavelet-HLH_firstorder_TotalEnergy                 | 0.942    | 0.942 | 0.942 | 0.942   |
| CT_wavelet-HLH_firstorder_Variance                    | 0.848    | 0.848 | 0.848 | 0.848   |
| CT_wavelet-HLH_glcm_Autocorrelation                   | 0.817    | 0.814 | 0.876 | 0.836   |
| CT_wavelet-HLH_glcm_JointAverage                      | 0.899    | 0.890 | 0.910 | 0.900   |
| CT_wavelet-HLH_glcm_Idmn                              | 0.951    | 0.942 | 0.949 | 0.947   |
| CT_wavelet-HLH_glcm_Idn                               | 0.956    | 0.960 | 0.952 | 0.956   |
| CT_wavelet-HLH_glrlm_GrayLevelNonUniformity           | 0.942    | 0.944 | 0.944 | 0.944   |
| CT_wavelet-HLH_glrlm_HighGrayLevelRunEmphasis         | 0.820    | 0.817 | 0.877 | 0.838   |
| CT_wavelet-HLH_glrlm_LongRunHighGrayLevelEmphasis     | 0.892    | 0.888 | 0.907 | 0.896   |
| CT_wavelet-HLH_glrlm_LongRunLowGrayLevelEmphasis      | 0.935    | 0.890 | 0.864 | 0.896   |
| CT_wavelet-HLH_glrlm_LowGrayLevelRunEmphasis          | 0.935    | 0.908 | 0.934 | 0.925   |
| CT_wavelet-HLH_glrlm_RunEntropy                       | 0.965    | 0.956 | 0.948 | 0.956   |
| CT_wavelet-HLH_glrlm_RunLengthNonUniformity           | 0.935    | 0.940 | 0.944 | 0.940   |
| CT_wavelet-HLH_glrlm_RunVariance                      | 0.830    | 0.958 | 0.963 | 0.917   |
| CT_wavelet-HLH_glrlm_ShortRunLowGrayLevelEmphasis     | 0.931    | 0.907 | 0.944 | 0.927   |
| CT_wavelet-HLH_glszm_GrayLevelNonUniformityNormalized | 0.928    | 0.935 | 0.953 | 0.939   |
| CT_wavelet-HLH_glszm_GrayLevelVariance                | 0.940    | 0.961 | 0.937 | 0.946   |
| CT_wavelet-HLH_glszm_HighGrayLevelZoneEmphasis        | 0.845    | 0.851 | 0.890 | 0.862   |
| CT_wavelet-HLH_glszm_LargeAreaHighGrayLevelEmphasis   | 0.851    | 0.881 | 0.877 | 0.870   |
| CT_wavelet-HLH_glszm_LowGrayLevelZoneEmphasis         | 0.935    | 0.826 | 0.898 | 0.887   |
| CT_wavelet-HLH_glszm_SizeZoneNonUniformity            | 0.812    | 0.841 | 0.863 | 0.838   |
| CT_wavelet-HLH_glszm_ZoneEntropy                      | 0.973    | 0.966 | 0.901 | 0.947   |

| Feature name   | Binwidth |       |       |         |
|--|----------|-------|-------|---------|
|  | 0.05     | 0.10  | 0.20  | Average |
| CT_wavelet-HLH_gldm_DependenceNonUniformity              | 0.937    | 0.936 | 0.936 | 0.936   |
| CT_wavelet-HLH_gldm_GrayLevelNonUniformity               | 0.939    | 0.942 | 0.943 | 0.941   |
| CT_wavelet-HLH_gldm_HighGrayLevelEmphasis                | 0.819    | 0.815 | 0.877 | 0.837   |
| CT_wavelet-HLH_gldm_LargeDependenceHighGrayLevelEmphasis | 0.891    | 0.880 | 0.911 | 0.894   |
| CT_wavelet-HLH_gldm_LargeDependenceLowGrayLevelEmphasis  | 0.928    | 0.879 | 0.865 | 0.891   |
| CT_wavelet-HLH_gldm_LowGrayLevelEmphasis                 | 0.935    | 0.907 | 0.933 | 0.925   |
| CT_wavelet-HLH_gldm_SmallDependenceLowGrayLevelEmphasis  | 0.873    | 0.888 | 0.947 | 0.903   |
| CT_wavelet-HLH_ngtdm_Coarseness                          | 0.882    | 0.890 | 0.893 | 0.888   |
| CT_wavelet-HLH_ngtdm_Complexity                          | 0.807    | 0.843 | 0.898 | 0.849   |
| CT_wavelet-HLH_ngtdm_Contrast                            | 0.928    | 0.902 | 0.939 | 0.923   |
| CT_wavelet-HHL_firstorder_10Percentile                   | 0.905    | 0.905 | 0.905 | 0.905   |
| CT_wavelet-HHL_firstorder_90Percentile                   | 0.906    | 0.906 | 0.906 | 0.906   |
| CT_wavelet-HHL_firstorder_Energy                         | 0.943    | 0.943 | 0.943 | 0.943   |
| CT_wavelet-HHL_firstorder_InterquartileRange             | 0.898    | 0.898 | 0.898 | 0.898   |
| CT_wavelet-HHL_firstorder_Maximum                        | 0.897    | 0.897 | 0.897 | 0.897   |
| CT_wavelet-HHL_firstorder_MeanAbsoluteDeviation          | 0.921    | 0.921 | 0.921 | 0.921   |
| CT_wavelet-HHL_firstorder_Minimum                        | 0.886    | 0.886 | 0.886 | 0.886   |
| CT_wavelet-HHL_firstorder_Range                          | 0.904    | 0.904 | 0.904 | 0.904   |
| CT_wavelet-HHL_firstorder_RobustMeanAbsoluteDeviation    | 0.901    | 0.901 | 0.901 | 0.901   |
| CT_wavelet-HHL_firstorder_TotalEnergy                    | 0.942    | 0.942 | 0.942 | 0.942   |
| CT_wavelet-HHL_firstorder_Variance                       | 0.865    | 0.865 | 0.865 | 0.865   |
| CT_wavelet-HHL_glcm_ClusterTendency                      | 0.898    | 0.930 | 0.931 | 0.920   |
| CT_wavelet-HHL_glcm_Contrast                             | 0.920    | 0.932 | 0.932 | 0.928   |
| CT_wavelet-HHL_glcm_Correlation                          | 0.931    | 0.932 | 0.932 | 0.932   |

| Feature name  | Binwidth |       |       |         |
|---|----------|-------|-------|---------|
|   | 0.05     | 0.10  | 0.20  | Average |
| CT_wavelet-HHL_glcm_DifferenceAverage                 | 0.929    | 0.932 | 0.932 | 0.931   |
| CT_wavelet-HHL_glcm_JointEnergy                       | 0.839    | 0.915 | 0.915 | 0.889   |
| CT_wavelet-HHL_glcm_Imc1                              | 0.916    | 0.919 | 0.919 | 0.918   |
| CT_wavelet-HHL_glcm_Imc2                              | 0.928    | 0.932 | 0.933 | 0.931   |
| CT_wavelet-HHL_glcm_Idm                               | 0.930    | 0.932 | 0.932 | 0.931   |
| CT_wavelet-HHL_glcm_Id                                | 0.930    | 0.932 | 0.932 | 0.932   |
| CT_wavelet-HHL_glcm_InverseVariance                   | 0.931    | 0.932 | 0.932 | 0.932   |
| CT_wavelet-HHL_glcm_SumEntropy                        | 0.807    | 0.918 | 0.928 | 0.884   |
| CT_wavelet-HHL_glrIm_GrayLevelNonUniformity           | 0.946    | 0.945 | 0.945 | 0.945   |
| CT_wavelet-HHL_glrIm_LongRunEmphasis                  | 0.965    | 0.964 | 0.964 | 0.964   |
| CT_wavelet-HHL_glrIm_LongRunHighGrayLevelEmphasis     | 0.827    | 0.813 | 0.962 | 0.868   |
| CT_wavelet-HHL_glrIm_RunEntropy                       | 0.951    | 0.952 | 0.952 | 0.951   |
| CT_wavelet-HHL_glrIm_RunLengthNonUniformity           | 0.947    | 0.948 | 0.948 | 0.948   |
| CT_wavelet-HHL_glrIm_RunLengthNonUniformityNormalized | 0.933    | 0.933 | 0.933 | 0.933   |
| CT_wavelet-HHL_glrIm_RunPercentage                    | 0.948    | 0.948 | 0.948 | 0.948   |
| CT_wavelet-HHL_glrIm_RunVariance                      | 0.965    | 0.965 | 0.965 | 0.965   |
| CT_wavelet-HHL_glrIm_ShortRunEmphasis                 | 0.943    | 0.943 | 0.943 | 0.943   |
| CT_wavelet-HHL_glrIm_ShortRunLowGrayLevelEmphasis     | 0.842    | 0.847 | 0.939 | 0.876   |
| CT_wavelet-HHL_glszm_GrayLevelNonUniformity           | 0.887    | 0.905 | 0.905 | 0.899   |
| CT_wavelet-HHL_glszm_LargeAreaEmphasis                | 0.849    | 0.844 | 0.846 | 0.846   |
| CT_wavelet-HHL_glszm_LargeAreaLowGrayLevelEmphasis    | 0.804    | 0.809 | 0.847 | 0.820   |
| CT_wavelet-HHL_glszm_SizeZoneNonUniformity            | 0.886    | 0.856 | 0.856 | 0.866   |
| CT_wavelet-HHL_glszm_ZoneVariance                     | 0.855    | 0.848 | 0.850 | 0.851   |
| CT_wavelet-HHL_gldm_DependenceNonUniformity           | 0.936    | 0.936 | 0.936 | 0.936   |

| Feature name   | Binwidth |       |       |         |
|--|----------|-------|-------|---------|
|  | 0.05     | 0.10  | 0.20  | Average |
| CT_wavelet-HHL_gldm_GrayLevelNonUniformity               | 0.943    | 0.943 | 0.943 | 0.943   |
| CT_wavelet-HHL_gldm_LargeDependenceEmphasis              | 0.955    | 0.954 | 0.954 | 0.955   |
| CT_wavelet-HHL_gldm_LargeDependenceHighGrayLevelEmphasis | 0.820    | 0.802 | 0.952 | 0.858   |
| CT_wavelet-HHL_gldm_SmallDependenceEmphasis              | 0.871    | 0.875 | 0.876 | 0.874   |
| CT_wavelet-HHL_gldm_SmallDependenceLowGrayLevelEmphasis  | 0.883    | 0.878 | 0.878 | 0.880   |
| CT_wavelet-HHL_ngtdm_Coarseness                          | 0.902    | 0.902 | 0.902 | 0.902   |
| CT_wavelet-HHH_firstorder_10Percentile                   | 0.891    | 0.891 | 0.891 | 0.891   |
| CT_wavelet-HHH_firstorder_90Percentile                   | 0.892    | 0.892 | 0.892 | 0.892   |
| CT_wavelet-HHH_firstorder_Energy                         | 0.943    | 0.943 | 0.943 | 0.943   |
| CT_wavelet-HHH_firstorder_InterquartileRange             | 0.842    | 0.842 | 0.842 | 0.842   |
| CT_wavelet-HHH_firstorder_Maximum                        | 0.911    | 0.911 | 0.911 | 0.911   |
| CT_wavelet-HHH_firstorder_MeanAbsoluteDeviation          | 0.906    | 0.906 | 0.906 | 0.906   |
| CT_wavelet-HHH_firstorder_Minimum                        | 0.928    | 0.928 | 0.928 | 0.928   |
| CT_wavelet-HHH_firstorder_Range                          | 0.927    | 0.927 | 0.927 | 0.927   |
| CT_wavelet-HHH_firstorder_RobustMeanAbsoluteDeviation    | 0.866    | 0.866 | 0.866 | 0.866   |
| CT_wavelet-HHH_firstorder_Skewness                       | 0.868    | 0.868 | 0.868 | 0.868   |
| CT_wavelet-HHH_firstorder_TotalEnergy                    | 0.942    | 0.942 | 0.942 | 0.942   |
| CT_wavelet-HHH_glrmlm_GrayLevelNonUniformity             | 0.944    | 0.944 | 0.944 | 0.944   |
| CT_wavelet-HHH_glrmlm_LongRunEmphasis                    | 0.968    | 0.968 | 0.968 | 0.968   |
| CT_wavelet-HHH_glrmlm_LongRunHighGrayLevelEmphasis       | 0.827    | 0.966 | 0.966 | 0.920   |
| CT_wavelet-HHH_glrmlm_RunEntropy                         | 0.949    | 0.950 | 0.950 | 0.950   |
| CT_wavelet-HHH_glrmlm_RunLengthNonUniformity             | 0.945    | 0.945 | 0.945 | 0.945   |
| CT_wavelet-HHH_glrmlm_RunLengthNonUniformityNormalized   | 0.924    | 0.924 | 0.924 | 0.924   |
| CT_wavelet-HHH_glrmlm_RunPercentage                      | 0.949    | 0.948 | 0.948 | 0.948   |



| Feature name   | Binwidth |       |       |         |
|--|----------|-------|-------|---------|
|  | 0.05     | 0.10  | 0.20  | Average |
| CT_wavelet-HHH_glrmlm_RunVariance                        | 0.970    | 0.970 | 0.970 | 0.970   |
| CT_wavelet-HHH_glrmlm_ShortRunEmphasis                   | 0.942    | 0.942 | 0.942 | 0.942   |
| CT_wavelet-HHH_glrmlm_ShortRunLowGrayLevelEmphasis       | 0.823    | 0.936 | 0.936 | 0.899   |
| CT_wavelet-HHH_glszm_LargeAreaEmphasis                   | 0.880    | 0.871 | 0.871 | 0.874   |
| CT_wavelet-HHH_glszm_LargeAreaLowGrayLevelEmphasis       | 0.856    | 0.871 | 0.871 | 0.866   |
| CT_wavelet-HHH_glszm_ZonePercentage                      | 0.807    | 0.809 | 0.809 | 0.808   |
| CT_wavelet-HHH_glszm_ZoneVariance                        | 0.876    | 0.867 | 0.867 | 0.870   |
| CT_wavelet-HHH_gldm_DependenceNonUniformity              | 0.932    | 0.932 | 0.932 | 0.932   |
| CT_wavelet-HHH_gldm_GrayLevelNonUniformity               | 0.943    | 0.942 | 0.942 | 0.943   |
| CT_wavelet-HHH_gldm_LargeDependenceEmphasis              | 0.955    | 0.955 | 0.955 | 0.955   |
| CT_wavelet-HHH_gldm_LargeDependenceHighGrayLevelEmphasis | 0.831    | 0.954 | 0.954 | 0.913   |
| CT_wavelet-HHH_gldm_SmallDependenceEmphasis              | 0.896    | 0.894 | 0.894 | 0.894   |
| CT_wavelet-HHH_gldm_SmallDependenceLowGrayLevelEmphasis  | 0.886    | 0.888 | 0.888 | 0.887   |
| CT_wavelet-HHH_ngtdm_Coarseness                          | 0.900    | 0.900 | 0.900 | 0.900   |
| CT_wavelet-HHH_ngtdm_Strength                            | 0.868    | 0.900 | 0.900 | 0.889   |
| CT_wavelet-LLL_firstorder_90Percentile                   | 0.904    | 0.904 | 0.904 | 0.904   |
| CT_wavelet-LLL_firstorder_Energy                         | 0.943    | 0.943 | 0.943 | 0.943   |
| CT_wavelet-LLL_firstorder_Entropy                        | 0.954    | 0.954 | 0.952 | 0.953   |
| CT_wavelet-LLL_firstorder_InterquartileRange             | 0.810    | 0.810 | 0.810 | 0.810   |
| CT_wavelet-LLL_firstorder_Kurtosis                       | 0.824    | 0.824 | 0.824 | 0.824   |
| CT_wavelet-LLL_firstorder_Maximum                        | 0.960    | 0.960 | 0.960 | 0.960   |
| CT_wavelet-LLL_firstorder_MeanAbsoluteDeviation          | 0.889    | 0.889 | 0.889 | 0.889   |
| CT_wavelet-LLL_firstorder_Mean                           | 0.868    | 0.868 | 0.868 | 0.868   |
| CT_wavelet-LLL_firstorder_Minimum                        | 0.935    | 0.935 | 0.935 | 0.935   |

| Feature name  | Binwidth |       |       |         |
|---|----------|-------|-------|---------|
|   | 0.05     | 0.10  | 0.20  | Average |
| CT_wavelet-LLL_firstorder_Range                       | 0.967    | 0.967 | 0.967 | 0.967   |
| CT_wavelet-LLL_firstorder_RobustMeanAbsoluteDeviation | 0.842    | 0.842 | 0.842 | 0.842   |
| CT_wavelet-LLL_firstorder_RootMeanSquared             | 0.868    | 0.868 | 0.868 | 0.868   |
| CT_wavelet-LLL_firstorder_Skewness                    | 0.848    | 0.848 | 0.848 | 0.848   |
| CT_wavelet-LLL_firstorder_TotalEnergy                 | 0.943    | 0.943 | 0.943 | 0.943   |
| CT_wavelet-LLL_firstorder_Uniformity                  | 0.961    | 0.961 | 0.955 | 0.959   |
| CT_wavelet-LLL_firstorder_Variance                    | 0.807    | 0.807 | 0.807 | 0.807   |
| CT_wavelet-LLL_glcm_Autocorrelation                   | 0.936    | 0.936 | 0.937 | 0.936   |
| CT_wavelet-LLL_glcm_JointAverage                      | 0.943    | 0.943 | 0.944 | 0.944   |
| CT_wavelet-LLL_glcm_Contrast                          | 0.830    | 0.830 | 0.830 | 0.830   |
| CT_wavelet-LLL_glcm_Correlation                       | 0.920    | 0.923 | 0.927 | 0.923   |
| CT_wavelet-LLL_glcm_DifferenceAverage                 | 0.896    | 0.896 | 0.896 | 0.896   |
| CT_wavelet-LLL_glcm_DifferenceEntropy                 | 0.944    | 0.943 | 0.941 | 0.943   |
| CT_wavelet-LLL_glcm_DifferenceVariance                | 0.865    | 0.865 | 0.865 | 0.865   |
| CT_wavelet-LLL_glcm_JointEnergy                       | 0.951    | 0.953 | 0.939 | 0.948   |
| CT_wavelet-LLL_glcm_JointEntropy                      | 0.953    | 0.950 | 0.946 | 0.949   |
| CT_wavelet-LLL_glcm_Imc2                              | 0.921    | 0.924 | 0.932 | 0.926   |
| CT_wavelet-LLL_glcm_Idm                               | 0.939    | 0.934 | 0.928 | 0.934   |
| CT_wavelet-LLL_glcm_Id                                | 0.938    | 0.934 | 0.929 | 0.934   |
| CT_wavelet-LLL_glcm_MaximumProbability                | 0.949    | 0.952 | 0.939 | 0.946   |
| CT_wavelet-LLL_glcm_SumEntropy                        | 0.951    | 0.951 | 0.948 | 0.950   |
| CT_wavelet-LLL_glrIm_GrayLevelNonUniformity           | 0.892    | 0.915 | 0.926 | 0.911   |
| CT_wavelet-LLL_glrIm_GrayLevelNonUniformityNormalized | 0.963    | 0.963 | 0.963 | 0.963   |
| CT_wavelet-LLL_glrIm_GrayLevelVariance                | 0.830    | 0.845 | 0.859 | 0.845   |

| Feature name  | Binwidth |       |       |         |
|---|----------|-------|-------|---------|
|   | 0.05     | 0.10  | 0.20  | Average |
| CT_wavelet-LLL_glrml_HighGrayLevelRunEmphasis         | 0.939    | 0.940 | 0.943 | 0.941   |
| CT_wavelet-LLL_glrml_LongRunEmphasis                  | 0.931    | 0.926 | 0.901 | 0.920   |
| CT_wavelet-LLL_glrml_LongRunHighGrayLevelEmphasis     | 0.916    | 0.873 | 0.823 | 0.871   |
| CT_wavelet-LLL_glrml_LongRunLowGrayLevelEmphasis      | 0.915    | 0.875 | 0.862 | 0.884   |
| CT_wavelet-LLL_glrml_LowGrayLevelRunEmphasis          | 0.929    | 0.917 | 0.922 | 0.923   |
| CT_wavelet-LLL_glrml_RunEntropy                       | 0.958    | 0.960 | 0.962 | 0.960   |
| CT_wavelet-LLL_glrml_RunLengthNonUniformity           | 0.940    | 0.934 | 0.927 | 0.933   |
| CT_wavelet-LLL_glrml_RunLengthNonUniformityNormalized | 0.929    | 0.928 | 0.929 | 0.928   |
| CT_wavelet-LLL_glrml_RunPercentage                    | 0.921    | 0.902 | 0.864 | 0.896   |
| CT_wavelet-LLL_glrml_RunVariance                      | 0.924    | 0.911 | 0.850 | 0.895   |
| CT_wavelet-LLL_glrml_ShortRunEmphasis                 | 0.938    | 0.940 | 0.941 | 0.940   |
| CT_wavelet-LLL_glrml_ShortRunHighGrayLevelEmphasis    | 0.940    | 0.942 | 0.944 | 0.942   |
| CT_wavelet-LLL_glrml_ShortRunLowGrayLevelEmphasis     | 0.929    | 0.920 | 0.930 | 0.927   |
| CT_wavelet-LLL_glszm_GrayLevelNonUniformity           | 0.938    | 0.934 | 0.930 | 0.934   |
| CT_wavelet-LLL_glszm_GrayLevelNonUniformityNormalized | 0.957    | 0.951 | 0.955 | 0.954   |
| CT_wavelet-LLL_glszm_GrayLevelVariance                | 0.903    | 0.922 | 0.943 | 0.923   |
| CT_wavelet-LLL_glszm_HighGrayLevelZoneEmphasis        | 0.951    | 0.954 | 0.958 | 0.955   |
| CT_wavelet-LLL_glszm_LowGrayLevelZoneEmphasis         | 0.965    | 0.958 | 0.954 | 0.959   |
| CT_wavelet-LLL_glszm_SizeZoneNonUniformity            | 0.919    | 0.913 | 0.904 | 0.912   |
| CT_wavelet-LLL_glszm_SizeZoneNonUniformityNormalized  | 0.956    | 0.948 | 0.943 | 0.949   |
| CT_wavelet-LLL_glszm_SmallAreaEmphasis                | 0.955    | 0.946 | 0.944 | 0.949   |
| CT_wavelet-LLL_glszm_SmallAreaHighGrayLevelEmphasis   | 0.953    | 0.955 | 0.958 | 0.955   |
| CT_wavelet-LLL_glszm_SmallAreaLowGrayLevelEmphasis    | 0.958    | 0.958 | 0.945 | 0.953   |
| CT_wavelet-LLL_glszm_ZoneEntropy                      | 0.966    | 0.968 | 0.970 | 0.968   |

| Feature name   | Binwidth |       |       |         |
|--|----------|-------|-------|---------|
|  | 0.05     | 0.10  | 0.20  | Average |
| CT_wavelet-LLL_glszm_ZonePercentage                      | 0.934    | 0.926 | 0.911 | 0.924   |
| CT_wavelet-LLL_gldm_DependenceEntropy                    | 0.962    | 0.963 | 0.958 | 0.961   |
| CT_wavelet-LLL_gldm_DependenceNonUniformity              | 0.912    | 0.914 | 0.924 | 0.917   |
| CT_wavelet-LLL_gldm_GrayLevelNonUniformity               | 0.843    | 0.855 | 0.892 | 0.863   |
| CT_wavelet-LLL_gldm_GrayLevelVariance                    | 0.807    | 0.807 | 0.807 | 0.807   |
| CT_wavelet-LLL_gldm_HighGrayLevelEmphasis                | 0.937    | 0.937 | 0.938 | 0.937   |
| CT_wavelet-LLL_gldm_LargeDependenceHighGrayLevelEmphasis | 0.882    | 0.893 | 0.912 | 0.896   |
| CT_wavelet-LLL_gldm_LargeDependenceLowGrayLevelEmphasis  | 0.844    | 0.834 | 0.849 | 0.843   |
| CT_wavelet-LLL_gldm_LowGrayLevelEmphasis                 | 0.919    | 0.905 | 0.908 | 0.910   |
| CT_wavelet-LLL_gldm_SmallDependenceEmphasis              | 0.935    | 0.927 | 0.913 | 0.925   |
| CT_wavelet-LLL_gldm_SmallDependenceHighGrayLevelEmphasis | 0.922    | 0.914 | 0.909 | 0.915   |
| CT_wavelet-LLL_gldm_SmallDependenceLowGrayLevelEmphasis  | 0.907    | 0.912 | 0.893 | 0.904   |
| CT_wavelet-LLL_ngtdm_Coarseness                          | 0.928    | 0.926 | 0.930 | 0.928   |
| CT_wavelet-LLL_ngtdm_Complexity                          | 0.887    | 0.896 | 0.907 | 0.897   |

**Table 8** The stable features in shape class in terms of %CV

| Feature name                 | Binwidth |       |       |         |
|------------------------------|----------|-------|-------|---------|
|                              | 0.05     | 0.10  | 0.20  | Average |
| CT_original_shape_Elongation | 9.664    | 9.664 | 9.664 | 9.664   |
| CT_original_shape_Sphericity | 5.263    | 5.263 | 5.263 | 5.263   |

**Table 9** The stable features in first-order class in terms of %CV

| Feature name                           | Binwidth |       |       |         |
|--|----------|-------|-------|---------|
|  | 0.05     | 0.10  | 0.20  | Average |
| CT_original_firstorder_10Percentile    | 3.660    | 3.660 | 3.660 | 3.660   |
| CT_original_firstorder_90Percentile    | 4.334    | 4.334 | 4.334 | 4.334   |
| CT_original_firstorder_Mean            | 2.111    | 2.111 | 2.111 | 2.111   |
| CT_original_firstorder_Median          | 0.469    | 0.469 | 0.469 | 0.469   |
| CT_original_firstorder_RootMeanSquared | 0.005    | 0.005 | 0.005 | 0.005   |

**Table 10** The stable features in texture class in terms of %CV

| Feature name                       | Binwidth |       |       |         |
|------------------------------------|----------|-------|-------|---------|
|                                    | 0.05     | 0.10  | 0.20  | Average |
| CT_original_glcm_Idm               | 9.151    | 7.214 | 5.257 | 7.208   |
| CT_original_glcm_Idmn              | 0.129    | 0.126 | 0.126 | 0.127   |
| CT_original_glcm_Id                | 7.505    | 6.029 | 4.520 | 6.018   |
| CT_original_glcm_Idn               | 0.468    | 0.451 | 0.458 | 0.459   |
| CT_original_glrlm_RunEntropy       | 7.886    | 7.882 | 7.643 | 7.804   |
| CT_original_glrlm_RunPercentage    | 4.365    | 6.010 | 7.933 | 6.103   |
| CT_original_glrlm_ShortRunEmphasis | 4.489    | 6.738 | 9.495 | 6.907   |
| CT_original_glszm_ZoneEntropy      | 5.795    | 7.516 | 9.645 | 7.652   |
| CT_original_gldm_DependenceEntropy | 5.000    | 5.907 | 7.468 | 6.125   |

**Table 11** The stable features in wavelet class in terms of %CV

| Feature name  | Binwidth |       |       |         |
|---|----------|-------|-------|---------|
|   | 0.05     | 0.10  | 0.20  | Average |
| CT_log-sigma-1-0-mm-3D_firstorder_RootMeanSquared             | 0.001    | 0.001 | 0.001 | 0.001   |
| CT_log-sigma-1-0-mm-3D_glcmm_Icm1                             | 6.975    | 7.414 | 7.698 | 7.362   |
| CT_log-sigma-1-0-mm-3D_glcmm_Icm2                             | 5.859    | 7.507 | 9.258 | 7.542   |
| CT_log-sigma-1-0-mm-3D_glcmm_Idm                              | 6.388    | 4.066 | 2.185 | 4.213   |
| CT_log-sigma-1-0-mm-3D_glcmm_Idmn                             | 0.149    | 0.172 | 0.293 | 0.205   |
| CT_log-sigma-1-0-mm-3D_glcmm_Id                               | 5.104    | 3.301 | 1.840 | 3.415   |
| CT_log-sigma-1-0-mm-3D_glcmm_Idn                              | 0.518    | 0.568 | 0.733 | 0.606   |
| CT_log-sigma-1-0-mm-3D_glcmm_InverseVariance                  | 3.267    | 2.561 | 2.972 | 2.933   |
| CT_log-sigma-1-0-mm-3D_glcmm_SumEntropy                       | 9.294    | 9.225 | 8.039 | 8.853   |
| CT_log-sigma-1-0-mm-3D_glrmm_RunEntropy                       | 5.039    | 5.053 | 4.893 | 4.995   |
| CT_log-sigma-1-0-mm-3D_glrmm_RunLengthNonUniformityNormalized | 6.034    | 5.486 | 5.316 | 5.612   |
| CT_log-sigma-1-0-mm-3D_glrmm_RunPercentage                    | 3.614    | 3.418 | 3.692 | 3.575   |
| CT_log-sigma-1-0-mm-3D_glrmm_ShortRunEmphasis                 | 3.683    | 3.666 | 3.253 | 3.534   |
| CT_log-sigma-1-0-mm-3D_gldm_DependenceEntropy                 | 3.821    | 3.690 | 3.034 | 3.515   |
| CT_log-sigma-1-0-mm-3D_gldm_DependenceNonUniformityNormalized | 6.424    | 6.563 | 6.107 | 6.365   |
| CT_log-sigma-2-0-mm-3D_firstorder_Entropy                     | 6.338    | 6.990 | 7.474 | 6.934   |
| CT_log-sigma-2-0-mm-3D_firstorder_RootMeanSquared             | 0.002    | 0.002 | 0.002 | 0.002   |
| CT_log-sigma-2-0-mm-3D_glcmm_Correlation                      | 5.585    | 5.397 | 5.340 | 5.441   |
| CT_log-sigma-2-0-mm-3D_glcmm_DifferenceEntropy                | 8.243    | 9.072 | 8.765 | 8.693   |
| CT_log-sigma-2-0-mm-3D_glcmm_JointEntropy                     | 7.617    | 8.167 | 8.302 | 8.028   |
| CT_log-sigma-2-0-mm-3D_glcmm_Icm1                             | 7.302    | 6.566 | 5.663 | 6.510   |
| CT_log-sigma-2-0-mm-3D_glcmm_Icm2                             | 1.870    | 2.303 | 3.192 | 2.455   |
| CT_log-sigma-2-0-mm-3D_glcmm_Idm                              | 6.223    | 4.274 | 2.539 | 4.346   |

| Feature name  | Binwidth |       |       |         |
|---|----------|-------|-------|---------|
|   | 0.05     | 0.10  | 0.20  | Average |
| CT_log-sigma-2-0-mm-3D_glcm_Idmn                              | 0.212    | 0.205 | 0.224 | 0.214   |
| CT_log-sigma-2-0-mm-3D_glcm_Id                                | 4.875    | 3.464 | 2.189 | 3.510   |
| CT_log-sigma-2-0-mm-3D_glcm_Idn                               | 0.679    | 0.650 | 0.609 | 0.646   |
| CT_log-sigma-2-0-mm-3D_glcm_InverseVariance                   | 3.580    | 3.347 | 4.842 | 3.923   |
| CT_log-sigma-2-0-mm-3D_glcm_SumEntropy                        | 5.776    | 6.340 | 6.747 | 6.288   |
| CT_log-sigma-2-0-mm-3D_glrlm_RunEntropy                       | 3.341    | 3.568 | 4.132 | 3.681   |
| CT_log-sigma-2-0-mm-3D_glrlm_RunLengthNonUniformityNormalized | 5.053    | 6.074 | 6.868 | 5.998   |
| CT_log-sigma-2-0-mm-3D_glrlm_RunPercentage                    | 3.307    | 3.868 | 4.378 | 3.851   |
| CT_log-sigma-2-0-mm-3D_glrlm_ShortRunEmphasis                 | 2.851    | 3.921 | 4.462 | 3.745   |
| CT_log-sigma-2-0-mm-3D_gldm_DependenceEntropy                 | 3.618    | 3.782 | 3.660 | 3.687   |
| CT_log-sigma-3-0-mm-3D_firstorder_Entropy                     | 4.678    | 5.753 | 7.041 | 5.824   |
| CT_log-sigma-3-0-mm-3D_firstorder_RootMeanSquared             | 0.002    | 0.002 | 0.002 | 0.002   |
| CT_log-sigma-3-0-mm-3D_glcm_Correlation                       | 5.065    | 4.952 | 5.073 | 5.030   |
| CT_log-sigma-3-0-mm-3D_glcm_DifferenceEntropy                 | 7.088    | 8.175 | 8.679 | 7.981   |
| CT_log-sigma-3-0-mm-3D_glcm_JointEntropy                      | 5.555    | 6.472 | 7.514 | 6.514   |
| CT_log-sigma-3-0-mm-3D_glcm_Imc1                              | 6.884    | 6.601 | 6.311 | 6.599   |
| CT_log-sigma-3-0-mm-3D_glcm_Imc2                              | 1.772    | 2.349 | 3.165 | 2.429   |
| CT_log-sigma-3-0-mm-3D_glcm_Idm                               | 5.239    | 3.690 | 2.332 | 3.754   |
| CT_log-sigma-3-0-mm-3D_glcm_Idmn                              | 0.204    | 0.205 | 0.207 | 0.205   |
| CT_log-sigma-3-0-mm-3D_glcm_Id                                | 4.020    | 2.998 | 2.004 | 3.007   |
| CT_log-sigma-3-0-mm-3D_glcm_Idn                               | 0.713    | 0.681 | 0.586 | 0.660   |
| CT_log-sigma-3-0-mm-3D_glcm_InverseVariance                   | 3.045    | 4.280 | 6.562 | 4.629   |
| CT_log-sigma-3-0-mm-3D_glcm_SumEntropy                        | 4.134    | 5.060 | 6.230 | 5.141   |
| CT_log-sigma-3-0-mm-3D_glrlm_RunEntropy                       | 3.117    | 3.564 | 4.261 | 3.647   |

| Feature name  | Binwidth |       |       |         |
|---|----------|-------|-------|---------|
|   | 0.05     | 0.10  | 0.20  | Average |
| CT_log-sigma-3-0-mm-3D_glrlm_RunLengthNonUniformityNormalized | 3.963    | 5.702 | 6.780 | 5.482   |
| CT_log-sigma-3-0-mm-3D_glrlm_RunPercentage                    | 2.734    | 3.814 | 4.786 | 3.778   |
| CT_log-sigma-3-0-mm-3D_glrlm_ShortRunEmphasis                 | 2.256    | 3.454 | 4.102 | 3.271   |
| CT_log-sigma-3-0-mm-3D_glszm_ZoneEntropy                      | 4.924    | 8.243 | 9.543 | 7.570   |
| CT_log-sigma-3-0-mm-3D_gldm_DependenceEntropy                 | 3.239    | 3.555 | 3.481 | 3.425   |
| CT_log-sigma-4-0-mm-3D_firstorder_Entropy                     | 4.678    | 5.923 | 7.839 | 6.147   |
| CT_log-sigma-4-0-mm-3D_firstorder_RootMeanSquared             | 0.003    | 0.003 | 0.003 | 0.003   |
| CT_log-sigma-4-0-mm-3D_glcm_Correlation                       | 5.888    | 5.914 | 6.369 | 6.057   |
| CT_log-sigma-4-0-mm-3D_glcm_DifferenceEntropy                 | 6.349    | 7.394 | 7.882 | 7.208   |
| CT_log-sigma-4-0-mm-3D_glcm_JointEntropy                      | 5.163    | 6.218 | 7.835 | 6.405   |
| CT_log-sigma-4-0-mm-3D_glcm_Imc1                              | 5.808    | 5.662 | 6.049 | 5.840   |
| CT_log-sigma-4-0-mm-3D_glcm_Imc2                              | 1.651    | 2.318 | 3.676 | 2.549   |
| CT_log-sigma-4-0-mm-3D_glcm_Idm                               | 5.016    | 3.711 | 2.443 | 3.723   |
| CT_log-sigma-4-0-mm-3D_glcm_Idmn                              | 0.230    | 0.232 | 0.231 | 0.231   |
| CT_log-sigma-4-0-mm-3D_glcm_Id                                | 3.810    | 2.928 | 2.098 | 2.946   |
| CT_log-sigma-4-0-mm-3D_glcm_Idn                               | 0.782    | 0.741 | 0.635 | 0.719   |
| CT_log-sigma-4-0-mm-3D_glcm_InverseVariance                   | 4.268    | 4.996 | 6.662 | 5.309   |
| CT_log-sigma-4-0-mm-3D_glcm_SumEntropy                        | 4.210    | 5.298 | 7.005 | 5.504   |
| CT_log-sigma-4-0-mm-3D_glrlm_RunEntropy                       | 3.608    | 4.154 | 4.854 | 4.205   |
| CT_log-sigma-4-0-mm-3D_glrlm_RunLengthNonUniformityNormalized | 3.757    | 5.580 | 7.251 | 5.529   |
| CT_log-sigma-4-0-mm-3D_glrlm_RunPercentage                    | 2.539    | 3.774 | 5.023 | 3.779   |
| CT_log-sigma-4-0-mm-3D_glrlm_ShortRunEmphasis                 | 2.052    | 3.068 | 4.212 | 3.111   |
| CT_log-sigma-4-0-mm-3D_glszm_ZoneEntropy                      | 5.736    | 7.991 | 8.945 | 7.557   |
| CT_log-sigma-4-0-mm-3D_gldm_DependenceEntropy                 | 3.382    | 3.657 | 3.731 | 3.590   |



| Feature name  | Binwidth |       |       |         |
|---|----------|-------|-------|---------|
|   | 0.05     | 0.10  | 0.20  | Average |
| CT_log-sigma-5-0-mm-3D_firstorder_Entropy                     | 4.724    | 5.987 | 8.086 | 6.266   |
| CT_log-sigma-5-0-mm-3D_firstorder_RootMeanSquared             | 0.003    | 0.003 | 0.003 | 0.003   |
| CT_log-sigma-5-0-mm-3D_glcmm_Correlation                      | 6.508    | 6.664 | 7.423 | 6.865   |
| CT_log-sigma-5-0-mm-3D_glcmm_DifferenceEntropy                | 5.316    | 6.132 | 6.851 | 6.100   |
| CT_log-sigma-5-0-mm-3D_glcmm_JointEntropy                     | 4.942    | 6.023 | 8.003 | 6.323   |
| CT_log-sigma-5-0-mm-3D_glcmm_Imc1                             | 5.318    | 5.553 | 6.527 | 5.800   |
| CT_log-sigma-5-0-mm-3D_glcmm_Imc2                             | 1.714    | 2.536 | 4.192 | 2.814   |
| CT_log-sigma-5-0-mm-3D_glcmm_Idm                              | 5.229    | 3.836 | 2.610 | 3.892   |
| CT_log-sigma-5-0-mm-3D_glcmm_Idmn                             | 0.226    | 0.228 | 0.226 | 0.227   |
| CT_log-sigma-5-0-mm-3D_glcmm_Id                               | 3.938    | 3.021 | 2.246 | 3.068   |
| CT_log-sigma-5-0-mm-3D_glcmm_Idn                              | 0.730    | 0.701 | 0.610 | 0.680   |
| CT_log-sigma-5-0-mm-3D_glcmm_InverseVariance                  | 3.954    | 4.750 | 7.064 | 5.256   |
| CT_log-sigma-5-0-mm-3D_glcmm_SumEntropy                       | 4.480    | 5.670 | 7.788 | 5.979   |
| CT_log-sigma-5-0-mm-3D_glrmm_RunEntropy                       | 3.744    | 4.252 | 5.008 | 4.335   |
| CT_log-sigma-5-0-mm-3D_glrmm_RunLengthNonUniformityNormalized | 3.858    | 5.749 | 7.463 | 5.690   |
| CT_log-sigma-5-0-mm-3D_glrmm_RunPercentage                    | 2.489    | 3.864 | 5.328 | 3.894   |
| CT_log-sigma-5-0-mm-3D_glrmm_ShortRunEmphasis                 | 2.070    | 3.108 | 4.152 | 3.110   |
| CT_log-sigma-5-0-mm-3D_glszm_ZoneEntropy                      | 5.621    | 6.987 | 7.791 | 6.800   |
| CT_log-sigma-5-0-mm-3D_gldm_DependenceEntropy                 | 3.483    | 3.619 | 3.825 | 3.642   |
| CT_wavelet-LLH_firstorder_Entropy                             | 6.711    | 7.807 | 8.393 | 7.637   |
| CT_wavelet-LLH_firstorder_RootMeanSquared                     | 0.004    | 0.004 | 0.004 | 0.004   |
| CT_wavelet-LLH_glcmm_DifferenceEntropy                        | 7.124    | 8.000 | 8.481 | 7.869   |
| CT_wavelet-LLH_glcmm_JointEntropy                             | 7.669    | 8.763 | 9.173 | 8.535   |
| CT_wavelet-LLH_glcmm_Imc1                                     | 8.632    | 7.663 | 6.945 | 7.747   |

| Feature name  | Binwidth |       |       |         |
|---|----------|-------|-------|---------|
|   | 0.05     | 0.10  | 0.20  | Average |
| CT_wavelet-LLH_glcm_Imc2                              | 3.659    | 4.740 | 5.846 | 4.749   |
| CT_wavelet-LLH_glcm_Idm                               | 9.072    | 7.105 | 5.066 | 7.081   |
| CT_wavelet-LLH_glcm_Idmn                              | 0.250    | 0.243 | 0.232 | 0.242   |
| CT_wavelet-LLH_glcm_Id                                | 7.105    | 5.626 | 4.046 | 5.592   |
| CT_wavelet-LLH_glcm_Idn                               | 0.605    | 0.589 | 0.583 | 0.592   |
| CT_wavelet-LLH_glcm_InverseVariance                   | 7.048    | 4.752 | 3.099 | 4.966   |
| CT_wavelet-LLH_glcm_SumEntropy                        | 6.295    | 7.212 | 7.635 | 7.047   |
| CT_wavelet-LLH_glrlm_RunEntropy                       | 4.328    | 4.425 | 4.459 | 4.404   |
| CT_wavelet-LLH_glrlm_RunLengthNonUniformityNormalized | 3.489    | 4.304 | 4.193 | 3.995   |
| CT_wavelet-LLH_glrlm_RunPercentage                    | 2.212    | 2.687 | 2.584 | 2.495   |
| CT_wavelet-LLH_glrlm_ShortRunEmphasis                 | 1.775    | 2.378 | 2.577 | 2.243   |
| CT_wavelet-LLH_glszm_SmallAreaEmphasis                | 3.238    | 4.661 | 8.700 | 5.533   |
| CT_wavelet-LLH_glszm_ZoneEntropy                      | 2.353    | 2.935 | 4.368 | 3.219   |
| CT_wavelet-LLH_gldm_DependenceEntropy                 | 2.974    | 3.289 | 3.426 | 3.230   |
| CT_wavelet-LLH_gldm_DependenceNonUniformityNormalized | 9.224    | 7.161 | 6.935 | 7.773   |
| CT_wavelet-LHL_firstorder_RootMeanSquared             | 0.000    | 0.000 | 0.000 | 0.000   |
| CT_wavelet-LHL_firstorder_Uniformity                  | 7.956    | 3.714 | 1.169 | 4.280   |
| CT_wavelet-LHL_glcm_DifferenceEntropy                 | 8.236    | 4.344 | 1.131 | 4.570   |
| CT_wavelet-LHL_glcm_Idm                               | 2.659    | 0.972 | 0.389 | 1.340   |
| CT_wavelet-LHL_glcm_Idmn                              | 0.160    | 0.425 | 0.940 | 0.508   |
| CT_wavelet-LHL_glcm_Id                                | 2.198    | 0.835 | 0.383 | 1.138   |
| CT_wavelet-LHL_glcm_Idn                               | 0.627    | 0.988 | 1.397 | 1.004   |
| CT_wavelet-LHL_glcm_InverseVariance                   | 1.522    | 1.468 | 1.704 | 1.565   |
| CT_wavelet-LHL_glcm_MaximumProbability                | 6.574    | 3.440 | 2.614 | 4.210   |

| Feature name  | Binwidth |       |       |         |
|---|----------|-------|-------|---------|
|   | 0.05     | 0.10  | 0.20  | Average |
| CT_wavelet-LHL_glcm_SumEntropy                        | 9.081    | 6.126 | 2.876 | 6.028   |
| CT_wavelet-LHL_glrlm_LongRunEmphasis                  | 5.901    | 5.339 | 7.833 | 6.357   |
| CT_wavelet-LHL_glrlm_RunEntropy                       | 5.943    | 5.144 | 4.212 | 5.099   |
| CT_wavelet-LHL_glrlm_RunLengthNonUniformityNormalized | 4.563    | 4.989 | 6.745 | 5.433   |
| CT_wavelet-LHL_glrlm_RunPercentage                    | 2.999    | 3.542 | 4.722 | 3.754   |
| CT_wavelet-LHL_glrlm_ShortRunEmphasis                 | 2.940    | 2.753 | 3.890 | 3.194   |
| CT_wavelet-LHL_gldm_DependenceEntropy                 | 2.972    | 1.963 | 1.100 | 2.012   |
| CT_wavelet-LHL_gldm_DependenceNonUniformityNormalized | 4.854    | 3.951 | 3.062 | 3.956   |
| CT_wavelet-LHL_gldm_DependenceVariance                | 8.631    | 6.645 | 5.291 | 6.856   |
| CT_wavelet-LHL_gldm_LargeDependenceEmphasis           | 6.337    | 6.654 | 7.728 | 6.907   |
| CT_wavelet-LHH_firstorder_Entropy                     | 7.670    | 4.479 | 1.328 | 4.492   |
| CT_wavelet-LHH_firstorder_RootMeanSquared             | 0.000    | 0.000 | 0.000 | 0.000   |
| CT_wavelet-LHH_firstorder_Uniformity                  | 5.649    | 2.288 | 0.538 | 2.825   |
| CT_wavelet-LHH_glcm_DifferenceAverage                 | 7.644    | 3.509 | 1.725 | 4.293   |
| CT_wavelet-LHH_glcm_DifferenceEntropy                 | 6.845    | 3.577 | 1.069 | 3.830   |
| CT_wavelet-LHH_glcm_JointEnergy                       | 9.045    | 3.496 | 0.969 | 4.503   |
| CT_wavelet-LHH_glcm_JointEntropy                      | 7.338    | 3.914 | 1.108 | 4.120   |
| CT_wavelet-LHH_glcm_Imc1                              | 9.099    | 8.289 | 5.803 | 7.730   |
| CT_wavelet-LHH_glcm_Imc2                              | 9.635    | 8.052 | 5.660 | 7.783   |
| CT_wavelet-LHH_glcm_Idm                               | 2.305    | 1.004 | 0.497 | 1.269   |
| CT_wavelet-LHH_glcm_Idmn                              | 0.350    | 1.068 | 1.841 | 1.086   |
| CT_wavelet-LHH_glcm_Id                                | 1.829    | 0.850 | 0.472 | 1.050   |
| CT_wavelet-LHH_glcm_Idn                               | 0.904    | 1.569 | 1.979 | 1.484   |
| CT_wavelet-LHH_glcm_InverseVariance                   | 1.409    | 1.273 | 1.318 | 1.333   |

| Feature name  | Binwidth |       |       |         |
|---|----------|-------|-------|---------|
|   | 0.05     | 0.10  | 0.20  | Average |
| CT_wavelet-LHH_glcm_MaximumProbability                | 5.569    | 2.634 | 1.498 | 3.234   |
| CT_wavelet-LHH_glcm_SumEntropy                        | 5.825    | 2.996 | 0.974 | 3.265   |
| CT_wavelet-LHH_grlm_GrayLevelNonUniformityNormalized  | 7.684    | 3.235 | 0.665 | 3.861   |
| CT_wavelet-LHH_grlm_LongRunEmphasis                   | 4.990    | 5.080 | 6.575 | 5.549   |
| CT_wavelet-LHH_grlm_RunEntropy                        | 4.433    | 3.552 | 2.675 | 3.554   |
| CT_wavelet-LHH_grlm_RunLengthNonUniformityNormalized  | 3.164    | 3.484 | 4.041 | 3.563   |
| CT_wavelet-LHH_grlm_RunPercentage                     | 1.959    | 2.269 | 2.699 | 2.309   |
| CT_wavelet-LHH_grlm_RunVariance                       | 5.747    | 7.321 | 9.040 | 7.369   |
| CT_wavelet-LHH_grlm_ShortRunEmphasis                  | 1.873    | 1.961 | 2.361 | 2.065   |
| CT_wavelet-LHH_gldm_DependenceEntropy                 | 2.117    | 1.263 | 0.762 | 1.381   |
| CT_wavelet-LHH_gldm_DependenceNonUniformityNormalized | 3.441    | 2.842 | 2.415 | 2.899   |
| CT_wavelet-LHH_gldm_DependenceVariance                | 6.631    | 4.895 | 4.142 | 5.222   |
| CT_wavelet-LHH_gldm_LargeDependenceEmphasis           | 5.029    | 5.059 | 5.698 | 5.262   |
| CT_wavelet-HLL_firstorder_RootMeanSquared             | 0.000    | 0.000 | 0.000 | 0.000   |
| CT_wavelet-HLL_firstorder_Uniformity                  | 7.968    | 3.581 | 1.080 | 4.210   |
| CT_wavelet-HLL_glcm_Idm                               | 2.597    | 0.926 | 0.398 | 1.307   |
| CT_wavelet-HLL_glcm_Idmn                              | 0.140    | 0.408 | 0.935 | 0.494   |
| CT_wavelet-HLL_glcm_Id                                | 2.148    | 0.795 | 0.390 | 1.111   |
| CT_wavelet-HLL_glcm_Idn                               | 0.578    | 0.944 | 1.377 | 0.966   |
| CT_wavelet-HLL_glcm_InverseVariance                   | 1.639    | 1.323 | 1.719 | 1.560   |
| CT_wavelet-HLL_glcm_MaximumProbability                | 6.246    | 3.057 | 2.309 | 3.871   |
| CT_wavelet-HLL_glcm_SumEntropy                        | 9.178    | 6.201 | 2.818 | 6.066   |
| CT_wavelet-HLL_grlm_LongRunEmphasis                   | 5.796    | 5.148 | 8.055 | 6.333   |
| CT_wavelet-HLL_grlm_RunEntropy                        | 6.145    | 5.323 | 4.326 | 5.265   |

| Feature name  | Binwidth |       |       |         |
|---|----------|-------|-------|---------|
|   | 0.05     | 0.10  | 0.20  | Average |
| CT_wavelet-HLL_grlm_RunLengthNonUniformityNormalized  | 4.273    | 4.685 | 6.844 | 5.268   |
| CT_wavelet-HLL_grlm_RunPercentage                     | 2.720    | 3.310 | 4.807 | 3.612   |
| CT_wavelet-HLL_grlm_ShortRunEmphasis                  | 3.014    | 2.524 | 3.987 | 3.175   |
| CT_wavelet-HLL_gldm_DependenceEntropy                 | 3.093    | 2.056 | 1.157 | 2.102   |
| CT_wavelet-HLL_gldm_DependenceNonUniformityNormalized | 4.968    | 3.934 | 3.172 | 4.025   |
| CT_wavelet-HLL_gldm_DependenceVariance                | 8.843    | 6.596 | 5.545 | 6.994   |
| CT_wavelet-HLL_gldm_LargeDependenceEmphasis           | 5.585    | 6.168 | 7.804 | 6.519   |
| CT_wavelet-HLH_firstorder_Entropy                     | 7.080    | 4.312 | 1.347 | 4.246   |
| CT_wavelet-HLH_firstorder_RootMeanSquared             | 0.000    | 0.000 | 0.000 | 0.000   |
| CT_wavelet-HLH_firstorder_Uniformity                  | 5.159    | 2.078 | 0.428 | 2.555   |
| CT_wavelet-HLH_glcm_DifferenceAverage                 | 7.355    | 3.341 | 1.491 | 4.063   |
| CT_wavelet-HLH_glcm_DifferenceEntropy                 | 6.499    | 3.528 | 1.047 | 3.691   |
| CT_wavelet-HLH_glcm_JointEnergy                       | 8.397    | 3.293 | 0.688 | 4.126   |
| CT_wavelet-HLH_glcm_JointEntropy                      | 6.911    | 3.883 | 1.105 | 3.966   |
| CT_wavelet-HLH_glcm_Imc1                              | 7.880    | 6.393 | 4.661 | 6.311   |
| CT_wavelet-HLH_glcm_Imc2                              | 9.224    | 7.115 | 4.661 | 7.000   |
| CT_wavelet-HLH_glcm_Idm                               | 2.167    | 0.933 | 0.415 | 1.172   |
| CT_wavelet-HLH_glcm_Idmn                              | 0.246    | 0.584 | 1.439 | 0.757   |
| CT_wavelet-HLH_glcm_Id                                | 1.715    | 0.783 | 0.389 | 0.962   |
| CT_wavelet-HLH_glcm_Idn                               | 0.721    | 1.012 | 1.577 | 1.103   |
| CT_wavelet-HLH_glcm_InverseVariance                   | 1.334    | 1.080 | 1.048 | 1.154   |
| CT_wavelet-HLH_glcm_MaximumProbability                | 4.989    | 2.280 | 1.058 | 2.776   |
| CT_wavelet-HLH_glcm_SumEntropy                        | 5.502    | 3.011 | 0.834 | 3.116   |
| CT_wavelet-HLH_grlm_GrayLevelNonUniformityNormalized  | 7.184    | 3.090 | 0.658 | 3.644   |

| Feature name  | Binwidth |       |       |         |
|---|----------|-------|-------|---------|
|   | 0.05     | 0.10  | 0.20  | Average |
| CT_wavelet-HLH_glrml_LongRunEmphasis                  | 4.465    | 4.503 | 6.079 | 5.016   |
| CT_wavelet-HLH_glrml_RunEntropy                       | 4.211    | 3.465 | 2.618 | 3.432   |
| CT_wavelet-HLH_glrml_RunLengthNonUniformityNormalized | 2.905    | 3.407 | 4.094 | 3.469   |
| CT_wavelet-HLH_glrml_RunPercentage                    | 1.814    | 2.212 | 2.709 | 2.245   |
| CT_wavelet-HLH_glrml_RunVariance                      | 5.304    | 6.525 | 8.007 | 6.612   |
| CT_wavelet-HLH_glrml_ShortRunEmphasis                 | 1.770    | 1.975 | 2.434 | 2.060   |
| CT_wavelet-HLH_gldm_DependenceEntropy                 | 1.923    | 1.086 | 0.633 | 1.214   |
| CT_wavelet-HLH_gldm_DependenceNonUniformityNormalized | 2.885    | 2.534 | 2.270 | 2.563   |
| CT_wavelet-HLH_gldm_DependenceVariance                | 5.688    | 3.919 | 3.657 | 4.421   |
| CT_wavelet-HLH_gldm_LargeDependenceEmphasis           | 4.421    | 4.871 | 5.592 | 4.961   |
| CT_wavelet-HHL_firstorder_Entropy                     | 0.271    | 0.035 | 0.021 | 0.109   |
| CT_wavelet-HHL_firstorder_RootMeanSquared             | 0.000    | 0.000 | 0.000 | 0.000   |
| CT_wavelet-HHL_firstorder_Uniformity                  | 0.080    | 0.031 | 0.029 | 0.047   |
| CT_wavelet-HHL_glcm_ClusterProminence                 | 2.259    | 0.914 | 0.870 | 1.348   |
| CT_wavelet-HHL_glcm_ClusterTendency                   | 1.071    | 0.886 | 0.880 | 0.946   |
| CT_wavelet-HHL_glcm_Contrast                          | 1.220    | 1.296 | 1.301 | 1.273   |
| CT_wavelet-HHL_glcm_Correlation                       | 5.332    | 5.239 | 5.236 | 5.269   |
| CT_wavelet-HHL_glcm_DifferenceAverage                 | 1.237    | 1.298 | 1.301 | 1.278   |
| CT_wavelet-HHL_glcm_DifferenceEntropy                 | 0.309    | 0.312 | 0.316 | 0.312   |
| CT_wavelet-HHL_glcm_DifferenceVariance                | 0.428    | 0.429 | 0.433 | 0.430   |
| CT_wavelet-HHL_glcm_JointEnergy                       | 0.358    | 0.376 | 0.379 | 0.371   |
| CT_wavelet-HHL_glcm_JointEntropy                      | 0.270    | 0.148 | 0.151 | 0.190   |
| CT_wavelet-HHL_glcm_Imc1                              | 8.190    | 7.899 | 7.880 | 7.990   |
| CT_wavelet-HHL_glcm_Imc2                              | 5.342    | 5.057 | 5.035 | 5.145   |

| Feature name  | Binwidth |       |       |         |
|---|----------|-------|-------|---------|
|   | 0.05     | 0.10  | 0.20  | Average |
| CT_wavelet-HHL_glcm_Idm                               | 0.310    | 0.323 | 0.324 | 0.319   |
| CT_wavelet-HHL_glcm_Idmn                              | 1.223    | 0.362 | 0.113 | 0.566   |
| CT_wavelet-HHL_glcm_Id                                | 0.311    | 0.323 | 0.324 | 0.319   |
| CT_wavelet-HHL_glcm_Idn                               | 1.287    | 0.438 | 0.199 | 0.641   |
| CT_wavelet-HHL_glcm_InverseVariance                   | 1.262    | 1.299 | 1.301 | 1.287   |
| CT_wavelet-HHL_glcm_MaximumProbability                | 1.116    | 1.094 | 1.093 | 1.101   |
| CT_wavelet-HHL_glcm_SumEntropy                        | 0.323    | 0.162 | 0.153 | 0.212   |
| CT_wavelet-HHL_glcm_SumSquares                        | 0.227    | 0.033 | 0.025 | 0.095   |
| CT_wavelet-HHL_glrIm_GrayLevelNonUniformityNormalized | 0.110    | 0.020 | 0.016 | 0.049   |
| CT_wavelet-HHL_glrIm_GrayLevelVariance                | 0.418    | 0.032 | 0.016 | 0.155   |
| CT_wavelet-HHL_glrIm_LongRunEmphasis                  | 7.782    | 7.846 | 7.849 | 7.826   |
| CT_wavelet-HHL_glrIm_RunEntropy                       | 3.212    | 3.140 | 3.135 | 3.162   |
| CT_wavelet-HHL_glrIm_RunLengthNonUniformityNormalized | 6.046    | 6.083 | 6.084 | 6.071   |
| CT_wavelet-HHL_glrIm_RunPercentage                    | 4.384    | 4.421 | 4.423 | 4.410   |
| CT_wavelet-HHL_glrIm_ShortRunEmphasis                 | 3.783    | 3.839 | 3.842 | 3.821   |
| CT_wavelet-HHL_gldm_DependenceEntropy                 | 0.780    | 0.756 | 0.755 | 0.764   |
| CT_wavelet-HHL_gldm_DependenceNonUniformityNormalized | 3.085    | 3.070 | 3.069 | 3.075   |
| CT_wavelet-HHL_gldm_DependenceVariance                | 5.566    | 5.528 | 5.526 | 5.540   |
| CT_wavelet-HHL_gldm_GrayLevelVariance                 | 0.251    | 0.038 | 0.029 | 0.106   |
| CT_wavelet-HHL_gldm_LargeDependenceEmphasis           | 7.969    | 8.007 | 8.009 | 7.995   |
| CT_wavelet-HHH_firstorder_Entropy                     | 0.093    | 0.007 | 0.007 | 0.036   |
| CT_wavelet-HHH_firstorder_InterquartileRange          | 9.058    | 9.058 | 9.058 | 9.058   |
| CT_wavelet-HHH_firstorder_RootMeanSquared             | 0.000    | 0.000 | 0.000 | 0.000   |
| CT_wavelet-HHH_firstorder_Uniformity                  | 0.027    | 0.010 | 0.010 | 0.015   |

| Feature name  | Binwidth |       |       |         |
|---|----------|-------|-------|---------|
|   | 0.05     | 0.10  | 0.20  | Average |
| CT_wavelet-HHH_glcm_Autocorrelation                   | 6.981    | 0.271 | 0.271 | 2.507   |
| CT_wavelet-HHH_glcm_JointAverage                      | 3.889    | 0.131 | 0.131 | 1.384   |
| CT_wavelet-HHH_glcm_ClusterProminence                 | 0.812    | 0.590 | 0.590 | 0.664   |
| CT_wavelet-HHH_glcm_ClusterTendency                   | 0.603    | 0.587 | 0.587 | 0.592   |
| CT_wavelet-HHH_glcm_Contrast                          | 0.709    | 0.651 | 0.651 | 0.670   |
| CT_wavelet-HHH_glcm_DifferenceAverage                 | 0.675    | 0.651 | 0.651 | 0.659   |
| CT_wavelet-HHH_glcm_DifferenceEntropy                 | 0.191    | 0.147 | 0.147 | 0.161   |
| CT_wavelet-HHH_glcm_DifferenceVariance                | 0.231    | 0.200 | 0.200 | 0.210   |
| CT_wavelet-HHH_glcm_JointEnergy                       | 0.182    | 0.185 | 0.185 | 0.184   |
| CT_wavelet-HHH_glcm_JointEntropy                      | 0.129    | 0.072 | 0.072 | 0.091   |
| CT_wavelet-HHH_glcm_Imc1                              | 5.220    | 5.158 | 5.158 | 5.179   |
| CT_wavelet-HHH_glcm_Imc2                              | 4.251    | 4.161 | 4.161 | 4.191   |
| CT_wavelet-HHH_glcm_Idm                               | 0.209    | 0.203 | 0.203 | 0.205   |
| CT_wavelet-HHH_glcm_Idmn                              | 0.688    | 0.068 | 0.068 | 0.275   |
| CT_wavelet-HHH_glcm_Idn                               | 0.208    | 0.203 | 0.203 | 0.204   |
| CT_wavelet-HHH_glcm_Idn                               | 0.710    | 0.123 | 0.123 | 0.318   |
| CT_wavelet-HHH_glcm_InverseVariance                   | 0.651    | 0.651 | 0.651 | 0.651   |
| CT_wavelet-HHH_glcm_MaximumProbability                | 0.617    | 0.629 | 0.629 | 0.625   |
| CT_wavelet-HHH_glcm_SumEntropy                        | 0.249    | 0.237 | 0.237 | 0.241   |
| CT_wavelet-HHH_glcm_SumSquares                        | 0.071    | 0.007 | 0.007 | 0.028   |
| CT_wavelet-HHH_glrlm_GrayLevelNonUniformityNormalized | 0.036    | 0.006 | 0.006 | 0.016   |
| CT_wavelet-HHH_glrlm_GrayLevelVariance                | 0.123    | 0.006 | 0.006 | 0.045   |
| CT_wavelet-HHH_glrlm_HighGrayLevelRunEmphasis         | 6.616    | 0.234 | 0.234 | 2.361   |
| CT_wavelet-HHH_glrlm_LongRunEmphasis                  | 5.166    | 5.191 | 5.191 | 5.183   |



| Feature name   | Binwidth |       |       |         |
|--|----------|-------|-------|---------|
|  | 0.05     | 0.10  | 0.20  | Average |
| CT_wavelet-HHH_glrmlm_RunEntropy                       | 2.272    | 2.236 | 2.236 | 2.248   |
| CT_wavelet-HHH_glrmlm_RunLengthNonUniformityNormalized | 3.880    | 3.884 | 3.884 | 3.882   |
| CT_wavelet-HHH_glrmlm_RunPercentage                    | 2.790    | 2.798 | 2.798 | 2.795   |
| CT_wavelet-HHH_glrmlm_RunVariance                      | 7.315    | 7.332 | 7.332 | 7.326   |
| CT_wavelet-HHH_glrmlm_ShortRunEmphasis                 | 2.325    | 2.339 | 2.339 | 2.334   |
| CT_wavelet-HHH_glrmlm_ShortRunHighGrayLevelEmphasis    | 7.880    | 2.409 | 2.409 | 4.233   |
| CT_wavelet-HHH_glszm_GrayLevelNonUniformityNormalized  | 9.287    | 6.230 | 6.230 | 7.249   |
| CT_wavelet-HHH_gldm_DependenceEntropy                  | 0.700    | 0.698 | 0.698 | 0.699   |
| CT_wavelet-HHH_gldm_DependenceNonUniformityNormalized  | 2.963    | 2.961 | 2.961 | 2.962   |
| CT_wavelet-HHH_gldm_DependenceVariance                 | 4.807    | 4.809 | 4.809 | 4.808   |
| CT_wavelet-HHH_gldm_GrayLevelVariance                  | 0.080    | 0.010 | 0.010 | 0.033   |
| CT_wavelet-HHH_gldm_HighGrayLevelEmphasis              | 6.654    | 0.278 | 0.278 | 2.403   |
| CT_wavelet-HHH_gldm_LargeDependenceEmphasis            | 6.222    | 6.231 | 6.231 | 6.228   |
| CT_wavelet-LLL_firstorder_10Percentile                 | 3.765    | 3.765 | 3.765 | 3.765   |
| CT_wavelet-LLL_firstorder_90Percentile                 | 4.837    | 4.837 | 4.837 | 4.837   |
| CT_wavelet-LLL_firstorder_Mean                         | 2.158    | 2.158 | 2.158 | 2.158   |
| CT_wavelet-LLL_firstorder_Median                       | 0.558    | 0.558 | 0.558 | 0.558   |
| CT_wavelet-LLL_firstorder_RootMeanSquared              | 0.015    | 0.015 | 0.015 | 0.015   |
| CT_wavelet-LLL_glcm_Imc1                               | 6.924    | 6.425 | 6.804 | 6.718   |
| CT_wavelet-LLL_glcm_Imc2                               | 3.787    | 5.212 | 7.544 | 5.514   |
| CT_wavelet-LLL_glcm_Idmn                               | 0.114    | 0.111 | 0.109 | 0.111   |
| CT_wavelet-LLL_glcm_Id                                 | 8.981    | 7.832 | 6.361 | 7.725   |
| CT_wavelet-LLL_glcm_Idn                                | 0.416    | 0.408 | 0.401 | 0.408   |
| CT_wavelet-LLL_glcm_InverseVariance                    | 9.305    | 6.213 | 5.186 | 6.902   |

| Feature name  | Binwidth |       |       |         |
|---|----------|-------|-------|---------|
|   | 0.05     | 0.10  | 0.20  | Average |
| CT_wavelet-LLL_glrIm_RunEntropy                       | 6.940    | 7.025 | 7.063 | 7.010   |
| CT_wavelet-LLL_glrIm_RunLengthNonUniformityNormalized | 3.967    | 6.656 | 9.463 | 6.695   |
| CT_wavelet-LLL_glrIm_RunPercentage                    | 2.367    | 3.941 | 5.286 | 3.865   |
| CT_wavelet-LLL_glrIm_ShortRunEmphasis                 | 2.040    | 3.716 | 5.538 | 3.765   |
| CT_wavelet-LLL_glszm_SmallAreaEmphasis                | 5.170    | 5.857 | 7.502 | 6.176   |
| CT_wavelet-LLL_glszm_ZoneEntropy                      | 4.163    | 4.658 | 5.811 | 4.877   |
| CT_wavelet-LLL_gldm_DependenceEntropy                 | 4.022    | 4.499 | 5.341 | 4.621   |



## REFERENCES

1. team TACSmaec. About Nasopharyngeal Cancer. American Cancer Society 2018.
2. Mahdavifar N, Ghoncheh M, Mohammadian-Hafshejani A, Khosravi B, Salehiniya H. Epidemiology and Inequality in the Incidence and Mortality of Nasopharynx Cancer in Asia. *Osong Public Health Res Perspect*. 2016;7(6):360-72.
3. Sung H, Ferlay J, Siegel RL, Laversanne M, Soerjomataram I, Jemal A, et al. Global Cancer Statistics 2020: GLOBOCAN Estimates of Incidence and Mortality Worldwide for 36 Cancers in 185 Countries. *CA Cancer J Clin*. 2021;71(3):209-49.
4. Lee AW, Ma BB, Ng WT, Chan AT. Management of Nasopharyngeal Carcinoma: Current Practice and Future Perspective. *J Clin Oncol*. 2015;33(29):3356-64.
5. Wong KCW, Hui EP, Lo KW, Lam WKJ, Johnson D, Li L, et al. Nasopharyngeal carcinoma: an evolving paradigm. *Nat Rev Clin Oncol*. 2021;18(11):679-95.
6. Lin R. Target volume delineation and margins in the management of lung cancers in the era of image guided radiation therapy. *J Med Radiat Sci*. 2014;61(1):1-3.
7. Njeh CF. Tumor delineation The weakest link in the search for. *Journal of Medical Physics*. 2008;23.
8. van Timmeren JE, Cester D, Tanadini-Lang S, Alkadhi H, Baessler B. Radiomics in medical imaging-"how-to" guide and critical reflection. *Insights Imaging*. 2020;11(1):91.
9. Intarak S, Chongpison Y, Vimolnoch M, Oonsiri S, Kitpanit S, Prayongrat A, et al. Tumor Prognostic Prediction of Nasopharyngeal Carcinoma Using CT-Based Radiomics in Non-Chinese Patients. *Front Oncol*. 2022;12:775248.
10. Pan XX, Tong LH, Chen YF, Li FL, Tang WB, Liu YJ, et al. A simplified T classification based on the 8th edition of the UICC/AJCC staging system for nasopharyngeal carcinoma. *Cancer Manag Res*. 2019;11:3163-9.
11. team TACSmaec. Nasopharyngeal Cancer Early Detection, Diagnosis, and Staging. American Cancer Society. 2022.

12. Mayerhoefer ME, Materka A, Langs G, Haggstrom I, Szczypinski P, Gibbs P, et al. Introduction to Radiomics. *J Nucl Med.* 2020;61(4):488-95.
13. Lambin P, Rios-Velazquez E, Leijenaar R, Carvalho S, van Stiphout RG, Granton P, et al. Radiomics: extracting more information from medical images using advanced feature analysis. *Eur J Cancer.* 2012;48(4):441-6.
14. Dice LR. Measures of the Amount of Ecologic Association Between Species. *Ecology.* 2012;26:297-302.
15. Chang ATY, Tan LT, Duke S, Ng WT. Challenges for Quality Assurance of Target Volume Delineation in Clinical Trials. *Front Oncol.* 2017;7:221.
16. Vinod SK, Jameson MG, Min M, Holloway LC. Uncertainties in volume delineation in radiation oncology: A systematic review and recommendations for future studies. *Radiother Oncol.* 2016;121(2):169-79.
17. Jan Van de Steenea, Nadine Linthouta, Johan de Meyb, Vincent Vinh-Hunga, Cornelia Claassensa, Marc Noppenc, Arjan Bela, Guy Stormea. Definition of gross tumor volume in lung cancer inter-observer variability. *Radiotherapy and Oncology.* 2002;62:37-49.
18. Pavic M, Bogowicz M, Wurms X, Glatz S, Finazzi T, Riesterer O, et al. Influence of inter-observer delineation variability on radiomics stability in different tumor sites. *Acta Oncol.* 2018;57(8):1070-4.
19. Amin MB, Greene FL, Edge SB, Compton CC, Gershenwald JE, Brookland RK, et al. The Eighth Edition AJCC Cancer Staging Manual: Continuing to build a bridge from a population-based to a more "personalized" approach to cancer staging. *CA Cancer J Clin.* 2017;67(2):93-9.
20. van Griethuysen JJM, Fedorov A, Parmar C, Hosny A, Aucoin N, Narayan V, et al. Computational Radiomics System to Decode the Radiographic Phenotype. *Cancer Res.* 2017;77(21):e104-e7.
21. Aronhime S, Calcagno C, Jajamovich GH, Dyvorne HA, Robson P, Dieterich D, et al. DCE-MRI of the liver: effect of linear and nonlinear conversions on hepatic perfusion quantification and reproducibility. *J Magn Reson Imaging.* 2014;40(1):90-8.

22. Koo TK, Li MY. A Guideline of Selecting and Reporting Intraclass Correlation Coefficients for Reliability Research. *J Chiropr Med.* 2016;15(2):155-63.



## VITA

**NAME** Pongpitch Panyura

**DATE OF BIRTH** 31 January 1997

**PLACE OF BIRTH** Choburi, Thailand

**INSTITUTIONS ATTENDED** 2016-2019 Bachelor of Science Degree (Second class honors),  
Department of Physics, Faculty of Science, Chulalongkorn  
University

